

DISSERTATION

Testing the foundations of cosmology with
the radio sky

submitted to Faculty of Physics, Bielefeld University

by

Thilo Max Siewert

November 2020

Supervisor: Prof. Dr. Dominik J. Schwarz

Thilo Max Siewert
t.siewert@physik.uni-bielefeld.de
Wellensiek 177, 33619 Bielefeld
Germany

Gedruckt auf alterungsbeständigem Papier "DIN-ISO 9706"

List of Publications

As part of my PhD studies at the Bielefeld University between October 2016 and November 2020 I have contributed to several scientific publications. The detailed contributions to the listed publications are highlighted in the corresponding sections of this thesis.

- **“Testing the standard model of cosmology with the SKA: the cosmic radio dipole”**
Carlos A. P. Bengaly, Thilo M. Siewert, Dominik J. Schwarz, and Roy Maartens
MNRAS 486, 1350-1357 (2019), arXiv:1810.04960 [astro-ph.CO]
<https://doi.org/10.1093/mnras/stz832> (see Sect. 3.3)
- **“SKA and the Cosmic Radio Dipole”**
Dominik J. Schwarz, Carlos A. P. Bengaly, Roy Maartens, and Thilo M. Siewert
arXiv:1810.06373 [astro-ph.CO], submitted to Proceedings of the International Astronomical Union (see Sec. 3.5)
- **“Cosmology with Phase 1 of the Square Kilometre Array Red Book 2018: Technical specifications and performance forecasts”**
Square Kilometre Array Cosmology Science Working Group, 46 authors including Thilo M. Siewert
PASA 37, e007 (2020), arXiv:1811.02743 [astro-ph.CO]
<https://doi.org/10.1017/pasa.2019.51> (see Sect. 3.4)
- **“One- and Two-point Source Statistics from the LOFAR Two-metre Sky Survey First Data Release”**
Thilo M. Siewert, Catherine Hale, Nitesh Bhardwaj, Marian Biermann, David J. Bacon, Matt Jarvis, Huub Röttgering, Dominik J. Schwarz, Timothy Shimwell, Philip N. Best, Kenneth J. Duncan, Martin J. Hardcastle, Jose Sabater, Cyril Tasse, Glenn J. White, and Wendy L. Williams
A&A 643, A100 (2020), arXiv:1908.10309 [astro-ph.CO]
<https://doi.org/10.1051/0004-6361/201936592> (see Sect. 4.4)
- **“The Cosmic Radio Dipole: Estimators and Frequency Dependence”**
Thilo M. Siewert, Matthias Schmidt-Rubart, and Dominik J. Schwarz
arXiv:2010.08366 [astro-ph.CO], submitted to A&A on November 3rd, 2020 (see Sect. 2.3)
- **“Extremely deep 150 MHz source counts from the LoTSS Deep Fields”**
Soumyajit Mandal et al., 22 authors including Thilo M. Siewert
arXiv:2011.08829 [astro-ph.GA], Part of the LoTSS deep field first data release

Abstract

In this work the foundations of cosmology are tested based on the observed radio sky. The assumption of the Cosmic Radio Dipole being caused by the proper motion of the Solar System with respect to the Cosmic Microwave Background (CMB) is studied with recent radio continuum surveys. The fundamental assumption of an isotropic Universe is studied by means of radio source distributions.

In the first project (Siewert et al., 2020b), we introduce a quadratic estimator in order to derive the Cosmic Radio Dipole. The estimator is tested against possible contributions from the masking procedure and low source densities. As the estimator is nearly unbiased with respect to the tested effects, it is applied to source count maps of four radio continuum surveys. We find nearly consistent dipole amplitudes for three of the four surveys, while we find a significantly increased dipole amplitude for the fourth survey. Additionally, we find indications for a frequency dependent dipole amplitude, which is analysed in more detail by cross-matching the lowest and highest frequency surveys. The project is extended by studying a rescaled version of the lowest frequency survey, which is intended to overcome flux density offsets in the survey. In this updated radio source catalogue we find an intermediate dipole amplitude. The observed dipole direction however is inconsistent with previous findings, which additionally indicates systematic contributions to the Cosmic Radio Dipole.

The second project resulted in three publications (Schwarz et al., 2018; Bengaly et al., 2019; Square Kilometre Array Cosmology Science Working Group et al., 2020), which address forecasts of the Cosmic Radio Dipole for observations by means of the Square Kilometre Array (SKA). Based on the specifications of the upcoming SKA survey, maps of radio source counts are simulated. These mock catalogues include clustering and are boosted by a fiducial kinematic dipole, based on the observed dipole of the CMB. The survey specifications are varied for the two phases of the SKA and the flux density thresholds are varied for realistic and optimistic cases. Using the quadratic estimator from the previous project, we can recover the simulated Cosmic Radio Dipole within positional offsets of about a few degrees. Additionally, we show that the local Universe within redshifts below $z = 0.5$ contributes to variations in the observed amplitude and direction of the Cosmic Radio Dipole.

In the third project (Siewert et al., 2020a), the data quality of the first data release of the LOFAR Two-Metre Sky Survey (LoTSS-DR1) is analysed. We compare the point source completeness and the one-point statistics of the radio source catalogue to the value added source catalogue. Based on the spatial distribution of the source counts, we find for both catalogues an improved fit to a Compound Poisson distribution rather than to a assumed Poisson distribution. The observed differential source counts of the value added source catalogue show good agreement with simulated source distributions of the SKA Design Study and the Tiered Radio Extragalactic Continuum Simulation. Additionally, we measure the angular two-point correlation function for the LoTSS-DR1 value added source catalogue. Using expectations based on the best-fit cosmological model of Planck 2018, we find good agreement with the observed angular two-point correlation function of flux-limited subsamples with photometric redshift information.

Contents

1	Introduction	1
1.1	The radio sky	4
1.2	Radio sources	9
1.2.1	Active galactic nuclei	9
1.2.2	Star-forming Galaxies	10
1.3	Radio telescopes	11
1.4	Radio continuum surveys	13
1.5	Measures of Large-Scale Structures	19
1.5.1	Counts-in-cells	19
1.5.2	Differential number counts	25
1.5.3	Angular two-point correlation function	27
1.5.4	Cosmic Radio Dipole	29
2	Estimators of the Cosmic Radio Dipole	33
2.1	Comparison of a linear and a quadratic estimator	34
2.2	Estimates from different surveys	35
2.3	Publication arXiv:2010.08366	37
2.4	Supplementary material	38
2.4.1	NVSS with a different noise mask	38
2.4.2	Spectral Index from TGSSxNVSS	40
2.4.3	Different fitting routine	41
2.4.4	Rescaled TGSS-ADR1 catalogue	43
3	Forecasting possible Radio Dipole measurements	49
3.1	Forecast of the structure dipole	50
3.2	Forecast in terms of the Square Kilometre Array	50
3.3	Publication MNRAS 486, pp. 1350-1357 (2019)	52
3.4	Publication PASA 37, e007 (2020)	53
3.5	Publication arXiv:1810.06373	54
4	One- and two-point source statistics of LOFAR radio sources	55
4.1	Source count distribution of LOFAR radio sources	56
4.2	Angular two-point correlation function of LOFAR radio sources	58

4.3	Comparison to expectations of the cosmological standard model	59
4.4	Publication A&A 643, A100 (2020)	61
4.5	Supplementary material	62
4.5.1	Sensitivity of the survey	62
4.5.2	Mock - Mock correlation	63
4.5.3	Settings of CAMB SOURCES	65
4.5.4	Angular two-point correlation function for different redshift bins	68
4.6	Quality cut on redshift distribution	70
4.7	Comparison of the angular two-point correlation function	73
4.8	Estimating the angular two-point correlation function from different surveys	77
4.8.1	TGSS-ADR1 angular two-point correlation	78
4.8.2	WENSS angular two-point correlation	79
4.8.3	SUMSS angular two-point correlation	81
4.8.4	NVSS angular two-point correlation	82
5	Summary and Conclusion	87
	Acknowledgements	91
	Appendix	93
A.1	Differential source counts	93
A.2	Angular two-point correlation	95
A.3	Settings of CAMB SOURCES	96
A.4	Bias Modification	98

Chapter 1

Introduction

For many centuries, the place of our Earth and the Solar system in the Universe has been an open question and triggered multiple models and measurements from all perspectives of astronomy. Based on the discovery of the Cosmic Microwave Background (CMB; Penzias and Wilson 1965; Dicke et al. 1965), the observed sky brightness temperature revealed at first sight an isotropic sky, which is in good agreement with the Cosmological Principle. In general the CMB, which originates from the time of recombination, obeys a nearly perfect black-body spectrum at a temperature of $T_b = 2.7$ K (Fixsen, 2009). The Cosmological Principle states that the Universe is homogenous and isotropic, such that an observer placed elsewhere in the Universe would statistically observe the same distribution of matter and energy. Therefore, the CMB is assumed to be a perfect probe to define an absolute rest frame in the Universe. At second sight, the CMB reveals a dipole anisotropy of order 10^{-3} in the temperature distribution (Fixsen et al., 1994; Planck Collaboration et al., 2018a), which was firstly observed by Partridge and Wilkinson (1967), Conklin (1969), and Henry (1971). This anisotropy give again rise to questions about the absolute rest frame of the Universe. Already Condon and Harwit (1968) and Peebles and Wilkinson (1968) proposed in their works that the motion of the Solar system can introduce a dipole anisotropy to the observed brightness temperature of the CMB. Assuming this proper motion to be the only origin of the observed dipole anisotropy, the assumptions of the Cosmological Principle and the CMB as rest frame are still satisfied. Only after subtracting the proper motion and further contributions of the Milky Way from the CMB, anisotropies of order 10^{-5} in the temperature distribution are getting visible. Due to the high accuracies of recent observations, like from the Planck space telescope (Tauber et al., 2010; Planck Collaboration et al., 2018a), the CMB dipole is accepted to be a solid measurement and the proper motion of the Solar System is currently the standard interpretation of its origin. Primordial remnants, due to pre-inflationary fluctuation of the density field, could also contribute to the CMB dipole anisotropy (Turner, 1991), but are expected to be sub-dominant.

Beside the measurements of the CMB, the dipole can be studied from different perspectives in astronomy and by extragalactic probes, such as radio sources. Recent measurements of the dipole anisotropy in the radio spectrum, hereinafter called Cosmic Radio

Dipole, revealed strong differences in the observed dipole velocities (e.g. Ellis and Baldwin 1984; Blake and Wall 2002), which might rule out local peculiar motions as the only origin of the Cosmic Radio Dipole. Depending on the observed frequency, the observed dipole amplitudes of the Cosmic Radio Dipole are found to be factors of five to ten larger than the CMB dipole amplitude and are in general of order 10^{-2} . In contrast to the CMB dipole, the Cosmic Radio Dipole is not generally accepted to be of kinematic origin and several systematic contributions, like fractional sky coverages and poorer signal to noise ratios of the radio surveys can contribute to the observed differences. Additionally, the observations of the Cosmic Radio Dipole are mostly based on source counts of extragalactic radio sources, which can introduce biases based on local and/or large-scale structures.

In order to distinguish the different contributions of local structures and other systematics to the Cosmic Radio Dipole, new instruments and surveys are needed, which observe the radio sky in more depth and resolution. Furthermore, supplementary informations, like photometric and/or spectroscopic redshifts for the radio sources are needed to understand the local and large-scale structures. Additionally, these studies will give insights on the general assumption of the Cosmological Principle, which is assumed to be statistically correct at distance scales larger than $100 h^{-1}\text{Mpc}$. Studying the source distribution as a function of different dependencies more closely, evolutionary models of the Universe can be tested and the isotropy of the Universe can be quantified.

The aim of this thesis is to study the Cosmic Radio Dipole and contributions to it, as well as the general source distribution of sources in the observed Universe. Therefore, the thesis can be divided into three separated projects.

Firstly, we draw our attention to the question of how to measure the Cosmic Radio Dipole from existing radio surveys. Therefore, we test a linear and a quadratic estimator in Section 2. For the first time, we measure in Siewert et al. (2020b) the Cosmic Radio Dipole from four different radio surveys with a consistent routine and data reduction pipeline. Additionally in this analysis, the source catalogue of SUMSS is used for the first time to measure the Cosmic Radio Dipole. Furthermore, we test the general assumption of the Cosmic Radio Dipole with a new fitting routine in Section 2.4.3, by fitting either a pure monopole, or a monopole with dipole modulation to the observed source counts.

As upcoming surveys will be able to probe the radio sky in more depth, we simulate in the second project (see Sect.3) mock catalogues of radio sources for the specifications of the SKA telescope. In order to test contributions from local structures to the Cosmic Radio Dipole, we simulate in Schwarz et al. (2018), Bengaly et al. (2019), and Square Kilometre Array Cosmology Science Working Group et al. (2020) source counts maps, which include large-scale structures and clustering based on the recent best-fit ΛCDM cosmology. Finally, the source count maps are boosted with a kinematic dipole of the order of the CMB dipole. The quadratic estimator from the previous project is then used to measure the Cosmic Radio Dipole of these simulations for different flux density thresholds and redshift bins.

While the SKA surveys are still in the planning process, we analyse in the third project (see Sect. 4) the data quality of the LOFAR Two-metre Sky Survey and its first data

release (LoTSS-DR1; Shimwell et al. 2019). We do so, by estimating the point source completeness and identifying under-sampled regions in the coverage of the HETDEX field. The two available source catalogues of the LoTSS-DR1 are then used to determine the spatial source count distribution, to which two models of a Poisson and a Compound Poisson distribution are fitted. In order to analyse the capabilities of the LoTSS-DR1 for cosmological measurements, we measure the differential source counts and compare them to source catalogues of the SKA Design Study (SKADS; Wilman et al. 2008) and the Tiered Radio Extragalactic Continuum Simulation (T-RECS; Bonaldi et al. 2019). We also measure the angular two-point correlation function of the LoTSS-DR1 and compare it with the help of additional redshift information to expectations based on the best-fit cosmological model of the Planck 2018 analysis.

In order to address the measurements of the Cosmic Radio Dipole and the source distributions, the basic concepts of these radio sources, their signals and how to observe them are introduced in the Sections 1.1 to 1.4. We summarise the results of Chapter 2, 3, and 4 in Chapter 5.

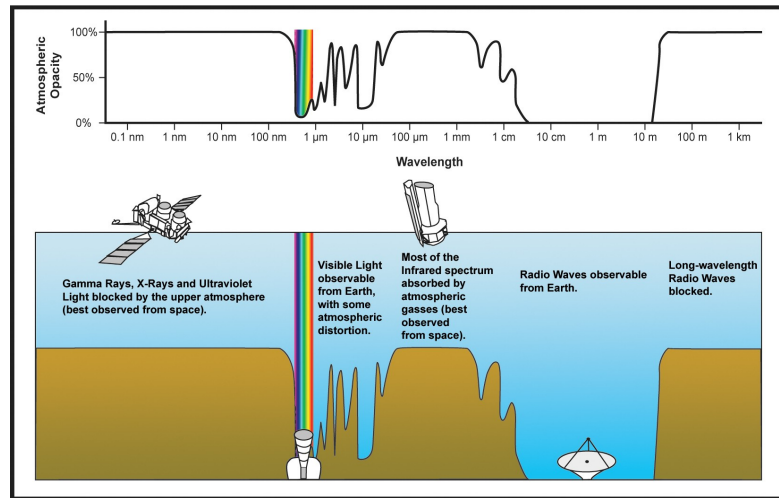


Figure 1.1: Electromagnetic opacity of the Earth's atmosphere for different wavelengths (NASA).

1.1 The radio sky

In the following, the concepts of radio emission and their radiation processes are briefly introduced. The derivations used in this section follow the books of Wilson et al. (2013) and Burke et al. (2019).

The corresponding probes of cosmological tests and tracers of large-scale structures are often radio sources observed with radio continuum surveys. Especially radio sources are good tracers of large-scale structures, as most radio sources are of extra-galactic nature. Most commonly, these sources are Radio Galaxies (RG), Star-forming galaxies (SFG) and other sources with an Active Galactic Nuclei (AGN), for example Quasars. Similar to optical observations, the radio spectrum is not strongly affected by the atmosphere of the Earth and can therefore easily be observed with ground-based instruments, without the need to observe from space (see Figure 1.1). Most of the absorption in the atmosphere originates from water vapour, which also varies strongly in time, and atmospheric gases, like carbon dioxide and ozone. The radio regime is typically defined as the range between 10^{-3} m and 10^1 m, whereas in recent works 10^{-4} m wavelengths are also included in the radio regime. In industrial standards, the radio regime is subdivided into bands, like in the Institute of Electrical and Electronics Engineers (IEEE) standard, as most of the frequencies in the radio regime also have industrial usage. For example, most of the terrestrial radio broadcasting is done between MHz and GHz, like the VHF band II and the L band, which can also interfere with possible observations. Most of the radio spectrum we observe from Earth in the sky is emitted in the Galactic plane and from strong extragalactic sources. Observing the sky at longer wavelengths, the most prominent radio emissions come from synchrotron and free-free processes. For smaller wavelengths, dust emission starts to dominate. In general, the observed sources

are quantified by their observed flux density (following Burke et al. 2019):

$$S_\nu = \int_{\Omega_s} I_\nu(\theta, \phi) \cos \theta d\Omega, \quad (1.1)$$

which is the integral of the spectral brightness I_ν at angle θ to the observer over the solid angle Ω_s covered by the source on the sky. In astronomical units, the flux density at frequency ν is measured in terms of Jansky, which relates to SI-unit via $1 \text{ Jy} = 10^{-26} \text{ Wm}^{-2}\text{Hz}^{-1}$. The observed spectral brightness can be related to the received power dP per surface area $d\sigma$ of the detector, observing at frequency bandwidth $d\nu$ via:

$$\frac{dP}{d\sigma d\nu} = I_\nu \cos \theta d\Omega. \quad (1.2)$$

In terms of radio telescopes, the received spectral brightness is often referred to as brightness temperature T_b , which can in the limit of long wavelengths and the Rayleigh-Jeans law be written as:

$$T_b = \frac{c^2}{2k\nu^2} I_\nu. \quad (1.3)$$

For the two main radiation processes - synchrotron and free-free emission - the emitted power is derived in the following.

Synchrotron radiation is produced by high energetic electrons circling in galactic magnetic fields. The total emitted power of one electron can be derived under the assumption, that the electron is moving with constant, relativistic speed ($|\vec{v}| = \text{const}, \beta \approx 1$) in a homogeneous magnetic field \vec{B} . The motion is described by the relativistic Einstein-Planck equation (following Wilson et al., 2013)

$$\frac{d}{dt}(\gamma m \vec{v}) = \frac{e}{c}(\vec{v} \times \vec{B}) \quad (1.4)$$

and, under the absence of an electric field \vec{E} , additionally

$$\frac{d}{dt}(\gamma m c^2) = 0. \quad (1.5)$$

By splitting the velocity into a parallel (\vec{v}_\parallel) and perpendicular part (\vec{v}_\perp), with respect to \vec{B} and $|\vec{v}| = \text{const}$, one finds

$$\frac{d\vec{v}_\parallel}{dt} = 0, \quad \frac{d\vec{v}_\perp}{dt} = \frac{e}{\gamma m c}(\vec{v}_\perp \times \vec{B}), \quad (1.6)$$

which lead to the conclusion that the electron is forced on a circular motion with a gyration frequency of

$$\omega_B = \frac{e|\vec{B}|}{\gamma m c}. \quad (1.7)$$

As the motion on circular orbits is accelerated, the acceleration of the electron is derived by:

$$\vec{a}_\perp = \omega_B \vec{v}_\perp. \quad (1.8)$$

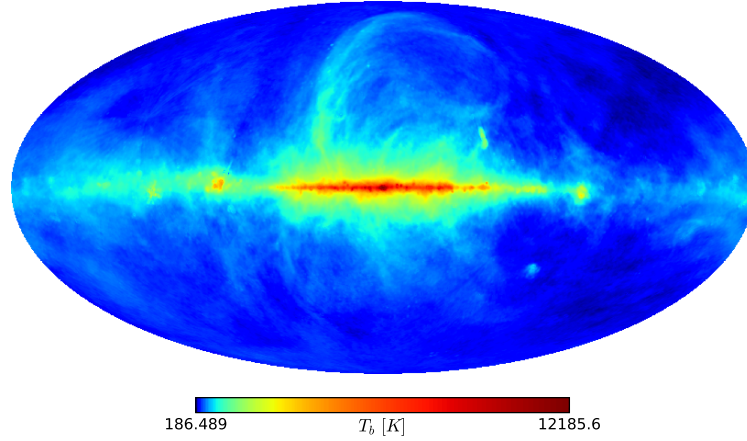


Figure 1.2: Full sky map of the brightness temperature at 150 MHz, scaled from 408 MHz (Haslam et al., 1982) with spectral index $\alpha = 2.8$. Strong sources have been removed. The map is shown in Mollweide view and in galactic coordinates with a HEALPIX resolution of $N_{\text{side}} = 512$.

According to Larmor's formula, an accelerated charge radiates at a given time the following amount of power:

$$P(t) = \frac{2}{3} \frac{e^2 \dot{\mathbf{v}}^2(t)}{c^3}. \quad (1.9)$$

Using Eq. (1.7), (1.8), and (1.9), the emitted power of one accelerated electron is:

$$P = \frac{2e^4 \bar{v}_\perp^2 \bar{\mathbf{B}}^2}{3m^2 c^5} \left(\frac{E}{mc^2} \right)^2, \quad (1.10)$$

with the total energy of the electron $E = \gamma mc^2$. In an observer rest frame the emitted power per solid angle Ω can be written as (Wilson et al., 2013):

$$\frac{dP}{d\Omega} = \frac{1}{4\pi} \frac{e^2}{c^3} a_\perp^2 \frac{1}{(1 - \beta \cos \theta)^3} \left(1 - \frac{\sin^2 \theta \cos^2 \phi}{\gamma^2 (1 - \beta \cos \theta)^2} \right). \quad (1.11)$$

For a relativistic electron this radiation will be focused towards a cone with angle θ .

In Figure 1.2, a full sky map of the brightness temperature at 150 MHz is shown in galactic coordinates and Mollweide projection. The full sky map shown in Figure 1.2 is based on the Hierarchical Equal Area isoLatitude Pixelation (HEALPix; Górski et al. 2005)¹ with a resolution of $N_{\text{side}} = 512$. Combining several partial sky maps, Haslam et al. (1981) made the effort to produce a full sky map of the sky brightness temperature at 408 MHz (Haslam et al., 1982). The brightness temperature map in Figure 1.2 has been scaled from 408 MHz to 150 MHz using the power law $T_b \propto \nu^{-\alpha}$ with a spectral index of

¹<http://healpix.sourceforge.net>

$\alpha = 2.8$. After removing strong sources, the remaining most prominent source of radiation is the Galactic plane in the centre of the map. This observed brightness temperature is mostly dominated by diffuse synchrotron emission of the interstellar medium and supernovae remnants.

Emission from free electrons, which scatter with free ions from an ionized hydrogen cloud, is called free-free emission, or bremsstrahlung. The scattering of these free electrons on ions accelerate the electrons and therefore lead the electron, accordingly to Larmor's formula (see Eq. 1.9), to radiate power. Induced by the electrostatic interaction between the electron and the ion, a parallel and a perpendicular force acting on the electron can be formulated. Based on Coulomb's law and in case of the perpendicular force, the acceleration of the electron with velocity v is given by (following Wilson et al. 2013):

$$m_e a_{\perp} = -\frac{Ze^2}{p^2} \cos \Psi, \quad (1.12)$$

with charge number Z of the ion, p the closest distance of the electron to the ion, and Ψ the angle between the ion and the position of the electron. Using Larmor's formula (see Eq. 1.9) and the previous acceleration we find the emitted power of a single electron:

$$P = \frac{2}{3} \frac{Z^2 e^6}{c^3 m_e^2 p^2} \cos^6 \Psi. \quad (1.13)$$

Scaling the thermal emission of a single electron-ion collision to clouds of N_i ions and N_e electrons, one defines the emission coefficient for the free-free emission as:

$$\epsilon_{\nu} = \frac{8}{2} \frac{Z^2 e^6}{c^3} \frac{N_i N_e}{m^2} \sqrt{\frac{2m}{\pi kT}} \ln \frac{p_2}{p_1}, \quad (1.14)$$

where p_1 and p_2 are upper and lower limits of the collision parameter in the cloud. Based on Kirchhoff's law, the emission coefficient is related to the absorption coefficient κ_{ν} and we can define the optical depth by:

$$\tau_{\nu} = -\int_0^D \kappa_{\nu} ds. \quad (1.15)$$

Together with a measure for the fluctuation of the electron density N_e along the path from the observer to a distance D , called emission measure:

$$\text{EM} = \int_0^D ds N_e^2, \quad (1.16)$$

and assuming the ionized gas to be in local thermal equilibrium, the free-free optical depth is:

$$\tau_{\nu} \approx 0.082 \left(\frac{T_e}{\text{K}} \right)^{-1.35} \left(\frac{\nu}{\text{GHz}} \right)^{-2.1} \left(\frac{\text{EM}}{\text{pc cm}^{-6}} \right). \quad (1.17)$$

Cordes and Lazio (2002) introduced a model for the Galactic distribution of free electrons. The so called NE2001 model is based on dispersion measurements of pulsars,

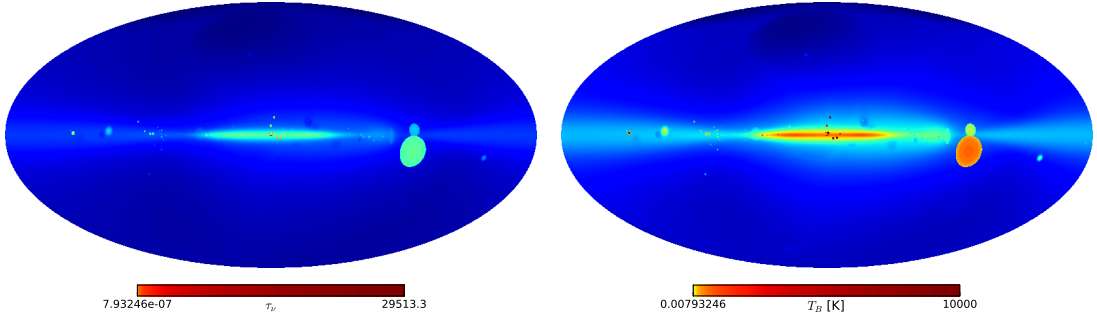


Figure 1.3: Optical depth (*left*) and brightness temperature (*right*) estimated from the NE2001 model with an electron temperature of $T_e = 10^4$ K and up to 20 kpc at a frequency of $\nu = 150$ MHz. Both maps are shown in galactic coordinates and Mollweide projection, with a HEALPIX resolution of $N_{\text{side}} = 1024$.

measurements of the angular broadening of sources, and emission measures. In total 1736 measurements throughout the Galaxy are used to estimate the free electron distribution. Assuming an electron temperature of $T_e = 10^4$ K, we use the NE2001 model to simulate the emission measure for the full sky. The resulting optical depth, while assuming an observing frequency of 150 MHz, is shown as a full sky map in Figure 1.3 (left) with galactic coordinates in a Mollweide projection and a HEALPIX resolution of $N_{\text{side}} = 1024$. Based on the assumed electron temperature and the simulated optical depth, the brightness temperature can again be inferred by:

$$T_b = T_e(1 - e^{-\tau\nu}). \quad (1.18)$$

The resulting brightness temperature in Kelvin of the simulated optical depth is shown in Figure 1.3 (right). Similar to the observed brightness temperature (Fig. 1.2; Haslam et al. 1981), the Galactic centre contributes mostly to the observed temperature. Other strong sources, like the Gum nebula and the Vela supernovae remnant in the western part of the full-sky maps in Figure 1.3, contribute to the observed brightness temperature as well.

1.2 Radio sources

Besides radio sources in our own Galaxy, like supernovae remnants, two populations of extragalactic radio sources dominate the observed radio sky. These two populations of Active Galactic Nuclei (AGN) and Star-Forming Galaxies (SFG) are discussed in the following.

1.2.1 Active galactic nuclei

The population of Active Galactic Nuclei is a group of different classes of sources, which have presumably a Supermassive Black Hole (SMBH) in the core of their host galaxy. The host galaxy is in most cases, based on the Hubble classification scheme (Hubble, 1926) of optical galaxies, an elliptical galaxy. Depending on the line of sight to this source, the sources can again be divided into several groups. Due to the strong appearance in the radio spectrum, the galaxies inhabiting an AGN are also called Radio Galaxies. All of these AGN sources have a core with a SMBH in common, which is fed by an accretion disk. This accretion disk is a thin, gravitational bounded collection of visible matter circling around the SMBH. The accretion disk itself is fed by the host-galaxy through an optically thick torus. Due to the interaction in the accretion disk, the matter heats up and loses angular momentum, which is transferred into radiation. By losing angular momentum, the matter finally falls beyond the event horizon of the SMBH. The radiation from the accretion disk can then be blocked by gas regions, circling at high elevation around the main axis of rotation of the SMBH. Depending on the speed of these gas regions, they are classified as Broad Line (BLR) and Narrow Line Regions (NLR). From the SMBH, two jets of highly energetic and relativistic particles, mainly electrons are ejected along the axis of rotation. These electrons emit synchrotron radiation, caused by the magnetic field of the galaxy. The elongated shape of these Radio Galaxies can be seen in Figure 1.4². The broad regions at the end of the jets are called hot-spots and lobes, where the energetic particles are stopped in the intergalactic medium, mainly consisting of ionized hydrogen clouds. Again, the main radiation in the lobes and hot-spots comes from synchrotron radiation. Due to tides in accretion and energy outburst in the AGN, the lobes can show several shock-fronts, which fade out into the intergalactic medium.

Based on the distance of the hot-spots to the core of the Radio Galaxy, the sources can be sub-divided into Fanaroff-Riley (FR) sources of class I and II (Fanaroff and Riley, 1974). In recent studies, more sub-classes of FR sources are distinguished, like FR O sources (Ghisellini, 2011), which are expected to evolve into FR I radio galaxies (Garofalo and Singh, 2019). The appearance of FR I and II radio galaxies goes beyond typical length scales of a few kpc of optical galaxies. For example, the jets of a FR radio galaxy can reach hot-spot to hot-spot distances of a few Mpc. The core, including the AGN, has a typical diameter of ~ 1 pc.

The other main sub-group of AGNs is called Quasi-Stellar Objects (QSO) or Quasars.

²Credit: Judith Croston and the LOFAR surveys team. www.lofar-surveys.org

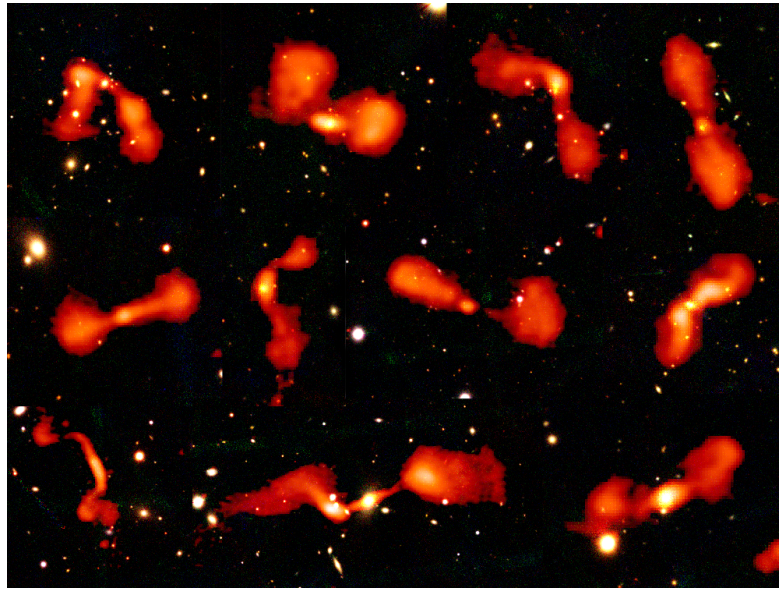


Figure 1.4: Collage of low-power radio galaxies, observed in the HETDEX field covered by the LOFAR Two-Metre Sky Survey. The galaxies are shown on an optical background. [Credit: Judith Croston and the LOFAR surveys team, downloaded from <https://lofar-surveys.org>]

Based on the Unified Oriented Scheme of AGNs (Barthel, 1989), Quasars are AGNs, where the observer looks either directly into the jet, or close to it. Because of the high speeds of the particles in the jet, the emission of the quasars is boosted towards the observer and appears therefore brighter. Vice versa, the counterjet appears fainter and is not in all cases visible. Typical Quasars outshine their host-galaxy even in the optical spectrum and appear as bright, point-like sources.

To complete the classification of AGNs, they are typically sub-divided into radio-loud and radio-quiet sources (Wilson and Colbert, 1995). The sources discussed above are usually included in the radio-loud sector of the AGN classification, whereas radio-quiet quasars and Seyfert galaxies (Seyfert, 1943) define the radio-quiet regime of the AGNs. Seyfert galaxies are usually seen in the optical as normal galaxies, with a bright core and can again be sub-divided by the broadening of spectral lines.

1.2.2 Star-forming Galaxies

Another type of galaxies, which appear in the radio regime, are star-forming (SFG), or star-burst galaxies. These star-forming galaxies are more related to normal galaxies, mostly prominent in the optical and infrared regime, as they do not show an active SMBH in their centre. Due to the increased star formation rate (SFR) in these galaxies, the radio emission emerges from cosmic rays of recently formed stars and/or supernovae remnants. The supernovae remnants produce charged particles, which dominate through



Figure 1.5: *Left*: Single dish radio telescope in Effelsberg, Germany [Credit: Dr. G. Schmitz, downloaded from de.wikipedia.org/wiki/Radioteleskop_Effelsberg]. *Right*: LBA Antennas of the LOFAR station “DE609” in Norderstedt, Germany [Downloaded from www.glowconsortium.de].

steep synchrotron radiation the radio continuum at low frequencies (Condon, 1992). Additionally, the star-forming galaxies show in the radio continuum a flat-spectrum free-free component, which dominates at higher frequencies (Condon, 1992). The radio emission of these star-forming galaxies is therefore highly correlated to the SFR (Kennicutt and Evans, 2012). In detail, the radio emission shows a linear correlation with the far infrared (FIR) emission (Yun et al., 2001; Sargent et al., 2010). The FIR radiation is mostly emitted by dust, which is heated by the stars in the galaxy. As both, SFG and Seyfert galaxies, are dominated by synchrotron radiation in the radio regime, they can hardly be distinguished. Only for objects with an excess in the radio luminosity compared to the prediction of the radio-FIR correlation, AGN contributions can easily be distinguished (Yun et al., 2001).

In their studies at a frequency of 1.4 GHz, Smolčić et al. (2008) and Bonzini et al. (2013) were able to distinguish the SFG and AGN populations from each other. For low flux densities between 30 and 100 μJy , the SFG starts to dominate the source population (Bonzini et al., 2013), whereas for higher flux densities radio-loud AGNs dominate.

1.3 Radio telescopes

In order to observe the radio continuum, two main types of ground-based telescopes are used. Depending on the desired frequency range and resolution of the survey, the sky is either observed with single-aperture telescopes or with arrays of dish telescopes, or simple dipoles. Most of the surveys used in this work were carried out with interferometers, therefore the main concepts of such telescopes are described in the following.

As the names of the two different concepts already suggest, the main difference between the single-aperture and the array of telescopes is the number of apertures used. The aperture itself usually consists of a receiver, which is generally a Hertzian dipole, and a collector, or a reflector. In Figure 1.5 two different concepts of radio telescopes are shown. The left panel shows the single-dish telescope in Effelsberg, Germany, which uses a parabolic reflector to focus the radiation towards the receiver at the tip of the

telescope. The right panel of Figure 1.5 shows a Low-Band Antenna (LBA) of the LOW Frequency ARray (LOFAR; van Haarlem et al. 2013). This antenna uses a relatively coarse steel grid as a reflector, while the cables going from the end of the grid to the tip of the central pole are the dipole elements.

The angular resolution θ of a telescope, both in optical and in radio, depends on the observed wavelength λ and the diameter D via (Airy, 1835; Rayleigh, 1879):

$$\theta = 1.22 \frac{\lambda}{D}. \quad (1.19)$$

Therefore the angular resolution at a given wavelength is only limited by the diameter of the telescope. Assuming typical wavelengths for radio and optical observations, like 1 m and 7×10^{-7} m, the angular resolution for a 100 m dish would be $\sim 2500''$ and $\sim 0.0018''$, respectively. The currently largest telescope for optical observations is a 10.4 m optical mirror used in the Gran Telescopio Canarias (GTC; Rodríguez-Espinosa and Alvarez Martin 1997), which would result in a angular resolution of $0.017''$. A radio telescope with comparable resolution at metre-wavelengths would need a diameter of 10^5 km.

In order to overcome structural limits of a single-dish aperture, multiple apertures are connected and used as a combined instrument. These arrays of single instruments use basic interferometry, based on the delayed arrival time of the signal between different antennas. The angular resolution is then defined by the baseline between the single instruments and not by the individual diameter of the apertures. Basic concepts of these radio interferometers use either steerable dish antennas to focus the beam at a chosen patch of the sky, or use ground based dipole antennas with software formed beams. The examples of Figure 1.5 show on the left a steerable single-dish telescope and on the right several ground based dipole antennas of LOFAR. In case of the Effelsberg telescope (Fig. 1.5 left), the instrument can either be used in single operation mode, or can be combined with other radio telescopes. An example of this combination is the Very Long Baseline Interferometry (VLBI), which connects telescopes across different countries and continents, while the Effelsberg telescope, for example, is used in the European VLBI Network (EVN). Other interferometers using parabolic dish apertures are for example the Very Large Array (VLA), consisting of 27 dishes with a diameter of 25 m, and the Westerbork Synthesis Radio Telescope (WSRT), consisting of 14 dishes. Both interferometers are also part of VLBI network, where the WSRT is part of the EVN, like the Effelsberg telescope. The LOFAR station ‘DE609’, shown in Figure 1.5 (right), itself consists of 96 Low-Band Antennas (LBA; 30-80 MHz) and 96 groups of 16 High-Band Antennas (HBA; 120-240 MHz). Therefore, each station can theoretically be seen as an interferometer, which can operate on its own in single station mode. However, the single stations use a combination of analog and digital beam-forming methods to create several distinct beams, which can be used to simultaneously observe different sources (van Haarlem et al., 2013). In order to form an even larger telescope, all of the 14 international LOFAR stations and the 38 LOFAR stations in the Netherlands can be used together, ranging from Irland to Poland in west-east direction and from Sweden to southern Germany in north-south direction.

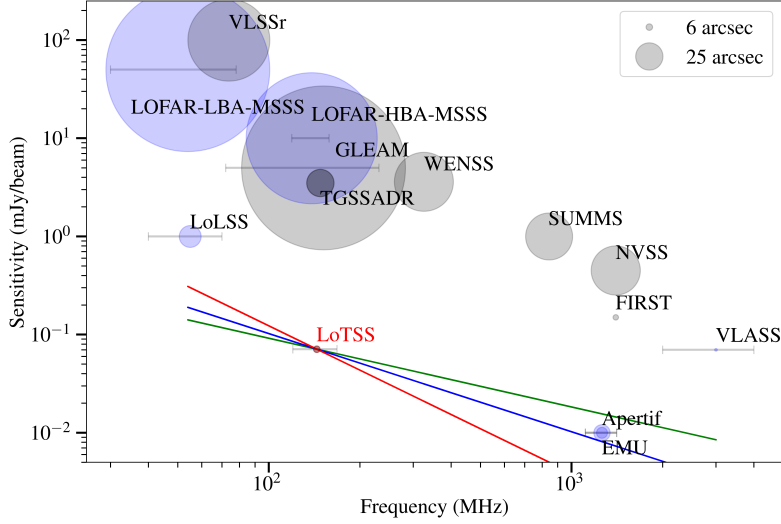


Figure 1.6: Sensitivity comparison of existing wide-area surveys (grey) with respect to the LoTSS-DR1 survey, extracted from Shimwell et al. (2019). The coloured lines correspond to equivalent sensitivities, scaled with spectral indexes of 0.7 (green), 1.0 (blue), and 1.5 (red).

1.4 Radio continuum surveys

Already before the discovery of the CMB, several missions and surveys have been started to observe the radio continuum, like the First Cambridge Catalogue of Radio Sources (1C; Ryle et al. 1950) and its successors. Depending on the epoch and instrument, the surveys observe the sky at different frequencies and sensitivities. A comparison of the sensitivity, observing frequency, and resolution of different wide-field surveys is shown in Figure 1.6 (Shimwell et al., 2019). The sensitivity of the most recent survey, the LoTSS-DR1, is scaled to different frequencies with three different spectral indexes to compare it better to other surveys. Additionally, the resolution of the surveys is sketched as grey circles in Figure 1.6. In order to get a simple overview of the surveys used in this work for direct measurements, or for comparison, the details of the surveys are briefly presented in the following. A short comparison of the main features of the surveys is presented in Table 1.1. This collection is without any claim of completeness and could be extended by studies of sub-samples of each survey, or combinations of surveys. Issues regarding the surveys, like positional dependencies of the sensitivity, are either discussed in the following, or directly in the corresponding sections.

The VLA Low-Frequency Sky Survey (VLSS; Cohen et al. 2007) is until now the only survey, which covers a large fraction of the full sky below 150 MHz. In order to observe at such low frequencies, the Very Large Array (VLA) was extended with 4 m wavelength receivers (Kassim et al., 1993; Kassim et al., 2007). For a sky coverage of 30 939 square degrees, the VLSS survey observes the sky at a central frequency of 73.8 MHz with a total bandwidth of 1.56 MHz. The survey produces images with a

resolution of $80''$ and a typical rms noise of $100 \text{ mJy beam}^{-1}$, from which 68 311 sources have been extracted (Cohen et al., 2007). Similar to its precursor, the NVSS survey (see below), the VLSS survey was observed in two different configurations in order to produce an uniform resolution.

The LOFAR Two-metre Sky Survey (LoTSS; Shimwell et al. 2017) is an ongoing project of the international LOw Frequency ARray (LOFAR; van Haarlem et al. 2013) using the HBAs, which had its first data release in 2019 (LoTSS-DR1; Shimwell et al. 2019). It will eventually cover the complete northern hemisphere at a central frequency of 144 MHz, with a bandwidth of 24 MHz. In the first data release, 325 694 sources in an area of 424 square degrees (HETDEX field) were detected. The observations are carried out with a resolution of $6''$ and with a median noise of $71 \mu\text{Jy beam}^{-1}$. A value added catalogue, where multi-component sources have been matched and artefacts have been removed, contains 318 520 sources. Out of these sources, 231 716 sources have optical or near-IR identifications in the Panoramic Survey Telescope and Rapid Response System (Pan-STARRS; Kaiser et al. 2002; Kaiser et al. 2010) and/or the Wide-field Infrared Survey Explorer (WISE; Wright et al. 2010). A second data release is expected to be publicly available in summer 2021, with roughly 5700 square degree coverage and in total up to 4.5 million sources. The first data release is 99% point source complete at a flux density threshold of 1 mJy, or for a more consistent sub-sample at 0.8 mJy (Siewert et al., 2020a).

The first Alternative Data Release of the the TIFR GMRT Sky Survey (TGSS³) was observed with the Giant Metrewave Radio Telescope (GMRT; Swarup 1991) in Puna, India, and was published by Intema et al. (2017, TGSS-ADR1). It observed 36 900 square degrees at a central frequency of 147.5 MHz with a bandwidth of 16.7 MHz. Due to bad ionospheric weather conditions, 33 pointings of the TGSS have not been included in the TGSS-ADR1, which results in an incomplete sky coverage in the north-east of the survey (see Fig. 6 of Siewert et al. 2020b). By re-processing the raw uncalibrated visibility data, Intema et al. (2017) found 623 604 radio sources in images with a resolution of $25'' \times 25''$ above 19 degree declination and $25'' \times 25'' / \cos(\delta - 19)$ below 19 degree declination. With a median rms noise of $3.5 \text{ mJy beam}^{-1}$ the catalogue is estimated to be complete above a flux density threshold of 100 mJy (Intema et al., 2017). In a study of large-scale anisotropies in the TGSS-ADR1, Tiwari et al. (2019) found large-scale flux systematics in the TGSS-ADR1 while comparing it to GLEAM flux densities.

The GaLactic and Extragalactic All-sky MWA (GLEAM; Hurley-Walker et al. 2017) survey, observed with the Murchison Widefield Array (MWA; Lonsdale et al. 2009; Tingay et al. 2013), covers the southern hemisphere with a frequency range between 72 and 231 MHz. Published images of the 24 831 square degrees covering catalogue are centred at 200 MHz, with a resolution of $2'$. In total, the radio source catalogue contains 307 455 sources south of $+30 \text{ deg}$. Contributions from the Galactic foreground to the catalogue are avoided by neglecting Galactic latitudes within $|b| \leq 10 \text{ deg}$. Additionally, areas with known structures, like the Magellanic Cloud, are excluded. The catalogue is estimated to be 90% complete at 170 mJy, but the completeness varies strongly with the declina-

³<http://tgss.ncra.tifr.res.in>

tion. In the zenith of the survey at -26.7 deg declination, the catalogue is already 95% complete at 160 mJy. In order to be 99% complete, the necessary flux density threshold has to be increased to 500 mJy for declinations below 18.5 deg, which will recover only 34 278 radio sources. Therefore, the survey is not widely used for cosmological studies yet.

Using the flux densities of the GLEAM survey, Hurley-Walker (2017) rescaled the flux density scale of the TGSS-ADR1. For declinations $\leq +30$ deg and a sky coverage of 18 800 square degrees, the new catalogue TGSS-RSADR1 contains 383 589 radio sources (see Fig. 2.5). By matching sources within $25''$, the author claims to reduce the position-dependent flux density scale variations of the TGSS-ADR1. The catalogue TGSS-RSADR1 is provided by the author only on request. Therefore, the studies in Section 2.3 have been done with the publicly available TGSS-ADR1. A more detailed study of these rescaled sources is presented in Section 2.4.4.

The Miyun Metre-wave aperture Synthesis Radio Telescope (MSRT; Beijing Observatory Metre-Wave Radio Astronomy Group 1986) of the Beijing Astronomical Observatory, consisting of 28 parabolic antennas with a diameter of 9 m, was used to produce a survey at 232 MHz, mapping nearly the complete northern hemisphere above declinations of $+30$ deg (Zhang et al., 1993). The data release has in total 34 426 sources, extracted from 152 fields with a resolution of $3'.8 \times 3'.8 / \cos(\delta)$ and an average rms noise of 50 mJy (Zhang et al., 1997).

The Westerbork Northern Sky Survey (WENSS; Rengelink et al. 1997) was a project to cover parts of the northern hemisphere ($\delta \geq +30$ deg) with the Westerbork Synthesis Radio Telescope (WSRT) in two different frequencies. The largest part of about 10 177 square degrees was observed at 325 MHz, whereas only 2298 square degrees were observed at 609 MHz (see Fig. 6 of Siewert et al. 2020b). For the low frequency survey, 229 420 sources were observed in maps with a resolution of $54'' \times 54'' / \cos(\delta)$ and a rms noise of $3.9 \text{ mJy beam}^{-1}$ and published as a source catalogue (de Bruyn et al., 2000).

The Sydney University Molonglo Sky Survey (SUMSS), observed with the Molonglo Observatory Synthesis Telescope (MOST) at 843 MHz, was published in a first data release by Mauch et al. (2003). It contained originally 107 765 radio sources in an incomplete region of 3500 square degrees of the southern sky with $\delta \leq -30$ deg. The produced images have a resolution of $45'' \times 45'' / \cos(\delta)$ and can be sub-divided into two sets, namely the southern $\delta \leq -50$ deg and the northern $\delta > -50$ deg, with limiting peak brightnesses of 6 mJy beam^{-1} and 10 mJy beam^{-1} , respectively. This initial release was estimated to be complete at 8 mJy in the southern part and at 18 mJy in the northern part. The survey was then completed and reprocessed (Murphy et al., 2007), containing in the end 210 412 radio sources in a region of 8100 square degrees in the southern sky without the galactic plane of $|b| \leq 10$ deg (see Fig. 6 of Siewert et al. 2020b).

The NRAO VLA Sky Survey (NVSS; Condon et al. 1998) was observed with the Very Large Array (VLA) in New Mexico, USA. It observed in an area of 33 813 square degrees 1 773 484 sources (see Fig. 6 of Siewert et al. 2020b). With an effective bandwidth of $\Delta\nu = 42$ MHz, the survey was observed at a central frequency of $\nu = 1.4$ GHz. Depending on the declination, the survey was observed with different configurations of

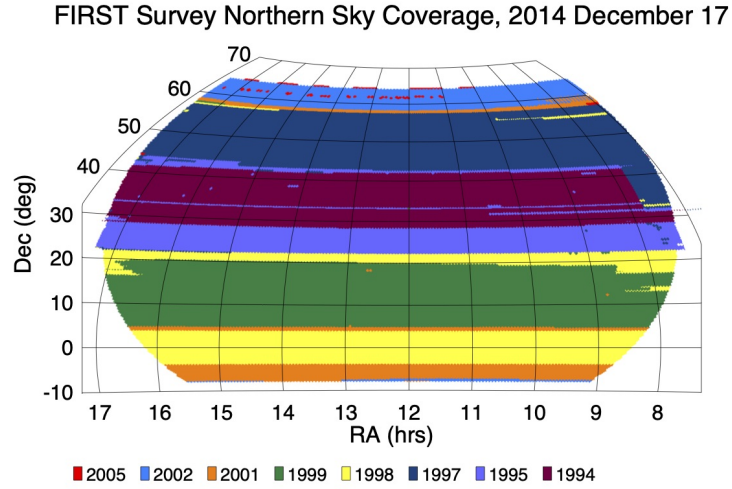


Figure 1.7: Final sky coverage of the north-galactic part of the FIRST survey (Helfand et al., 2015). The sky coverage of the different observation epochs are highlighted in different colours. [Downloaded from <http://sundog.stsci.edu>]

the VLA. The configurations are chosen, such that the system noise of the telescope is kept nearly constant. Additionally, the snapshot durations are increased with respect to the zenith of the telescope, which is located at a latitude of ~ 34 deg. Adjusting the snapshot time and the configuration, the survey yields rms brightness fluctuations of $\sigma_b = 0.45$ mJy beam $^{-1}$ with a FWHM resolution of $45''$. The corresponding source catalogue is limited to a lower flux density threshold of 2.5 mJy, which is the 50% completeness limit. For a point source completeness of 99% the flux density threshold has to be increased to 3.4 mJy.

At the same frequency of the NVSS survey, the VLA instrument is used to produce the collection of Faint Images of the Radio Sky at Twenty centimeters (FIRST; Becker et al. 1995). The FIRST survey in its final status covers 10 557 square degrees, while observing 946 432 radio sources (Helfand et al., 2015). Neglecting the Galactic plane, the sky coverage is splitted into two main parts of 8444 square degrees in the northern part and 2131 square degrees in the southern part. The northern part is exemplary shown in Figure 1.7 with the sky coverages of the different observation epochs. Due to several updates of the survey and the source catalogue, the images have a typical rms noise of 0.15 mJy beam $^{-1}$ with a resolution of $5''$. The final source catalogue is limited by the detection sensitivity of 1 mJy. Due to changes in the array configuration in the 20 years of observation, the central frequency, as well as the integration time, changes between different observation epochs. In order to avoid confusion from different frequencies and noise properties, older images are not mixed with more recent ones, which results in small gaps in the sky coverage of the latest source catalogue.

The Parkes-MIT-NRAO (PMN; Griffith and Wright 1993) survey was observed with the ANRAO 64 m single dish telescope in Parkes, Australia covering in total 23 242 square degrees from -87.5 deg to $+10$ deg in declination. The survey itself is split up into four regions, namely the Southern (Wright et al., 1994), Tropical (Griffith et al., 1994), Equatorial (Griffith et al., 1995) and the Zenith (Wright et al., 1996) survey. In total the radio source catalogues for the four surveys contain 50 814 sources observed at a central frequency of 4850 MHz with a bandwidth of 600 MHz and a spatial resolution of $4.2'$. Additional maps for the surveys haven been produced and published, i.e. for the Southern (Condon et al., 1993) and the Tropical (Tasker et al., 1994) survey, with a declination dependent rms noise of $5 - 10$ mJy beam $^{-1}$ and $9 - 11$ mJy beam $^{-1}$, respectively.

The NRAO 91 m single-dish telescope in Green Bank was used to produce three observations from 0 deg declination to $+75$ deg declination at a central frequency of 4850 MHz in three different epochs, namely November 1986, October 1987 and November 1988. Condon et al. (1989) produced from the 1987 observations a set of maps, covering 19 697 square degrees with a resolution of $3'.7 \times 3'.3$. These maps have a rms noise of 5 mJy, from which Gregory and Condon (1991) extracted 54 579 sources with flux densities stronger than $S \sim 25$ mJy.

In a later approach, Condon et al. (1994) used the observations of 1986, as well as the combination of 1986 and 1987 of the NRAO 91 m telescope in Green Bank, to produce a second set of maps, covering now 19 927 square degrees. Using the combined maps of the observation epochs 1986 and 1987, Gregory et al. (1996) produced a source catalogue consisting of 75 162 sources.

Table 1.1: Comparison of different radio surveys and their properties. Each survey is described by its central frequency (ν) and bandwidth ($\Delta\nu$), as well as its median noise and resolution. The observed survey area (Ω) and the observed number of sources (N) are compared without applying a flux density threshold.

Survey	ν (MHz)	$\Delta\nu$ (MHz)	Noise (mJy beam ⁻¹)	Resolution	Ω (sqdeg)	N	Instrument	Reference
VLSS	74	1.56	100	80''	30 939	68 311	VLA	Cohen et al. (2007)
LoTSS-DR1	144	24	0.071	6''	424	325 694	LOFAR	Shimwell et al. (2019)
TGSS-ADR1	147.5	16.7	3.5	25'' × 25''	36 900	623 604	GMRT	Intema et al. (2017)
GLEAM	200	159	10 – 28	2'	24 831	307 455	MWA	Hurley-Walker et al., 2017
MIYUN	232	1.5	50	3'.8 × 3'.8 / cos(δ)		34 462	MSRT	Zhang et al. (1997)
WENSS	325	5	3.9	54'' × 54'' / cos(δ)	10 177	229 420	WSRT	Rengelink et al. (1997)
SUMSS	843	3	6	45'' × 45'' / cos(δ)	8100	210 412	MOST	Murphy et al. (2007)
NVSS	1400	42	0.45	45''	33 813	1 773 484	VLA	Condon et al. (1998)
FIRST	1400	128	0.15	5''	10 575	946 432	VLA	Helfand et al. (2015)
PMN	4850	600	5 – 11	4'.2	23 242	50 814	ANRAO 64m	Griffith and Wright (1993)
87GB	4850	600	5	3'.7 × 3'.3	19 697	54 579	NRAO 91m	Gregory and Condon (1991)
GB6	4850	600				75 162	NRAO 91m	Gregory et al. (1996)

1.5 Measures of Large-Scale Structures

1.5.1 Counts-in-cells

Assuming the cosmological principle, the observed distribution of sources on the sky should be completely random. This underlying point process is often described by a Poisson distribution. Variations from the cosmological principle, like clustering and/or large-scale structures will lead to statistical variations from the Poisson distribution. In the following, the Poisson distribution and possible deviations from it are discussed. The derivations in this section follow the book of Kingman (2010).

The Poisson distribution $\mathbb{P}(\mu)$ is related to the source counts in the sense that the random variable N , which is just the number of sources in a given subset $A \subset \Omega$ of the whole sky Ω , has the probability $P(N(A) = n)$ to take the possible value $n > 0$ (following Kingman 2010):

$$P(N(A) = n) = \mathbb{P}_n(\mu(A)) = (\mu(A))^n \frac{e^{-\mu(A)}}{n!}, \quad (1.20)$$

with $\mu(A)$ the mean and $\mathbb{E}[N(A)] = \mu(A)$ the expectation, as well as the variance $\mathbb{V}[N(A)] = \mu(A)$. For mathematical correctness, one has to assume the subsets to be measurable with a simple counting process $\# : A \rightarrow \mathbb{N}$, $\#(A) = N \in \mathbb{N}$, like the cardinality. For this example, we assume that the space Ω is of dimension 2 and a subset of \mathbb{R}^2 . The subsets $A_i \subset \Omega$ are disjoint and the union $\bigcup_i A_i = \Omega$. Furthermore, we assume that the numbers $N(A_i)$ are independent, which leads to the total number of sources $N(\Omega) = \sum_i N(A_i)$. The expectation value for the whole sky can be assumed as $\mu(\Omega) = \sum_i \mu(A_i)$ and is also called the mean measure. In our case the mean measure can be described with the number density or intensity ρ :

$$\mu(\Omega) = \iint_{\Omega} \rho(\phi, \theta) d\phi d\theta. \quad (1.21)$$

For an uniform and homogeneous density the equation simplifies to $\mu(\Omega) = \rho|\Omega|$, with $|\Omega|$ the area of Ω . The same calculation can be done for the subsets ($\mu(A_i) = \rho|A_i|$). If the density is inhomogeneous across the sky, like for overdensities in clusters of galaxies, or in the Galactic plane, we are not able to simplify the mean measure. In most common cases, the mean measure will be defined by the arithmetic mean:

$$\mu = \frac{1}{a} \sum_{i=0}^a N_i, \quad (1.22)$$

with a the number of subsets (A_i) and $N_i = N(A_i)$ the number of sources in these subsets. In the following, the subsets A_i are the equal area pixels formed with HEALPIX⁴ (Górski et al., 2005) and we assume a homogeneous density. The corresponding pixels for a HEALPIX resolution of $N_{\text{side}} = 16$ cover ~ 13.43 square degrees. Assuming

⁴<http://healpix.sourceforge.net>

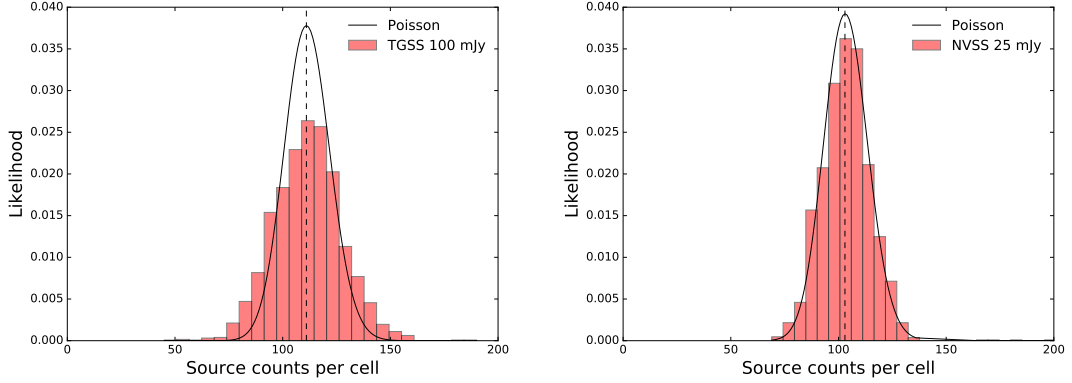


Figure 1.8: Source count distribution (red bars) of the TGSS-ADR1 (*left*) and NVSS survey (*right*), with 100 mJy and 25 mJy flux density thresholds, respectively. The Poisson distribution (black dots) with mean of the source count distribution (back dashed) is plotted on top.

typical extragalactic sources with redshifts $z > 0.1$, the assumed pixel size corresponds to distances > 100 Mpc. Therefore, we can expect the assumption of the cosmological principle to hold true and statistical fluctuation of the source counts, like clusters, are negligible. Using the pixelisation scheme of HEALPIX, we simplify the notation:

$$A_i \rightarrow A$$

$$\mu(A_i) \rightarrow \mu$$

$$N(A_i) \rightarrow N$$

In order to obtain the probability to find exact or less sources per pixel ($x \leq N$) than a given number, one has to sum over all probabilities:

$$P(x \leq N) = \sum_{x=0}^N \mu^x \frac{e^{-\mu}}{x!}. \quad (1.23)$$

The source count distribution of the TGSS-ADR1 (*left*) and NVSS (*right*) survey are shown in Figure 1.8 with the corresponding Poisson distribution (black curve). The arithmetic mean of the source count distribution (black dashed line) is used as mean measure for the Poisson distribution. By eye, the observed source count distribution differs strongly from a Poisson distribution for the TGSS-ADR1 100 mJy sample. In case of the NVSS 25 mJy sample, a Poisson distribution agrees much better with the observed source counts. Several contributions to the source count distribution, like different galaxy populations, projection effects, and multicomponent sources, or groups of sources, are discussed in the following.

Previously, we assumed that only one population of sources exists, which lead to one Poisson process on the sky. Assuming different populations of sources, like AGNs and

SFGs, we have to take a separate Poisson process into account for each population. The combined probability of two overlapping Poisson processes, with independent random variables N and M and Poisson distributions $\mathbb{P}(\mu)$ and $\mathbb{P}(\lambda)$, is:

$$P(N = n, M = m) = P(N = n)P(M = m) = \frac{\mu^n e^{-\mu}}{n!} \frac{\sigma^m e^{-\sigma}}{m!}. \quad (1.24)$$

To quantify if the joint number $N + M$ is also Poisson distributed, we have to sum over all possible values of n , while assuming $n + m = r$ to be constant:

$$\begin{aligned} P(N + M = r) &= \sum_{n=0}^r P(N = n)P(M = r - n) \\ &= \sum_{n=0}^r \frac{\mu^n e^{-\mu}}{n!} \frac{\sigma^{(r-n)} e^{-\sigma}}{(r-n)!} \\ &= \frac{(\mu + \sigma)^r e^{-(\mu + \sigma)}}{r!}. \end{aligned} \quad (1.25)$$

Thus $N + M$ has the distribution $\mathbb{P}(\mu + \sigma)$, which can be extended to any finite number of independent random variables. For a countable collection of n populations and therefore independent Poisson processes Π_n , with mean measure μ_n , the superposition is:

$$\Pi = \bigcup_n \Pi_n, \quad (1.26)$$

which is a Poisson process with

$$\mu = \sum_n \mu_n. \quad (1.27)$$

Therefore, the number counts per pixel would only change like $N + M = n + m$.

So far, we only looked at a two dimensional sky. In general the galaxy distribution on the sky is a projection from the higher dimensional Universe. It is not obvious, how a projection or mapping of a Poisson process would change the mean measure or in general if the projection is still a Poisson process. For simplicity, we assume the Universe to be a subset $A \subset \mathbb{R}^3$, which will be projected onto the two-sphere $S^2 = \{(\phi, \theta, r) : \phi \in [0, \pi], \theta \in [0, 2\pi], r = \text{const} \in \mathbb{R}\}$ in spherical coordinates with $f : A \rightarrow S^2$. In general the transformed points should form another Poisson process on the new state space. Unfortunately, two or more projected galaxies can result in only one new point on the projected sphere, like extended sources hiding point sources. However, the vast majority of the radio sources in the TGSS-ADR1 source catalogue are point-like with respect to the beam size of the survey (see Fig. 1.9). Based on the observed sky coverage of the TGSS-ADR1 and the assumption of point-like sources with sizes comparable to the beam size, the occupational sky coverage for the total number of sources is $\sim 0.6 \times 10^{-3}$. Therefore, the assumption of the atomic measure is still satisfied in case of the TGSS-ADR1.

In the latter, we assumed a well-known value for the mean measure, but in general the mean itself can be distributed with other probability distributions. While we assume

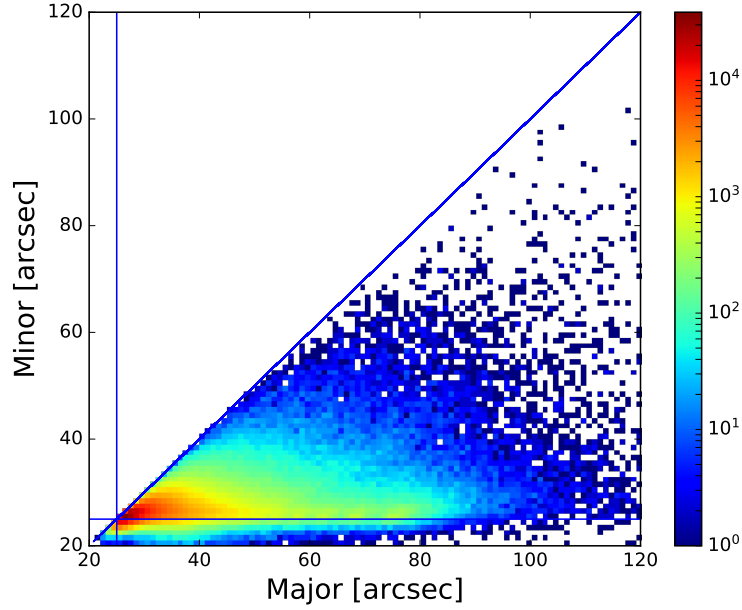


Figure 1.9: Histogram of the major and minor axes of the TGSS-ADR1 sources. The vertical and horizontal line corresponds to the beam size of the TGSS of $25'' \times 25''$.

for the probability to find n sources per pixel, with the mean μ :

$$P(n, \mu) = \frac{\mu^n}{n!} e^{-\mu}, \quad (1.28)$$

the mean can be normal distributed with:

$$P(\mu, \bar{\mu}, \sigma) = \frac{1}{\sqrt{2\pi}\sigma} \exp\left(-\frac{(\mu - \bar{\mu})^2}{2\sigma^2}\right), \quad (1.29)$$

which can be constructed from the assumption, that the number counts scale with $N(>S) \propto S^{-x}$. Therefore, if we apply a flux density threshold to the data, the number counts would depend on the gaussian error of the flux ($S \pm \Delta S$) at the threshold itself. If we now fold the Poisson process with the distribution for the mean, we can show that:

$$P(n; \bar{\mu}, \sigma) = \int_0^\infty \frac{1}{\sqrt{2\pi}\sigma} \exp\left[-\frac{1}{2}\left(\frac{\mu - \bar{\mu}}{\sigma}\right)^2\right] \frac{\mu^n e^{-\mu}}{n!} d\mu. \quad (1.30)$$

A negative lower limit for the integral would be unreasonable for the mean measure of radio sources and for simplicity we set it to 0. The $\bar{\mu}$ can be constructed from theoretical calculations of the differential source counts (Peper, 2017), cast to the size of one pixel. Now we can perform a maximum likelihood test to get an approximation for $\bar{\mu}$ and σ from

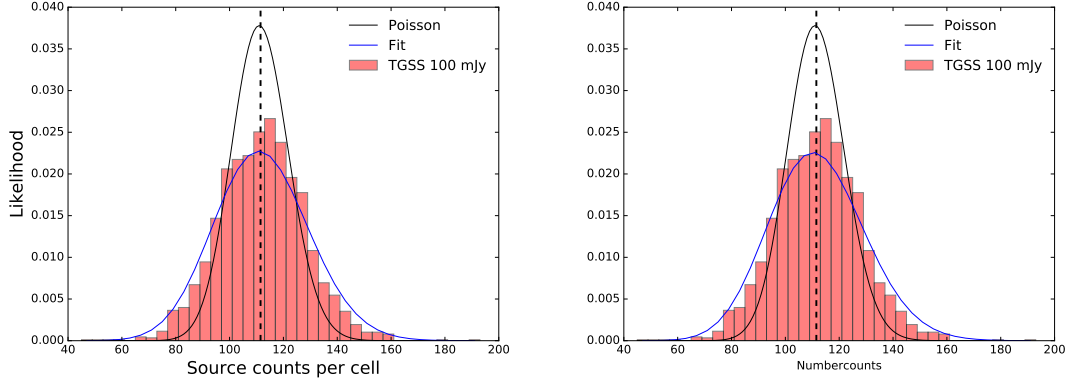


Figure 1.10: Compound distribution (blue line) of a Poisson and Normal distribution (*left*), and of two Poisson distributions (*right*) fitted to the source counts per cell (red bars) of the TGSS-ADR1 with a flux density threshold of 100 mJy.

the data. Therefore, we do a chi-square test with the hypothesis of a Poisson distribution folded with a normal distribution:

$$\chi^2 = \sum_{i=1}^n \frac{(c_i - P(i; \bar{\mu}, \sigma))^2}{P(i; \bar{\mu}, \sigma)}, \quad (1.31)$$

with c_i the relative frequency of i number counts and $P(i; \bar{\mu}, \sigma)$ the probability to find i sources. In this case, $\bar{\mu}$ corresponds to the mean of the Poisson distribution and σ to the standard deviation of the normal distribution, which is used to determine the distribution of the mean. For the TGSS-ADR1 with a flux threshold of 100 mJy, the test results in $\bar{\mu} = 112$ and $\sigma = 14$ with a $\chi^2 = 0.015$ (see Fig. 1.10 left).

If we assume that we have besides Quasars, which are most likely single point sources, also FR I and FR II Radio Galaxies in our sample, we have to think about a distribution for the points associated with one physical source. Depending on the frequency, resolution, and sensitivity of the survey, several components of a source, like core and lobes, can be detected separately or as a single source. In Figure 1.11 the same sources are observed with NVSS (left), FIRST (middle), and LoTSS (right). Because of the underlying physics, not all extended components of a source can be detected, like lying beneath the flux threshold, or they are spatially obscured by other components of the source. In comparison, the detection of source components can be simulated by a point process, like a Poisson distribution. Therefore, we are folding the Poisson distribution with a second Poisson. The resulting distribution is called Compound Poisson. This Poisson distribution should affect the overall distribution in the mean measure, like in the case of the normal distribution. First, we have a Poisson distribution for the sources across the sky with mean λ :

$$P(N) = \frac{\lambda^N e^{-\lambda}}{N!} \quad (1.32)$$

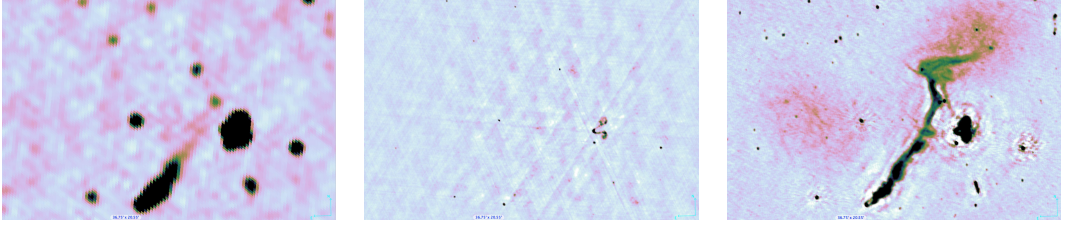


Figure 1.11: Radio image of the same source from the NVSS (*left*), FIRST (*middle*), and LoTSS (*right*) survey. [Credit: Tim Shimwell and LOFAR Survey KSP]

and secondly, we have a Poisson distribution for the components of a source with mean μ :

$$P(n_i) = \frac{\mu^{n_i} e^{-\mu}}{n_i!}, \quad (1.33)$$

while we have N Poisson variables n_i and the total number of sources:

$$r = \sum_{i=1}^N n_i. \quad (1.34)$$

If we now construct such a distribution:

$$P(r) = \sum_N P(r|N)P(N), \quad (1.35)$$

$$\Rightarrow P(r) = \sum_{N=0}^{\infty} \left[\frac{(N\mu)^r e^{-N\mu}}{r!} \frac{\lambda^N e^{-\lambda}}{N!} \right], \quad (1.36)$$

the expectation value should not change in comparison to a single Poisson distribution with mean μ_0 , therefore, it is fixed to $\mathbb{E}(N) = \mu\lambda = \mu_0$. The variance, on the other hand, will change like:

$$\mathbb{V}[r] = \lambda\mu(1 + \mu) \quad (1.37)$$

We can now apply the maximum likelihood method to get an approximation for μ and λ from the data. Therefore, we do a chi square test with the hypothesis of a Compound Poisson distribution

$$\chi^2 = \sum_{i=1}^n \frac{(c_i - P(i; \mu, \lambda))^2}{P(i; \mu, \lambda)} \quad (1.38)$$

with c_i the relative frequency of i number counts and $P(i; \mu, \lambda)$ the probability to find i sources. For the TGSS-ADR1 with a flux threshold of 100 mJy, the fit results in $\mu = 112$ and $\lambda = 1.8$ with a $\chi^2 = 0.016$ (see Fig. 1.10 right).

A more detailed analysis of the one-point statistics and higher moments, like skewness and kurtosis of the Poisson and Compound Poisson distributions in case of the LoTSS-DR1 survey, is shown in Siewert et al. (2020a).

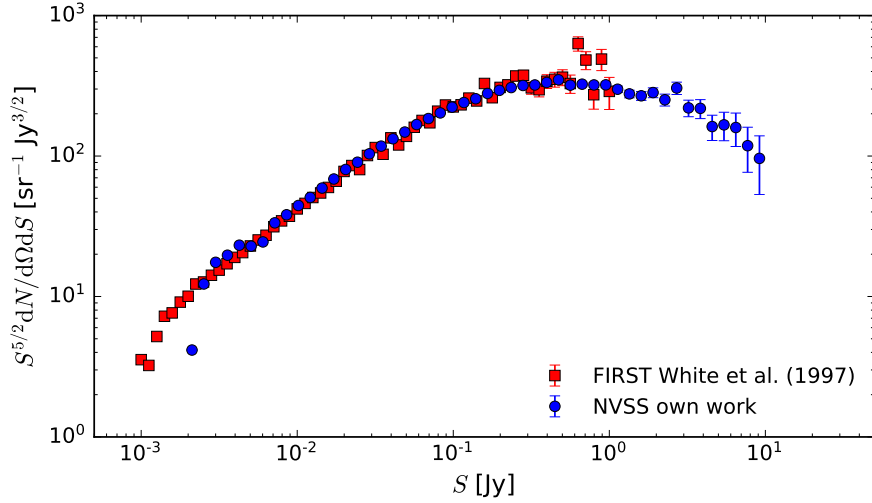


Figure 1.12: Differential source counts for the FIRST (blue, White et al. 1997) and NVSS (red) survey, weighted with $S^{5/2}$.

1.5.2 Differential number counts

As simple as the counts-in-cell statistics, the calculation of the measurement for cosmological studies are the integral or differential source counts. These source counts are typically computed as a function of flux density and/or redshift and are often depicted per unit volume. The differential source counts can reveal the cosmic evolution of galaxies and test cosmological models, by either comparing the observed counts to analytical models, or by fitting numerical calculations. More previously, the integrated source counts as a function of flux density have been widely used, which can easily be described by the amount of sources above a given flux density threshold. In contrast to the differential source counts, the integrated counts are not statistically independent with respect to the flux density and changes in the distribution can easily be burrowed in statistical errors.

The relevantly easy counting of sources makes this cosmological measurement accessible for every possible source catalogue. In order to connect these counts to cosmology, we start with the assumption that the source counts follow the luminosity function $\phi(L)$ via (following Weinberg 1972; Schechter 1976):

$$\frac{dN}{dV} = \phi(L)dL, \quad (1.39)$$

with $dV = a^3 r^2 dr dV$ and $a_0 r = d_c$ for a flat universe and a luminosity function $\phi(L_\nu)$ we get:

$$\frac{dN}{d\Omega dr} = \phi(L_\nu) dL_\nu a_0 d_c^2(z). \quad (1.40)$$

With the comoving distance:

$$d_c(z) = \frac{c}{H_0} \frac{1}{\sqrt{\Omega_k}} \sinh \left(\sqrt{\Omega_k} \int_0^z dz' \frac{H_0}{H(z')} \right) \quad (1.41)$$

for the today's Hubble rate H_0 and the dimensionless curvature parameter Ω_k , the relation between specific luminosity L_ν and flux density S can be written as:

$$L_\nu = 4\pi(1+z)^{1+\alpha}d_c^2(z)S, \quad (1.42)$$

with a spectral index α and $S \propto \nu^{-\alpha}$. Combining Equation (1.40) and (1.42) leads to the most general form of the differential source counts:

$$\frac{dN}{d\Omega dS dz} = 4\pi(1+z)^{1+\alpha}d_c^4(z)\frac{1}{H(z)}\phi(L_\nu). \quad (1.43)$$

By integrating over the redshift one can get the most common form of differential source counts per unit area and flux density:

$$\frac{dN}{d\Omega dS} = 4\pi \int_0^\infty dz (1+z)^{1+\alpha}d_c^4(z)\frac{1}{H(z)}\phi(L_\nu). \quad (1.44)$$

In order to further simplify the differential source counts, a specific luminosity function, like the Schechter function (Schechter, 1976), has to be assumed. In order to present measured differential source counts, the counts are weighted with $S^{5/2}$ to compensate steep slopes. Historically, the source counts are also often normalised to one at 1 Jy by dividing them with $k_0S^{-5/2}$. The slope $S^{-5/2}$ is the usual expectation for the differential source counts in a static Euclidean universe, which can easily be shown by integrating Equation (1.39) over the volume element $r^2 \sin\theta dr d\theta d\phi$ and taking the derivative with respect to dS .

To give an example of the weighted differential source counts, the measured source counts of the FIRST and NVSS survey at 1.4 GHz are shown in Figure 1.12. In case of the FIRST survey, the differential source counts have been extracted from White et al. (1997), who used the initial 1550 square degree field of the FIRST survey. The source counts of the NVSS survey (Condon et al., 1998) have been derived using the code shown in App. A.1 for 66 bins between 10^{-3} Jy and 10 Jy. The significant steepening at flux densities below 3×10^{-3} Jy for the NVSS and 2×10^{-2} Jy for the FIRST survey corresponds to their completeness limit. In an intermediate range of flux densities, the source counts of FIRST and NVSS shows a similar slope, which peak at 0.5 Jy. For brighter sources, the source counts flatten out and vary more strongly due to increased shot noise contributions.

A more detailed study of differential source counts from sub-samples of the LoTSS-DR1 is presented in Siewert et al. (2020b) (see Sect. 4). Furthermore, the differential source counts of the LoTSS-DR1 value added catalogue are compared in Siewert et al. (2020b) to simulated source catalogues of T-RECS (Bonaldi et al., 2019) and SKADS (Wilman et al., 2008). This comparison of differential source counts of observed and simulated sources is extended by a LOFAR deep-field study of the Lockman Hole, the Boötes, and the Elais-N1 regions (Mandal et al., 2020). In both of these studies (Siewert et al., 2020a; Mandal et al., 2020), the differential source counts are in good agreement to the expectations of the simulated source catalogues, besides a small lack of observed sources in a flux density range 3-12 mJy and 2-20 mJy, respectively.

1.5.3 Angular two-point correlation function

Besides the counts-in-cells statistics and the differential source counts, another measurement based on the spatial source distribution can be informative about the structure of the Universe and its composition. The angular two-point correlation function $w(\theta)$ is defined as the excess probability to find a galaxy at angular distance θ to a fixed galaxy within the solid angle $d\Omega$ (Peebles, 1980):

$$dP = \rho [1 + w(\theta)] d\Omega. \quad (1.45)$$

The excess is measured in the context of the mean number density ρ . Besides measuring the excess of the source density on a celestial sphere, it is possible to measure the spatial correlation function $\xi(r)$ as a function of the radial distance r between two sources (Peebles, 1980):

$$dP = n [1 + \xi(r)] dV. \quad (1.46)$$

Both correlation functions can be connected by the so called Limber equation and under the assumption of small angular source separations θ (Limber, 1953; Simon, 2007):

$$w(\theta) = \int_{-\infty}^0 d\bar{r} p_1(\bar{r}) p_2(\bar{r}) \int_{-\infty}^{+\infty} \Delta r \xi(\bar{R}, \bar{r}), \quad (1.47)$$

with $\bar{r} = (r_1 + r_2)/2$, $\Delta r = r_2 - r_1$, and $\bar{R} = \sqrt{\bar{r}^2 \theta^2 + \Delta r^2}$ for the radial source positions $r_{1,2}$, separated by the angle θ . Additionally, the filters $p_{1,2}$ project the Euclidean density contrast of sources onto a sphere. Assuming a power law of the form $\xi(r) = (r/r_0)^{-\delta}$ for the spatial correlation function, the angular two-point correlation function follows (Totsuji and Kihara, 1969; Peebles, 1980):

$$w(\theta) = A \left(\frac{\theta}{\theta_0} \right)^{-\gamma}, \quad (1.48)$$

with A the angular correlation amplitude at the angular pivot scale θ_0 , which is typically assumed to be 1 deg, and $\gamma = \delta - 1$. Early measurements of the angular two-point correlation reported the slope in the definition of Equation (1.48) to be $\gamma = 0.8$.

The angular two-point correlation can be measured by counting the galaxy-galaxy pairs $N_{gg}(\theta)$ at separation angle θ (Peebles, 1980). Landy and Szalay (1993) proposed an optimal estimator for the angular two-point correlation function:

$$\hat{w}(\theta) = \frac{DD - 2DR + RR}{RR}, \quad (1.49)$$

which compares the normalised galaxy-galaxy counts (DD) to counts of galaxy-random pairs (DR) and random-random pairs (RR) from a random sample with the same sky coverage. The normalised counts are defined by (Landy and Szalay, 1993; Roche et al.,

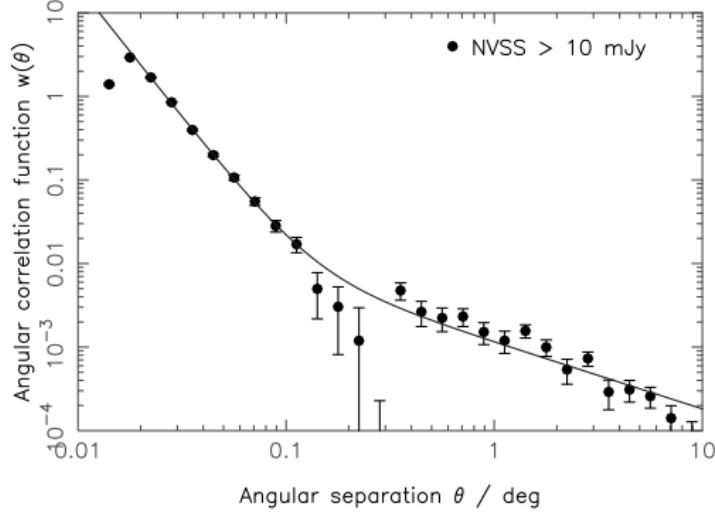


Figure 1.13: Angular two-point correlation function for the NVSS survey with 10 mJy flux density threshold from Blake and Wall (2002) and Blake et al. (2004). The best fitted power law, similar to Eq. (1.48), is shown as a black line.

2002):

$$DD = N_{gg}(\theta), \quad (1.50)$$

$$DR = \frac{(N_g - 1)}{2N_r} N_{gr}(\theta), \quad (1.51)$$

$$RR = \frac{N_g(N_g - 1)}{N_r(N_r - 1)} N_{rr}(\theta), \quad (1.52)$$

with N_i the total number of sources of the corresponding sample and N_{ij} the number of pairs at a given angular separation. A comparison of the performance of the estimator and its variance to other estimators from the literature is shown in Siewert et al. (2020a) (see Section 4.4) and Biermann (2019). Measurements with the estimator of Landy and Szalay (1993) and with an estimator suggested by Hamilton (1993) for different surveys are compared in Section 4.7. An example for the measured angular two-point correlation function for the NVSS survey with a flux density threshold of 10 mJy is shown in Figure 1.13 (Blake and Wall, 2002; Blake et al., 2004). The power law of Eq. (1.48) was fitted to angular separations $\theta > 0.3$ deg with best-fit values of $A = (1.49 \pm 0.15) \times 10^{-3}$ and $\gamma = 1.05 \pm 0.10$ (Blake et al., 2004). A more detailed description of the results and a comparison to other results from the literature (e.g. Rengelink 1999; Overzier et al. 2003; Rana and Bagla 2019) is presented in Section 4.7. In general for the fitted angular separations, the measurements commonly observe a clustering amplitude of, or below a percent, which is in agreement with the cosmological principle. For smaller angular separations galaxy clusters and multicomponent sources become more prominent, which increase the observed clustering.

For any radio survey, the observed sky is incomplete, which can affect the estimation of the angular two-point correlation by a negative offset, called integral constraint. The offset w_Ω of the estimated $\hat{w}(\theta)$ with respect to the true angular two-point correlation function $w(\theta)$:

$$\hat{w}(\theta) = w(\theta) - w_\Omega, \quad (1.53)$$

can be calculated by integrating an assumed true $w(\theta)$ over the observed sky Ω (Roche et al., 2002):

$$w_\Omega = \frac{1}{\Omega^2} \iint w(\theta) d\Omega_1 d\Omega_2. \quad (1.54)$$

Assuming the power law of Equation (1.48) and assumed true values for A and γ , the integral constraint can be written as (Roche et al., 2002):

$$w_\Omega = \frac{\sum RR \cdot A\theta^{-\gamma}}{\sum RR}. \quad (1.55)$$

In general, the angular two-point correlation function can be connected to the angular power spectrum C_l by (Peebles, 1980):

$$w(\theta) = \frac{1}{4\pi} \sum_{l=2}^{\infty} (2l+1) C_l P_l(\cos \theta), \quad (1.56)$$

with a sum over the Legendre Polynomials P_l . The sum is taken over the multipole moments l , starting with $l = 2$ and neglecting the monopole and dipole contributions, whereas the upper limit is mostly constraint by the desired numerical accuracy. By definition, the monopole vanishes and the dipole is expected to be of sub-dominant order, for details see Appendix D of Siewert et al. (2020a). The connection can be used to study the evolution of the Universe by comparing it to existing models and fitting cosmological parameters via simulations. In Section 4.5.3 to 4.6, as well as in Siewert et al. (2020a), the Equation (1.56) is used to compare the measured angular two-point correlation function to simulations based on best-fit Λ CDM-cosmology parameters from Planck Collaboration et al. (2018b).

1.5.4 Cosmic Radio Dipole

Following the discovery of the Cosmic Microwave Background (CMB), scientists early observed a prominent dipole anisotropy in the temperature of the CMB (e.g. see Fig. 1.14). This dipole of sub-percent order is assumed to be caused by the proper motion of the Solar System with respect to the rest frame of the CMB. Assuming a purely kinematic nature with velocity v of the CMB dipole, it can be modelled in first order of $\beta = v/c$ (Peebles and Wilkinson, 1968) by:

$$T(\theta) \approx T_0(1 + \beta \cos \theta), \quad (1.57)$$

with θ the angle between the line of sight and the dipole direction, and v the velocity of the proper motion. The cosmological principle states that the Universe should be statistically isotropic and homogenous from every point of view. Therefore the kinematic

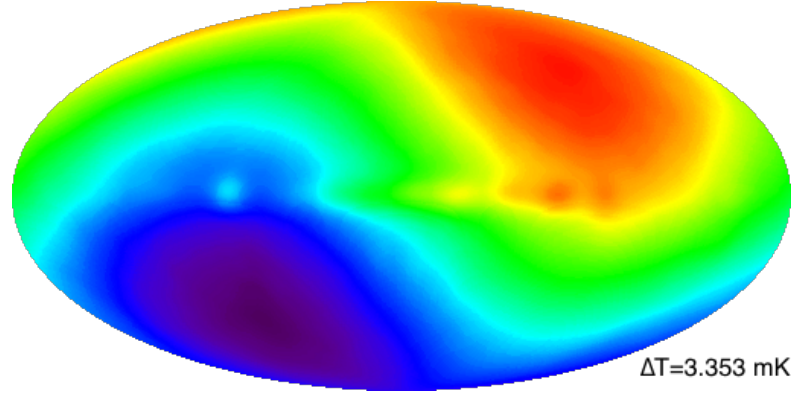


Figure 1.14: Observed dipole anisotropy of the Cosmic Microwave Background in the four-year sky map of COBE (Bennett et al., 1996). The map is shown in galactic coordinates [Obtained from <https://lambda.gsfc.nasa.gov>].

dipole should affect all frequencies of light emitted by visible matter. Several additional contributions to the dipole can be thought of, mostly caused by local structure, which is not covered by the statistical homogeneity of the cosmological principle. Observing the dipole anisotropy in the radio spectrum, the sky is dominated by extragalactic sources, like radio galaxies and quasars, which trace large-scale structures. Rejecting local structures, the observed Cosmic Radio Dipole should be dominated by the proper motion.

The kinematic term of the Cosmic Radio Dipole can be described by two different phenomena, depending on the proper motion of the observer with respect to the rest frame of the observed galaxies (Ellis and Baldwin, 1984). Basically, the effects are described by a Doppler shift from the emitted to the observed frequency, which will change the observed flux density, and by an additional aberration effect, which will result in a change of the observed angle.

The derivation of the boosted source counts, which is described in the following, follow mostly the work of Ellis and Baldwin (1984). The effect of Doppler shifting is described by:

$$\nu_{\text{ob}} = \delta(v, \theta) \nu_{\text{em}} \quad (1.58)$$

with

$$\delta(v, \theta) = \frac{1 + \frac{v}{c} \cos(\theta)}{\sqrt{1 - \frac{v}{c}}}. \quad (1.59)$$

Using the common description for the flux density:

$$S \propto \nu^{-\alpha}, \quad (1.60)$$

with the spectral index α and the Doppler shift, we can rewrite the observed flux density in terms of emitted flux density with the observed frequency:

$$S_{\text{obs}}(\nu_{\text{obs}}) = S_{\text{rest}}(\nu_{\text{obs}}) \delta^{1+\alpha}. \quad (1.61)$$

If we now describe the number counts of radio sources by a power law as a function of the flux density with index x :

$$\frac{dN}{d\Omega}(> S) \propto S^{-x}, \quad (1.62)$$

the observed source counts will depend on the emitted flux density in the rest frame of the sources by:

$$\left. \frac{dN}{d\Omega} \right|_{\text{obs}} = \left. \frac{dN}{d\Omega} \right|_{\text{rest}} \delta^{x(1+\alpha)}. \quad (1.63)$$

On the other hand, the position of each source will change towards the direction of motion and the observed angle between the source and the direction of motion will change as:

$$\tan \theta_{\text{obs}} = \frac{\sin \theta_{\text{rest}}}{\beta + \cos \theta_{\text{rest}}} \gamma^{-1}, \quad (1.64)$$

which will change the observed solid angle by:

$$d\Omega_{\text{obs}} = d\Omega_{\text{rest}} \delta^{-2}. \quad (1.65)$$

Combining both effects, the observed number counts per solid angle change from the number counts in the rest frame of the sources like:

$$\left. \frac{dN}{d\Omega} \right|_{\text{obs}} = \left. \frac{dN}{d\Omega} \right|_{\text{rest}} \delta^{2+x(1+\alpha)}. \quad (1.66)$$

Approximating δ in first order of β , the observed number counts can be written as:

$$\left. \frac{dN}{d\Omega} \right|_{\text{obs}} = \left. \frac{dN}{d\Omega} \right|_{\text{rest}} \{1 + [2 + x(1 + \alpha)]\beta \cos \theta\} \quad (1.67)$$

In a recent study of the CMB, Planck Collaboration et al. (2018a) found the dipole velocity to be $v = 369.82 \pm 0.11$ km/s. Defining the dipole amplitude by:

$$d = [2 + x(1 + \alpha)]\beta, \quad (1.68)$$

the Solar velocity can be translated to a dipole amplitude of $d = 4.62 \times 10^{-3}$. For this translation, the spectral index and the slope of the number counts are assumed to be $\alpha = 0.75$ and $x = 1$. Measurements of the Cosmic Radio Dipole using different surveys at different frequencies (e.g. Blake and Wall 2002; Singal 2011; Rubart and Schwarz 2013) revealed a dipole amplitude, which is increased by factors of four to five in comparison to the CMB dipole. A detailed comparison of the measurements is done in the Section 2, especially in App. A of the publication Siewert et al. (2020b). Possible explanations for the increased dipole amplitude are also discussed in Siewert et al. (2020b) and the following sections.

Chapter 2

Estimators of the Cosmic Radio Dipole

The publication of this chapter addresses two different estimators of the Cosmic Radio Dipole, where in the first part a linear estimator from the literature is analysed in terms of possible biases from masking and selection effects.

In the second part a quadratic estimator is established and tested for influences of the masking procedure and insufficient source densities. This quadratic estimator was firstly introduced in the doctoral thesis of Matthias Schmidt-Rubart (2015) and is additionally used in two publications of forecasting possible radio dipole measurements (Bengaly et al., 2019; Square Kilometre Array Cosmology Science Working Group et al., 2020) in terms of the upcoming Square Kilometre Array (SKA). The results of these forecasts are presented in Section 3.3 and 3.4.

The third part of the publication shows the application of the quadratic estimator to source catalogues of four different radio surveys, namely the TGSS-ADR1, WENSS, SUMSS, and NVSS. The surveys cover a frequency range between 147 MHz and 1.4 GHz. Regarding to this application, a common masking scheme is introduced for all four surveys. The masks handle the coverages and possible systematics of the surveys, like available noise properties. To address the differences in the dipole amplitude found between the TGSS-ADR1 and NVSS, both catalogues are crossmatched and a common catalogue is analysed.

The publication is additionally extended by a comparison of different dipole estimates from the literature (e.g Blake and Wall 2002; Singal 2011; Gibelyou and Huterer 2012; Rubart and Schwarz 2013).

In order to summarize the results of the publication (Siewert et al., 2020b, see chapter 2.3), we compare the linear and quadratic estimator in Section 2.1. The main results of the Cosmic Radio Dipole search for the TGSS-ADR1, WENSS, SUMSS, and NVSS radio source catalogues are summarised in Section 2.2. Supplementary materials, like a different fitting routine and results from a rescaled TGSS-ADR1 catalogue are shown in Section 2.4.

2.1 Comparison of a linear and a quadratic estimator

For the purpose to measure the Cosmic Radio Dipole, several estimators have been introduced in the literature (e.g. Crawford 2009; Blake and Wall 2002; Singal 2011; Bengaly et al. 2018). Most of these estimators use either directly the source positions, or the source density based on counts per cells or on hemispheres, to calculate the dipole direction and amplitude.

In the publication Siewert et al. (2020b), we analyse a linear estimator of the form (Crawford, 2009; Rubart and Schwarz, 2013):

$$\vec{R}_{3D} = \sum \vec{r}_i, \quad (2.1)$$

which uses the source positions \vec{r}_i to calculate the dipole amplitude and dipole direction. In more detail, the dipole direction is estimated by normalising \vec{R}_{3D} to the number of sources via $\vec{d}_{3D} = \frac{3}{N} \vec{R}_{3D}$ and the dipole amplitude is estimated via $|\vec{d}_{3D}|$. Already in Rubart and Schwarz (2013) a correction of the dipole amplitude and corresponding biases have been discussed in great detail. Beside the known directional bias (Rubart and Schwarz, 2013; Singal, 2019), which is introduced by masking, a general directional bias is found and described in Siewert et al. (2020b). In order to summarize on the linear estimator, we find that the linear estimator is of limited use to estimate the dipole direction.

Therefore, we introduce and test a quadratic estimator (Bengaly et al., 2019; Siewert et al., 2020b):

$$\chi^2 = \sum_i^{N_{\text{cell}}} \frac{(N_{i,o} - N_{i,m})^2}{N_{i,m}}, \quad (2.2)$$

which compares the observed source counts per cell $N_{i,o}$ to the model source counts:

$$N_{i,m} = m(1 + \vec{d} \cdot \vec{e}_i). \quad (2.3)$$

The model modifies the homogenous source distribution at position \vec{e}_i , here the monopole source counts per cell m , with a dipole \vec{d} pointing towards the direction \hat{d} with amplitude d . The dipole amplitude itself is expressed in Equation (1.68). In order to find the best-fit dipole, the χ^2 is minimised on the discretised parameter space of possible dipole directions, dipole amplitudes and monopole amplitudes.

For simulated skies with 10^7 sources, boosted with a kinematic dipole of order of the CMB dipole (see Sect. 1.5.4), we can recover the dipole amplitude within absolute accuracy of 10^{-3} and the dipole direction within one degree. The averaged dipole amplitude for 100 simulated skies was found to be $d = (0.46 \pm 0.06) \times 10^{-2}$ (Siewert et al., 2020b) with a dipole direction of $(RA, DEC) = (167.39, -6.40)$ deg. The angular offset $\Delta\theta_{\text{CMB}} = 0.77$ deg of the averaged dipole direction to the CMB dipole direction is within $q_{68} = 1.11$ deg of the estimated semi-vertical angle of the 68% confidence cone. Masking the simulated skies of 10^7 sources with a basic mask, which excludes galactic latitudes of $|b| < 10$ deg, we find a dipole amplitude of $d = (0.47 \pm 0.06) \times 10^{-2}$ and dipole direction of

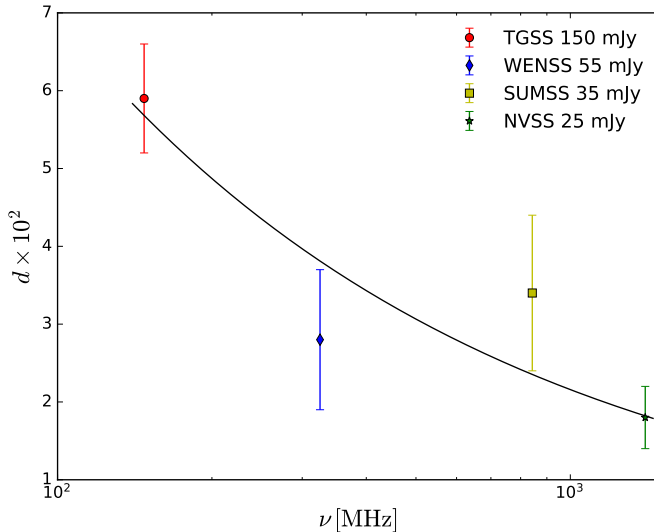


Figure 2.1: Estimated dipole amplitudes for the TGSS-ADR1, WENSS, SUMSS, and NVSS radio source catalogues with flux density thresholds of 150, 55, 35, and 25 mJy respectively (Siewert et al., 2020b).

$(RA, DEC) = (167.31, -5.91)$ deg (Siewert et al., 2020b). This resulting dipole direction is within $\Delta\theta_{\text{CMB}} = 1.21$ deg to the CMB dipole and is in good agreement to previous results (Bengaly et al., 2019). Varying the galactic latitude cut and also masking randomly chosen regions of the sky does not result in a significant change of the recovered dipole direction and amplitude.

We conclude that the quadratic estimator is unbiased by masking procedures and a simulated Cosmic Radio Dipole can be recovered for a full sky within an offset of one degree and absolute accuracies on the dipole amplitude better than 10^{-3} .

2.2 Estimates from different surveys

In Siewert et al. (2020b) we additionally estimate the Cosmic Radio Dipole for the TGSS-ADR1, WENSS, SUMSS, and NVSS radio source catalogues. We define two sets of masks, which are based on unobserved regions, the galactic plane (“mask d”), and additionally on the flux density of the local noise (“mask n”). Based on these masks, we estimate for the first time consistently the Cosmic Radio Dipole from the source counts maps of each survey and for different flux density thresholds with the help of the quadratic estimator. Between the two masking strategies we find in general self-consistency for the dipole directions and dipole amplitudes within each survey for different flux density thresholds. We observe for all four surveys an excess in the estimated dipole amplitudes with respect to the CMB dipole, while we find for the TGSS-ADR1 the highest and for the NVSS the

Table 2.1: Estimated dipole directions (RA, DEC) and dipole amplitudes (d) (Siewert et al., 2020b) for the TGSS-ADR1, WENSS, SUMSS, and NVSS source catalogues with flux density thresholds (S). The source density (n) per square degree is based on the sky coverage of “mask d”.

Survey	S [mJy]	n [deg ⁻²]	d $\times 10^{-2}$	RA [deg]	DEC [deg]	$\chi^2/\text{d.o.f.}$
TGSS	150	5.86	5.9 ± 0.7	139.53 ± 11.33	11.52 ± 10.21	1.83
WENSS	55	10.22	2.8 ± 1.0	127.51 ± 29.27	-10.71 ± 6.59	1.57
SUMSS	35	8.48	3.4 ± 1.0	$10.8.05 \pm 22.64$	-4.12 ± 8.92	1.49
NVSS	25	7.68	1.8 ± 0.4	140.02 ± 13.63	-5.14 ± 13.26	1.23

lowest dipole amplitudes. However, our results on the dipole amplitudes and directions, presented in Siewert et al. (2020b), are in good agreement with previous results from the literature (e.g. Blake and Wall 2002; Singal 2011; Singal 2019; Rubart and Schwarz 2013). The observed differences in the dipole amplitudes between the TGSS-ADR1 and NVSS is still persistent for a common subsample, which is formed by cross-matching sources of both surveys within $10''$. In order to quantify the differences in the dipole amplitudes, we fit a power law of the form $f(\nu) = A(\nu/1 \text{ GHz})^m$ to the dipole amplitudes of the TGSS-ADR1, WENSS, SUMSS, and NVSS radio source catalogues with flux density thresholds of 150, 55, 35, and 25 mJy, respectively. The estimated dipole amplitudes are shown in Figure 2.1 and together with the estimated dipole directions in Table 2.1. Based on the given sets of flux density thresholds in Siewert et al. (2020b), we have selected the thresholds in the fit such that they follow roughly the power law of Equation 1.60. The fit results, with $A = (2.16 \pm 0.53) \times 10^{-2}$ and $m = -0.51 \pm 0.15$ for a goodness-of-fit of $\chi^2/\text{d.o.f.} = 1.23$, confirms our assumption of a frequency dependent dipole amplitude.

We conclude that the estimated dipole amplitude shows for all surveys an excess with respect to the CMB dipole. Additionally, we find that the observed frequency dependency is incompatible with the assumption of a purely kinematic effect.

2.3 Publication arXiv:2010.08366

The publication

“The Cosmic Radio Dipole: Estimators and Frequency Dependence’

by

Thilo M. Siewert, Matthias Schmidt-Rubart, and Dominik J. Schwarz

was mainly produced by Thilo M. Siewert, except for the text and results in Section 3 of the publication, which have been mainly produced by Matthias Schmidt-Rubart. The publication is listed on arXiv in the category of astro-ph.CO

<https://arxiv.org/abs/2010.08366>

and it was submitted to A&A on November 3rd, 2020.

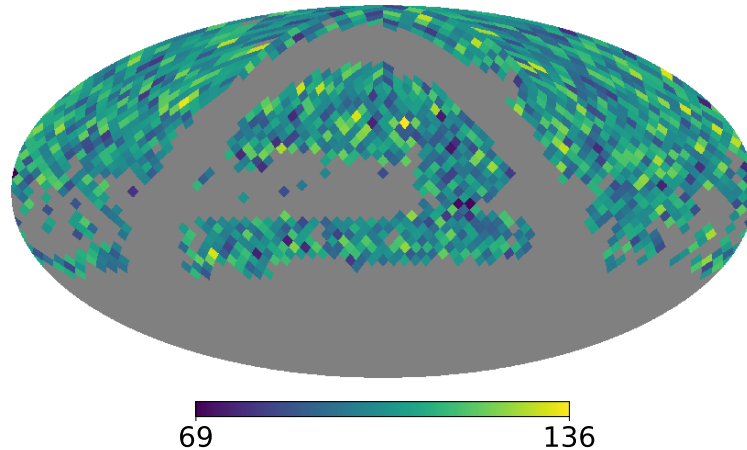


Figure 2.2: Source counts per HEALPix cell of the NVSS survey with 25 mJy flux density threshold and masked with “mask x”. The source counts are shown in equatorial coordinates and Mollweide projection with a HEALPIX resolution of $N_{side} = 16$.

2.4 Supplementary material

In the following sections, additional and consecutive materials to Siewert et al. (2020b) are shown. Based on the masking procedures introduced in Siewert et al. (2020b), a second noise mask is defined in Section 2.4.1 for the NVSS catalogue. For the cross-matched sources of the TGSS-ADR1 and NVSS source catalogues, we estimate the spectral index distribution in Section 2.4.2. Using a different, publicly available fitting routine, we test in Section 2.4.3 the general assumption of the Cosmic Radio Dipole and estimate it for the TGSS-ADR1 and NVSS source catalogues. As the TGSS-ADR1 is known for large-scale flux density offsets, we test a rescaled subsample of the survey for the Cosmic Radio Dipole in Section 2.4.4.

2.4.1 NVSS with a different noise mask

Like presented in Siewert et al. (2020b), the local rms noise can be used to define masks for the maps of the source counts per cell. In case of the NVSS catalogue, the local rms noise is not reported in the most commonly used version, published on Vizier¹. Therefore, we combine the radio source catalogue (VIII/65) available from Vizier, which does not report the rms noise, with the radio source catalogue provided directly by the NRAO on their webpage² via anonymous ftp. The other main difference of these two catalogue versions is the accuracy of the source positions, which are in the second version reported with only four digits. Additionally, the second version includes more sources, which have

¹<http://vizier.u-strasbg.fr>

²<https://www.cv.nrao.edu/nvss/>

Table 2.2: Estimated direction (RA, DEC) and amplitude d of the Cosmic Radio Dipole for the NVSS survey, masked with “mask x” and flux density threshold S . We also show the resulting number of sources N and the directional offset $\Delta\theta$ to the CMB dipole, as well as the $\chi^2/\text{d.o.f.}$ of the fit. Errors are estimated from 100 bootstraps for each sample.

S [mJy]	N	RA [deg]	DEC [deg]	$\Delta\theta$ [deg]	d ($\times 10^{-2}$)	$\chi^2/\text{d.o.f.}$
15	246 161	165.50 ± 23.86	41.00 ± 20.34	47.99 ± 18.60	1.5 ± 0.4	1.19
25	156 331	166.58 ± 22.68	43.26 ± 19.44	50.22 ± 18.51	1.7 ± 0.4	1.09
35	113 246	169.88 ± 25.21	40.56 ± 20.34	47.53 ± 19.22	1.7 ± 0.5	1.10
45	87 666	169.75 ± 26.76	36.60 ± 21.68	43.58 ± 20.07	1.7 ± 0.5	1.11
55	70 777	177.35 ± 31.21	34.74 ± 21.61	42.62 ± 20.74	1.8 ± 0.5	1.10

been removed in the common version. The cross-matching is carried out with TOPCAT (Taylor, 2005) and sources within $2''$ are matched. Doing so, we account to each source of the VizieR catalogue a local rms noise from the NRAO catalogue. We checked that no source is cross-matched twice and that all sources of the VizieR catalogue are recovered by the cross-matching. Following the masking procedure of Siewert et al. (2020b), the local rms noises are averaged per cell with a pixelisation resolution of $N_{\text{side}} = 16$. For the 68% limit of all cells, we find $\sigma_b^{68} = 0.49 \text{ mJy beam}^{-1}$. Masking all cells with $\sigma_b^{68} > 0.49 \text{ mJy beam}^{-1}$ and adding the criteria from the default mask of the NVSS (Siewert et al., 2020b), we get a fractional sky coverage of $f_{\text{sky}} = 0.49$. The combined mask is denoted “mask x” in the following. The NVSS catalogue with a 25 mJy flux density threshold and masked with “mask x” is shown in Figure 2.2. Comparing Figure 2.2 of this thesis to Figure 6 of Siewert et al. (2020b) reveals similar masked regions. Using the same quadratic estimator as in Siewert et al. (2020b) gives the results presented in Table 2.2. The results, as well as the errors, are based on estimates from 100 bootstraps of the corresponding source count maps.

While the sky coverage of “mask x” is comparable to the one of “mask n” from Siewert et al. (2020b), we find strong differences in the observed declination angles. The resulting dipole amplitudes and right ascensions on the other side are in good agreement to the previous findings. Comparing the offset of the estimated dipole directions with respect to the CMB dipole from “mask d” and “mask n” to the results of Table 2.2, we observe significantly increased values. This indicates a strong systematic feature in the NVSS catalogue, which was not covered by the previous masking procedure. The goodness-of-fit $\chi^2/\text{d.o.f.}$ reports comparable, or slightly smaller values for the “mask x” than for “mask n”.

Similar to “mask n”, the “mask x” rejects mainly cells around zero declination. The relatively clear cut of masked cells on the southern hemisphere in the centre of Figure 2.2 starts roughly at $DEC = -10 \text{ deg}$ and extends up to $DEC = 15 \text{ deg}$ on the northern hemisphere. This strip of masked cells coincidences with the Band 3 of the NVSS observations, which is the first band on the southern hemisphere observed in the “D” configuration of the VLA telescope. The configuration of the VLA telescope was

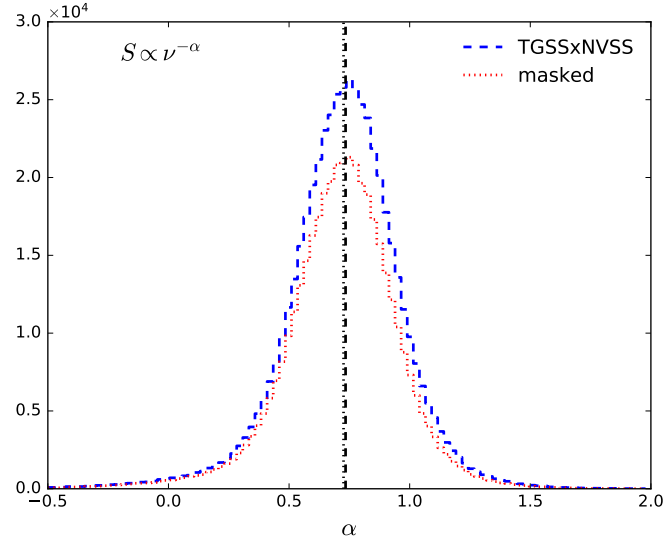


Figure 2.3: Estimated spectral index distribution of the unmasked (blue dashed) and masked (red dotted) TGSSxNVSS catalogue. The median spectral indices are $\alpha = 0.734$ and $\alpha_{masked} = 0.726$ (black vertical lines) respectively.

mainly changed in order to account for stronger system noise away from the zenith, due to ground contributions (Condon et al., 1998). Therefore, the snapshot duration was planned to maintain a constant noise level in the observations. Due to the concentrated band of rejected cells, the sky coverage of the mask indicates systematic effects in the noise levels of the NVSS. Additionally, the declination angles of the measured dipole directions in Table 2.2 coincides with band 6 of the NVSS observations, which covers mainly the zenith of the VLA telescope. Combining these two observations suggests that masking the NVSS with “mask x” biases the measurement of the Cosmic Radio Dipole to the cleanest regions of the NVSS.

2.4.2 Spectral Index from TGSSxNVSS

Using the flux densities of the cross-matched sources of the TGSSxNVSS catalogue at $\nu_{TGSS} = 147.5$ MHz and $\nu_{NVSS} = 1400$ MHz, we can estimate the spectral index distribution of the cross matched catalogue. Based on the common definition of the flux density $S \propto \nu^{-\alpha}$ the spectral index of each TGSSxNVSS source is estimated via:

$$\alpha = \frac{\log(S_{TGSS}/S_{NVSS})}{\log(\nu_{NVSS}/\nu_{TGSS})} \quad (2.4)$$

In Figure 2.3 we show the spectral index distribution of the unmasked and masked TGSSxNVSS catalogue. We estimate a median spectral index of $\alpha = 0.734 \pm 0.247$ and $\alpha_{masked} = 0.726 \pm 0.244$, respectively (mean: $\bar{\alpha} = 0.723$, $\bar{\alpha}_{masked} = 0.714$). Previous

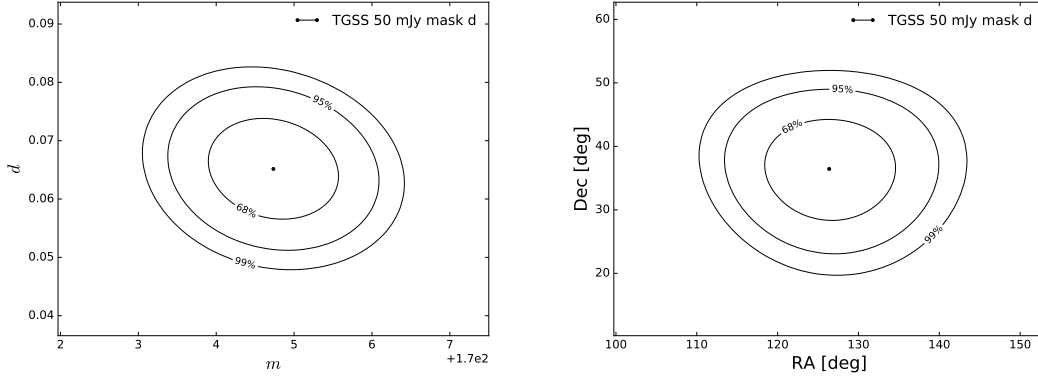


Figure 2.4: Confidence regions of the best-fit values for the monopole and dipole amplitude (*left*), and for the Right Ascension and Declination (*right*) of the TGSS-ADR1 50 mJy “mask d” sample.

reported estimates of the spectral index, like Tiwari (2016) with a mean spectral index of $\bar{\alpha} = 0.763 \pm 0.211$, matched sources within $30''$ with $S_{\text{TGSS}} \geq 100$ mJy and $S_{\text{NVSS}} \geq 20$ mJy. Additionally, de Gasperin et al. (2018) reprocessed and matched the images of the NVSS and TGSS and found an averaged spectral index of $\bar{\alpha} = 0.7870 \pm 0.0003$ with standard deviation $\sigma_{\alpha} = 0.24$. Both of these estimates are in reasonable agreement to the median spectral indices of the TGSSxNVSS catalogue. In a study of large-scale clustering of TGSS sources, Dolfi et al. (2019) also cross-matched TGSS and NVSS sources. Based on the larger searching radius of $45''$, Dolfi et al. (2019) accounted in case of more than one source only the closet NVSS source as the cross-match. From the common sub-sample of 103 047 sources they estimate a mode spectral index of $\alpha \simeq 0.77$, which is in good agreement to previous results and in reasonable agreement to our results.

2.4.3 Different fitting routine

The routine used in Siewert et al. (2020b) to minimize the χ^2 of the quadratic estimator is a simple C program, which is after some optimization still slow compared to highly optimized routines from the literature. Another way to minimize the χ^2 is to use existing fitting functions, like the python package LMFIT³ (Newville et al., 2016) and adapt the fitting routine to our question. Doing so, the residual in the model function of LMFIT is redefined as:

$$r_i = \frac{N_{i,o} - N_{i,m}}{\sqrt{N_{i,m}}}, \quad (2.5)$$

with $N_{i,o}$ the observed source counts per cell and $N_{i,m}$ the common definition of the model source counts from Equation (27) of Siewert et al. (2020b). The advantage of LMFIT is on one side the speed-up of a single fit and on the other the possibility to directly

³<http://lmfit.github.io/lmfit-py/index>

Table 2.3: Fitted dipole directions and amplitudes for the TGSS-ADR1 catalogue. The radio dipole is fitted for two different masks and four different flux density thresholds.

Mask	S (mJy)	RA (deg)	DEC (deg)	d ($\times 10^{-2}$)	$\chi^2/\text{d.o.f.}$	AIC	BIC
d	50	$126.38^{+5.39}_{-5.29}$	$36.44^{+5.33}_{-5.19}$	$6.52^{+0.57}_{-0.57}$	3.65	2844.39	2867.17
	100	$151.01^{+5.83}_{-5.67}$	$10.75^{+6.95}_{-6.89}$	$5.14^{+0.51}_{-0.50}$	2.20	1739.06	1761.84
	150	$150.58^{+5.81}_{-5.65}$	$11.86^{+6.92}_{-6.85}$	$5.76^{+0.56}_{-0.56}$	1.93	1446.99	1469.77
	200	$151.52^{+5.96}_{-5.79}$	$10.59^{+7.13}_{-7.06}$	$6.09^{+0.61}_{-0.61}$	1.74	1219.94	1242.72
n	50	$133.73^{+4.78}_{-4.63}$	$16.95^{+5.79}_{-5.67}$	$6.09^{+0.52}_{-0.52}$	2.48	1465.57	1487.09
	100	$143.71^{+5.43}_{-5.25}$	$13.23^{+6.56}_{-6.45}$	$6.29^{+0.58}_{-0.57}$	2.00	1120.80	1142.32
	150	$140.67^{+5.25}_{-5.08}$	$15.01^{+6.35}_{-6.23}$	$7.31^{+0.66}_{-0.65}$	1.79	937.22	958.75
	200	$139.67^{+5.42}_{-5.23}$	$15.05^{+6.58}_{-6.44}$	$7.67^{+0.72}_{-0.71}$	1.60	762.10	783.63

estimate the error of the best-fit values and the corresponding confidence regions, as well as the correlation between the fitted parameters. The model and the residual defined in Equation (2.5) is used in combination with the default Levenberg-Marquardt least square method. The initial values of the parameters are set to the mean source counts for the monopole amplitude, while the CMB dipole is used as first estimate for the dipole amplitude and direction. An example of the confidence regions for the best-fit values of the TGSS-ADR1 50 mJy “mask d” sample are shown in Figure 2.4. The best-fit results of the dipole direction and amplitude for the TGSS-ADR1 catalogue are presented in Table 2.3.

For the nearly full sky of the TGSS-ADR1 source catalogue, the results of the fitted Cosmic Radio Dipole in Siewert et al. (2020b) are in good agreement to the results of the LMFIT routine. The dipole directions, as well as the dipole amplitudes are consistent within error bars and the test statistic $\chi^2/\text{d.o.f.}$ reports similar values. By expanding the new fit routine to smaller surveys, like the WENSS and SUMSS catalogue, the routine is not converging correctly. For the WENSS 25 mJy sample of “mask d” the routine finds a dipole amplitude of $d = (8.15 \pm 0.56) \times 10^{-2}$ with a direction of $(RA, DEC) = (139.70 \pm 6.09, -73.42 \pm 23.43)$ deg. Especially the dipole amplitudes and the declinations are affected by the poor fit, which differ strongly from previous results of Siewert et al. (2020b) and from the literature. Increasing the flux density threshold, the fit quality becomes poorer and the routine is not able to determine sensitive uncertainties. The same behaviour is observed for the even smaller SUMSS source catalogue. A possible reason for the not converging fitting routine might be the small survey coverage, which is not sufficient to have enough statistics to estimate a percent effect like the radio dipole. The minimization routine, used in Siewert et al. (2020b), estimates the dipole amplitude and direction brute-force in a given parameter space, which is in case of small surveys a better choice. On the other hand, fixing the parameter space harbours the risk of forcing

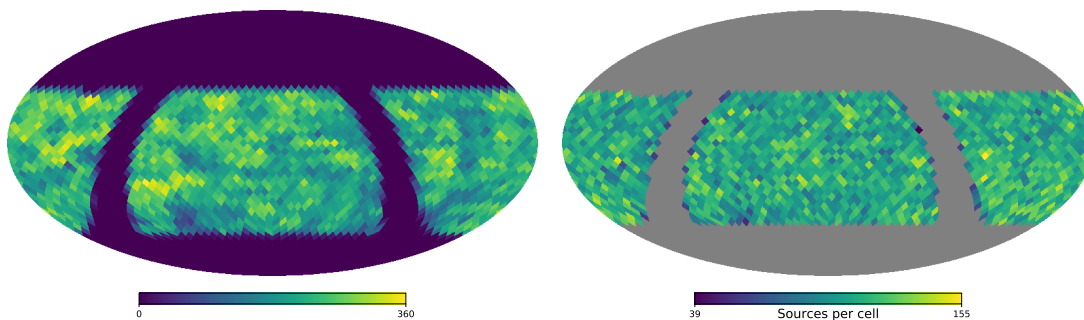


Figure 2.5: Source counts per cell of the complete TGSS-RSADR1 catalogue (*left*) and masked with “mask d” and flux density threshold of 100 mJy (*right*). The map is shown in Mollweide projection with equatorial coordinates and HEALPIX resolution $N_{\text{side}} = 16$.

the routine to match the initial hypothesis.

With the LMFIT routine, we tested the two different hypothesis of having only a monopole and a monopole with dipole amplification. First, we fitted only a monopole amplitude to the observed source counts per cell of the NVSS catalogue, which is varied around the mean as initial value. Secondly, we redo the fitting with the additional dipole modification, while the monopole amplitude is fitted in the same manner as before. The results of this test are shown in Table 2.4. Based on the Akaike (AIC) and Bayesian Information Criterion (BIC), most of the estimated dipoles for “mask d” agree much better with the data than with a pure monopole. Interestingly, while fitting only the monopole amplitude, the estimated monopole of the “mask d” samples matches perfectly with the sample mean. Fitting additionally the dipole modification changes the monopole amplitude towards a lower number of sources per cell. As the dipole modification varies with a cosine around the monopole, it is not a priori clear that the monopole amplitude should change to a smaller number of sources. Redoing the same procedure for the “mask n” samples, we find results similar to results of the “mask d” samples, except for the 35 and 45 mJy flux density thresholds.

Based on the test presented in this section, we conclude that it is acceptable to directly fit the dipole modification in Siewert et al. (2020b).

2.4.4 Rescaled TGSS-ADR1 catalogue

As mentioned previously in Section 1.4 and in Siewert et al. (2020b), the flux density scale of the TGSS-ADR1 (Intema et al., 2017) source catalogue shows large-scale offsets in the flux density calibration. Hurley-Walker (2017) made an effort to rescale the TGSS-ADR1 flux density scale using flux densities from the GLEAM (Hurley-Walker et al., 2017) survey. In the overlapping region of both surveys, they searched for a representative sample of both catalogues by applying numerous criteria. The resulting selection of sources are cross-matched within $25''$, forming a sub-sample of 23 796 sources. From this sub-sample, they interfered the spatial distribution of the logarithmic flux density ratio

Table 2.4: Fitted monopole amplitudes, dipole directions and dipole amplitudes for the NVSS catalogue. The radio dipole and monopole are fitted for two different masks and five different flux density thresholds.

Mask	S [mJy]	RA [deg]	DEC [deg]	d_{est} ($\times 10^{-2}$)	\bar{N}	m_{est}	χ^2/dof	AIC	BIC
d	15	-	-	-	162.64	162.64	1.29	520.11	525.72
		141.13 ^{+12.60} _{-11.97}	-3.17 ^{+16.47} _{-17.07}	1.51 ^{+0.33} _{-0.33}	161.35 ^{+0.35} _{-0.35}	161.35 ^{+0.35} _{-0.35}	1.27	488.91	511.35
	25	-	-	-	103.58	102.37	1.22	401.74	407.35
		148.62 ^{+13.01} _{-12.34}	-8.94 ^{+16.16} _{-17.27}	1.83 ^{+0.41} _{-0.40}	102.40 ^{+0.27} _{-0.27}	102.40 ^{+0.27} _{-0.27}	1.21	386.40	408.84
	35	-	-	-	75.17	75.17	1.24	440.79	446.40
	145.43 ^{+16.74} _{-15.65}	-24.34 ^{+17.65} _{-20.42}	1.83 ^{+0.52} _{-0.51}	74.05 ^{+0.23} _{-0.23}	74.05 ^{+0.23} _{-0.23}	1.22	399.90	422.34	
	45	-	-	-	58.28	58.28	1.25	453.68	459.29
		149.17 ^{+17.60} _{-16.42}	-38.53 ^{+14.65} _{-17.38}	2.33 ^{+0.64} _{-0.62}	57.22 ^{+0.21} _{-0.21}	57.22 ^{+0.21} _{-0.21}	1.22	401.68	424.12
	55	-	-	-	47.14	45.93	1.22	394.67	400.28
		167.83 ^{+19.98} _{-18.92}	-43.53 ^{+14.22} _{-17.35}	2.52 ^{+0.73} _{-0.70}	46.07 ^{+0.18} _{-0.18}	46.07 ^{+0.18} _{-0.18}	1.21	386.60	409.04
n	15	-	-	-	161.95	161.95	1.22	303.11	308.43
		161.94 ^{+22.29} _{-21.23}	43.34 ^{+20.91} _{-17.28}	1.44 ^{+0.43} _{-0.41}	160.18 ^{+0.44} _{-0.44}	160.18 ^{+0.44} _{-0.44}	1.20	284.48	305.79
	25	-	-	-	102.85	102.85	1.13	189.28	194.61
		164.76 ^{+21.15} _{-20.31}	42.33 ^{+20.25} _{-16.85}	1.79 ^{+0.52} _{-0.50}	101.29 ^{+0.34} _{-0.34}	101.29 ^{+0.34} _{-0.34}	1.11	164.30	185.60
	35	-	-	-	74.50	73.37	1.14	194.75	200.08
	168.82 ^{+28.46} _{-27.26}	40.51 ^{+28.68} _{-22.60}	1.56 ^{+0.61} _{-0.58}	73.10 ^{+0.29} _{-0.29}	73.10 ^{+0.29} _{-0.29}	1.13	192.86	214.17	
	45	-	-	-	57.68	56.55	1.13	187.52	192.85
		174.34 ^{+29.15} _{-28.32}	20.48 ^{+35.64} _{-31.57}	1.40 ^{+0.61} _{-0.60}	56.42 ^{+0.26} _{-0.26}	56.42 ^{+0.26} _{-0.26}	1.13	187.79	209.10
	55	-	-	-	46.56	46.56	1.16	222.72	228.05
		201.95 ^{+23.28} _{-24.31}	12.75 ^{+30.33} _{-29.03}	1.79 ^{+0.66} _{-0.65}	45.33 ^{+0.23} _{-0.23}	45.33 ^{+0.23} _{-0.23}	1.13	183.86	205.16

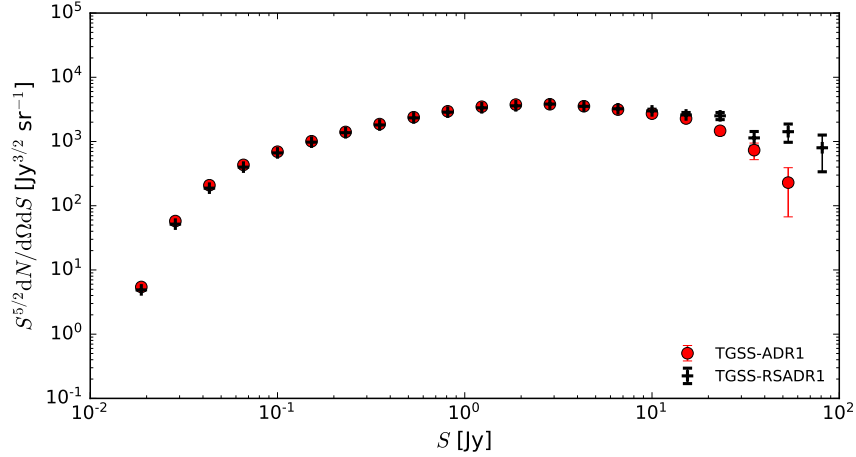


Figure 2.6: Normalised differential source counts of the masked TGSS-ADR1 (red dot) and TGSS-RSADR1 (black cross).

of both surveys. In order to get the flux density ratio for the complete field of view, a interpolation between radial basis functions of the form $\phi(r) = r$, which are centred at each source position and smoothed over angular scales of 10 deg, is used. From this fit, they inferred a correction factor, based on the fitted radial basis function at the position of each TGSS-ADR1 source in the overlap and multiplied it to the flux density of the individual source. The resulting rescaled catalogue, TGSS-RSADR1, with 383 589 sources is shown as source count map in Figure 2.5. Similar to Siewert et al. (2020b), we produced a default mask (mask d), which masks unobserved regions and the Galactic plane within $|b| \leq 10$ deg. The masked TGSS-RSADR1 with a flux density threshold of 100 mJy is shown in the right panel of Figure 2.5.

In order to compare the rescaled flux densities of the TGSS-RSADR1 to the sources of TGSS-ADR1, the differential source counts are shown in Figure 2.6. For flux densities below the point source completeness limit of 100 mJy the differential source counts of the rescaled catalogue show lesser counts than for the TGSS-ADR1 catalogue. The source counts at higher flux densities differ more strongly between the two surveys than for small flux densities, which is probably caused by the different sky coverage and therefore poorer statistics of bright sources in the TGSS-RSADR1. On an intermediate flux density range, the source counts seem not to be significantly affected. In general, the differential source counts do not change significantly by rescaling the flux density scale of the TGSS-ADR1.

Therefore, we investigate if the unscaled flux densities of the TGSS-ADR1 and the large-scale offsets contribute to the enlarged amplitude of the observed Cosmic Radio Dipole. We do so by applying the same set of flux density thresholds to the TGSS-RSADR1 and estimate the Cosmic Radio Dipole for these samples. The results of this test are shown in Table 2.5.

Table 2.5: Estimated dipole directions (RA, DEC) and amplitudes d for the TGSS-RSADR1 catalogue, masked with three different masks and flux density thresholds S . Errors are estimated from 100 bootstraps for each sample.

Mask	f_{sky}	S (mJy)	N	RA (deg)	DEC (deg)	d ($\times 10^{-2}$)	$\chi^2/\text{d.o.f.}$
d	0.52	50	277 024	124.15 ± 26.85	64.75 ± 11.34	3.3 ± 0.8	3.10
		100	172 063	240.73 ± 12.96	-54.87 ± 11.24	3.9 ± 0.8	1.78
		150	121 897	232.47 ± 14.15	-57.73 ± 8.40	4.8 ± 0.9	1.38
		200	93 365	240.60 ± 11.33	-62.35 ± 6.74	6.3 ± 1.0	1.10
15	0.47	50	256 250	137.67 ± 23.26	66.13 ± 11.28	3.4 ± 0.7	2.61
		100	158 825	235.64 ± 13.42	-45.15 ± 12.32	3.4 ± 0.6	1.51
		150	112 433	235.51 ± 13.00	-53.60 ± 9.58	4.3 ± 0.9	1.37
		200	86 091	239.22 ± 12.17	-58.55 ± 7.69	5.8 ± 0.9	1.25
n	0.36	50	200 816	214.48 ± 21.07	-6.53 ± 30.02	1.8 ± 0.5	2.21
		100	121 066	241.19 ± 10.92	-55.94 ± 8.29	5.4 ± 1.0	1.71
		150	85 190	240.37 ± 13.64	-57.21 ± 9.44	5.6 ± 1.0	1.53
		200	64 988	244.74 ± 11.68	-63.07 ± 6.64	6.7 ± 1.2	1.36

We find for the default mask a strong difference of the dipole directions and dipole amplitudes with respect to the results of Siewert et al. (2020b). Between the 100, 150, and 200 mJy results of Table 2.5, the dipole directions are in good agreement. The dipole amplitude on the other hand increases significantly with increasing flux threshold. As the TGSS-RSADR1 does not cover the Galactic plane within galactic latitudes of $|b| \leq 10$ deg, we reject cells which cell centre are within this limit. However, cells with centres not covered by this limit can still overlap with the Galactic plane, which will result in under-sampled cells. In order to account for this and verify the results of “mask d”, we increase the Galactic plane limit to $|b| = 15$ deg. The results of this new mask are denoted as “mask 15” in Table 2.5. We find consistent results for the dipole directions and amplitudes between “mask d” and “mask 15”. The inconsistent dipole direction and amplitude for the 50 mJy sample with respect to the other flux density thresholds still persists and it has additionally the lowest fit quality. This inconsistency is probably caused by the incompleteness of the TGSS-ADR1 and therefore also of the TGSS-RSADR1 catalogue.

We additionally redo the procedure of Siewert et al. (2020b) in order to produce a mask defined by the local rms noise of the sources, which have been equally scaled. By averaging the local rms noise of all sources per cell, we find for the 68% limit $\sigma_b^{68} = 4.05$ mJy beam $^{-1}$, which is similar to the limit found for the TGSS-ADR1 (Siewert et al., 2020b). The resulting mask recovers 1105 cells, which is in good agreement to 1110 recovered cells from a combination of the noise mask of Siewert et al. (2020b) with the “mask d” of this section. The estimated dipole directions for this “mask n” are consistent with the results of “mask d” and “mask 15” (see Table 2.5). Contrariwise, the estimated

Table 2.6: Differences between the observed dipole directions of the TGSS-RSADR1 and ADR1 in equatorial coordinates.

Mask	S (mJy)	RA (deg)	DEC (deg)
d	100	289.06	-41.30
	150	291.51	-43.26
	200	298.37	-43.46
n	100	291.02	-41.26
	150	292.16	-42.43
	200	297.01	-44.84

dipole amplitudes show for the three highest flux density thresholds larger values for “mask n” than for the corresponding samples of the previous two masks. The dipole amplitudes of “mask n” are also in better agreement to results from the TGSS-ADR1 (Siewert et al., 2020b). Over all, the $\chi^2/\text{d.o.f.}$ of the dipole measurements for the TGSS-RSADR1 report a better fit than for the TGSS-ADR1.

Based on the consistency of the estimated dipole directions for the three masks, the results indicate a significant difference between the TGSS-ADR1 and the TGSS-RSADR1 dipole. We calculate the differences of the TGSS-ADR1 and TGSS-RSADR1 dipoles to estimate the change in direction. Ignoring the 50 mJy samples due to incompleteness issues, we subtract the normalized Euclidean vectors for the three other flux density thresholds of “mask d” and “mask n”. The resulting directional changes are shown in Table 2.6, which have been converted back into equatorial coordinates. We observe a nearly consistent directional difference for all flux thresholds and masks. The origin of this directional difference is not understood yet.

As the dipole directions of the TGSS-RSADR1 are consistent for all masks and the three highest flux density thresholds, the significant directional difference is unlikely due to shot noise contributions in the smaller sub-sample of the catalogue. The resulting dipole directions are not consistent with recent measurements of the local bulk flow, like $(RA, DEC) \approx (10.8, -46.8)$ deg (Hoffman et al., 2015) estimated from the COMPOSITE dataset at radii of $R = 100 h^{-1}\text{Mpc}$ and $(RA, DEC) \approx (10.5, -51.2)$ deg (Feldman et al., 2010) estimated from combined peculiar velocity surveys at $R = 50 h^{-1}\text{Mpc}$.

Additionally, we cross-check the results by applying the same suite of masks of the TGSS-RSADR1 to the TGSS-ADR1 and estimate the Cosmic Radio Dipole with the quadratic estimator. The results of this test are shown in Table 2.7. We observe within the three samples of the TGSS-ADR1 consistent dipole directions and dipole amplitudes, which differ from the results of the TGSS-RSADR1. On the other side, the estimated dipole directions of Table 2.7 are in good agreement to previous results of the TGSS-ADR1 (Siewert et al., 2020b). However, we find a slightly decreased dipole amplitude with respect to results of Siewert et al. (2020b). If a general contribution from the masking procedure would cause the strong differences in the observed dipole directions

Table 2.7: Estimated dipole directions (RA, DEC) and amplitudes (d) for TGSS-ADR1 with 100 mJy flux density threshold, masked with three different masks of the TGSS-RSADR1. Errors are estimated from 100 bootstraps for each sample.

Mask	f_{sky}	S (mJy)	N	RA (deg)	DEC (deg)	d ($\times 10^{-2}$)	$\chi^2/\text{d.o.f.}$
d	0.52	100	176 257	154.85 ± 8.39	-15.83 ± 11.05	4.4 ± 0.5	2.13
15	0.47	100	161 080	154.13 ± 11.63	-18.67 ± 12.32	4.6 ± 0.6	2.10
n	0.36	100	123 684	154.85 ± 8.39	-15.83 ± 11.05	4.4 ± 0.5	1.96

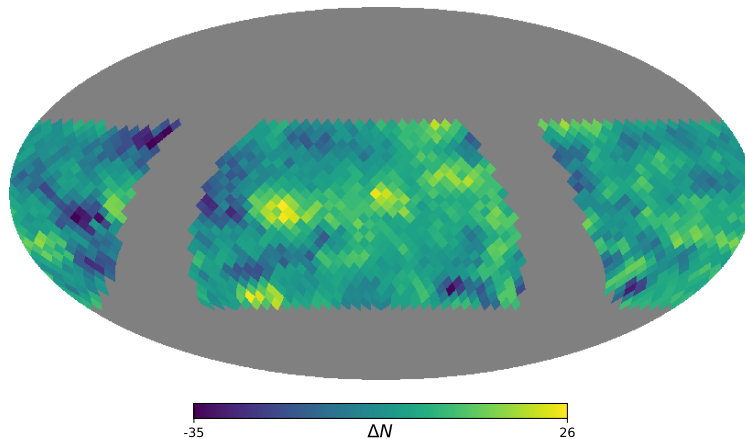


Figure 2.7: Difference map ΔN of the TGSS-RSADR1 and TGSS-ADR1 source count maps for a flux density threshold of 100 mJy and “mask 15”.

of the TGSS-RSADR1, it should also be observable with the TGSS-ADR1. On the other side, the smaller sky coverage of the TGSS-RSADR1 masks could highlight areas with systematic contributions to the dipole. In general the quadratic estimator is expected to be unbiased by the masking Siewert et al. (2020b). Therefore and based on the results of Table 2.7, we conclude that the smaller sky coverage of the TGSS-RSADR1 does not cause the strong differences in the estimated dipole directions.

In order to validate the previous results, we calculate the difference map $\Delta N = N_{\text{RS}} - N_{\text{A}}$ between the TGSS-RSADR1 (N_{RS}) and TGSS-ADR1 (N_{A}) source count maps. The difference map for a flux density threshold of 100 mJy and masked with “mask 15” is shown in Figure 2.7. We observe strong differences in the source counts per cell, which is also consistent for “mask n”. The patches of high and low differences have a similar size and shape like the radial basis functions of the rescaling process, which correspond to different observing nights of the TGSS (Hurley-Walker, 2017). These position-dependent flux density scale modification lead to position-dependent differences in the source counts, which will then introduce systematic affects to the estimated dipole direction.

Chapter 3

Forecasting possible Radio Dipole measurements

In the previous Section 2 and in Siewert et al. (2020b), the quadratic estimator was introduced and used to measure the Cosmic Radio Dipole. Using this quadratic estimator to measure the Cosmic Radio Dipole from four different surveys revealed a significantly increased dipole amplitude with respect to the CMB dipole. Several aspects and contributions to the dipole amplitude, like local structures have been briefly discussed in Siewert et al. (2020b). As stated in Siewert et al. (2020b), contributions from local structures could be identified with an increased sensitivity of upcoming surveys, like for example the SKA. Therefore, the quadratic estimator is used in the following sections and publications to estimate the Cosmic Radio Dipole from simulated number count maps with SKA specifications.

The aim of the first publication (Bengaly et al., 2019) is to estimate, how a possible survey with the SKA is sensitive to the Cosmic Radio Dipole and contributions from local large-scale structures. Therefore, number count maps for the SKA survey specifications of Phase 1 and 2 are simulated in Section 2.2 of Bengaly et al. (2019). The number count maps include shot noise, large-scale structures and a kinematic dipole with the velocity of the CMB dipole. For the flux density threshold of the survey, optimistic as well as realistic values are tested. Based on these number count maps, the Cosmic Radio Dipole is recovered in Section 3 of Bengaly et al. (2019) with the help of the quadratic estimator. Similar to the analysis in Siewert et al. (2020b), the publication briefly investigates the procedure on how to apply the dipole modification to the number count maps in Appendix A of Bengaly et al. (2019). The results of the quadratic estimator are compared in Appendix B to results from a second estimator from the literature (Bengaly et al., 2018).

The procedure and forecasts presented in Bengaly et al. (2019) have also been used for a contribution to the Red Book on the performance forecast of the Square Kilometre Array (Square Kilometre Array Cosmology Science Working Group et al., 2020), which extended the investigated range of flux density thresholds with $S > 22.8 \mu\text{Jy}$. These results have been additionally published in a third publication (Schwarz et al., 2018).

3.1 Forecast of the structure dipole

The publications Bengaly et al. (2019) and Square Kilometre Array Cosmology Science Working Group et al. (2020), which are presented in the following, use mock catalogues of radio sources to estimate the affects of large-scale structures to the observed Cosmic Radio Dipole. Therefore the basic concepts of this procedure are briefly summarised in this section.

The simulated maps are generated by computing the theoretical angular power spectrum using CAMB SOURCES (Challinor and Lewis, 2011) with the Λ CDM model and best-fit cosmological parameters of Planck Collaboration et al. (2016). The theoretical angular power spectrum is then used with the lognormal code FLASK (Xavier et al., 2016) in order to produce source count maps, which are based on the pixelisation scheme of HEALPIX (Górski et al., 2005). The necessary redshift distribution, clustering bias and magnification bias for CAMB SOURCES are used from the SKA Simulated Skies (S³; Wilman et al. 2008) and Alonso et al., 2015.

Based on these mock catalogues, which include large-scale structures, the kinematic dipole is directly modulated to the source counts maps. The dipole modulation used in the simulations follows the general dipole description of Section 1.5.4 and the dipole modulated source counts are derived from the model source counts of Equation (2.3) with the dipole amplitude of Equation (1.68). For the dipole velocity, we used the CMB dipole velocity of Planck Collaboration et al. (2018a) with $v = 369.82 \pm 0.11 \text{ km s}^{-1}$. This procedure modifies directly the source counts per cell of the HEALPIX maps. However, the simulated sources could also directly be boosted with the dipole velocity, which applies to the flux density (see Eq. 1.61) and the position of the sources (see Eq. 1.64), like described in Section 1.5.4. We tested both methods in Bengaly et al. (2019) (e.g., see App. A), as well as in Siewert et al. (2020b) (e.g., see Sect. 4.1) and found no significant differences in the resulting source count maps and the recovered dipoles. Nevertheless, boosting directly the source counts per cell improves the computation time significantly and we choose this method for all simulations of the Cosmic Radio Dipole.

3.2 Forecast in terms of the Square Kilometre Array

In Bengaly et al. (2019) and Square Kilometre Array Cosmology Science Working Group et al. (2020) several different estimates of the Cosmic Radio Dipole for simulated number count maps have been provided. These number count maps vary in the flux density threshold of the assumed survey specification, ranging from $1 \mu\text{Jy}$ of the SKA2 to $22.8 \mu\text{Jy}$ of the SKA1 survey. While the 20 and $22.8 \mu\text{Jy}$ flux density thresholds correspond to the most realistic case of the SKA1 survey, the $5 \mu\text{Jy}$ limit corresponds to the realistic case of the SKA2 survey. Additionally, the number count maps from Bengaly et al. (2019) include all effects from large-scale structure, which have not been included in the Red Book. For simplicity, the measurements of Bengaly et al. (2019) and the Red Book are summarised in Table 3.1. The reported estimates are given as mean and standard deviation from 500 simulated maps in case of Bengaly et al. (2018) and 100 maps in case

3.2. FORECAST IN TERMS OF THE SQUARE KILOMETRE ARRAY

Table 3.1: Estimates of the Cosmic Radio Dipole for different specifications of simulated number count maps. The dipole directions are given in galactic coordinates (l, b) .

Sample	N_{tot} ($\times 10^9$)	S (μJy)	l (deg)	b (deg)	d ($\times 10^{-3}$)	Reference
Full	2.37	1.0	264.87 ± 6.47	47.42 ± 4.33	4.64 ± 0.33	B19
$z \geq 0.5$	2.07	1.0	264.64 ± 5.57	47.37 ± 3.67	4.64 ± 0.30	B19
Full	0.72	5.0	265.15 ± 8.43	47.29 ± 5.58	4.67 ± 0.44	B19
$z \geq 0.5$	0.62	5.0	264.84 ± 5.77	47.43 ± 3.85	4.64 ± 0.30	B19
Full	0.33	10.0	264.50 ± 12.71	47.08 ± 6.18	4.66 ± 0.55	B19
$z \geq 0.5$	0.29	10.0	264.56 ± 7.34	47.20 ± 3.97	4.62 ± 0.38	B19
Full	0.18	20.0	263.86 ± 25.08	45.50 ± 12.89	4.93 ± 1.03	B19
$z \geq 0.5$	0.15	20.0	265.49 ± 8.65	46.83 ± 4.64	4.65 ± 0.45	B19
Full		22.8	263.5 ± 28.0	38.8 ± 19.7	5.6 ± 1.7	RB20
$z \geq 0.5$		22.8	265.3 ± 4.9	46.4 ± 4.3	4.7 ± 0.4	RB20
fiducial			264.02	48.25	4.62	P18

B19: Bengaly et al. (2019); RB20: Square Kilometre Array Cosmology Science Working Group et al. (2020); P18: Planck Collaboration et al. (2018a)

of the Red Book. All of these estimates recover the fiducial dipole, assumed to be of the order of 4.62×10^{-3} pointing in galactic coordinates towards $(l, b) = (264.02, 48.25)$ deg (Planck Collaboration et al., 2018a), within error bars. Excluding local structures with redshifts $z < 0.5$ improves the measurements significantly. We conclude that with the quadratic estimator and the SKA1 survey it will be possible to distinguish contributions from local structure and measure the Cosmic Radio Dipole with 10% accuracy on the dipole amplitude.

3.3 Publication MNRAS 486, pp. 1350-1357 (2019)

The following publication (Bengaly et al., 2019)

“Testing the standard model of cosmology with the SKA: the cosmic radio dipole”

by

Carlos A. P. Bengaly, Thilo M. Siewert, Dominik J. Schwarz, and Roy Maartens

was mainly produced by Carlos A. P. Bengaly and Thilo M. Siewert. The text was edited by Roy Maartens and Dominik J. Schwarz, while the Sections 2.4, 3, and Appendix A were mainly written by Thilo M. Siewert.

<https://doi.org/10.1093/mnras/stz832>

3.4 Publication PASA 37, e007 (2020)

The Section 3.4 of the following publication (Red Book; Square Kilometre Array Cosmology Science Working Group et al. 2020)

“Cosmology with Phase 1 of the Square Kilometre Array Red Book 2018:
Technical specifications and performance forecasts”

by

Square Kilometre Array Cosmology Science Working Group

was written by Carlos A. P. Bengaly, Roy Maartens, Dominik J. Schwarz and Thilo M. Siewert (alphabetical order). The estimates presented in Section 3.4.2 of the Red Book have been mainly produced by Thilo M. Siewert, while the simulations have been produced by Carlos A. P. Bengaly. In order to highlight the necessary parts of the Red Book and contributions of Thilo M. Siewert, the publication has been shortened for this thesis. Only the Abstract, Introduction, Section 3.4, Conclusion, and the Acknowledgements with the References are shown.

<https://doi.org/10.1017/pasa.2019.51>

3.5 Publication arXiv:1810.06373

The results of the Cosmic Radio Dipole section of the previous publication have been additionally published in a proceeding letter (Schwarz et al., 2018) to the General Assembly of the International Astronomical Union. The text of this publication (Schwarz et al., 2018)

“SKA and the Cosmic Radio Dipole”

by

Dominik J. Schwarz, Carlos A. P. Bengaly, Roy Maartens, and Thilo M. Siewert

was mainly written by Dominik J. Schwarz, while the results have been mainly produced by Carlos A. P. Bengaly and Thilo M. Siewert.

<https://arxiv.org/abs/1810.06373>

The letter is submitted and expected to appear in the supplementary material of the Proceedings of the IAU, eventually available under:

<https://doi.org/10.1017/S1743921319003442>

Chapter 4

One- and two-point source statistics of LOFAR radio sources

The publication (Siewert et al., 2020a), which is described in the following, contains a detailed statistical analysis of the data quality of the first Lofar Two-Metre Sky Survey Data Release (LoTSS-DR1; Shimwell et al. 2019) and is extended by first cosmological measurements, like differential number counts and angular two-point correlation functions of different sub-samples.

The main idea of this publication was to generate a common, cosmological working base for upcoming data releases of the LoTSS survey, which will have a bigger sky coverage and also a higher source density, based on better understandings of the calibration and source extracting pipelines. In detail, the radio source and value added catalogue of the LoTSS-DR1 (Williams et al., 2019) are compared in this publication in terms of point source completeness and one-point statistics. For example, the spatial distribution of source counts is compared to a Poisson and a Compound Poisson distribution. Whereas the value added source catalogue is then used to determine cosmological measurements in combination with theoretical expectations from cosmological simulations. We compare the differential source counts to results of the Tiered Radio Extragalactic Continuum Simulation (T-RECS; Bonaldi et al. 2019) and SKA Design Study (SKADS; Wilman et al. 2003), and the angular two-point correlation is compared to expectations calculated with CAMB SOURCES (Challinor and Lewis, 2011) based on recent best-fit cosmological parameters from Planck Collaboration et al. (2018b). For a better understanding of the results from the TGSS-ADR1 source catalogue (Intema et al., 2017) and the algorithm used to compute the angular two-point correlation, the publication is complemented by four Appendices.

In the following, the results of Siewert et al. (2020a) on the spatial source count distribution, as well as on the angular two-point correlation function are summarised. The publication itself is shown in Section 4.4 and the results of it are extended by supplementary materials in Section 4.5.

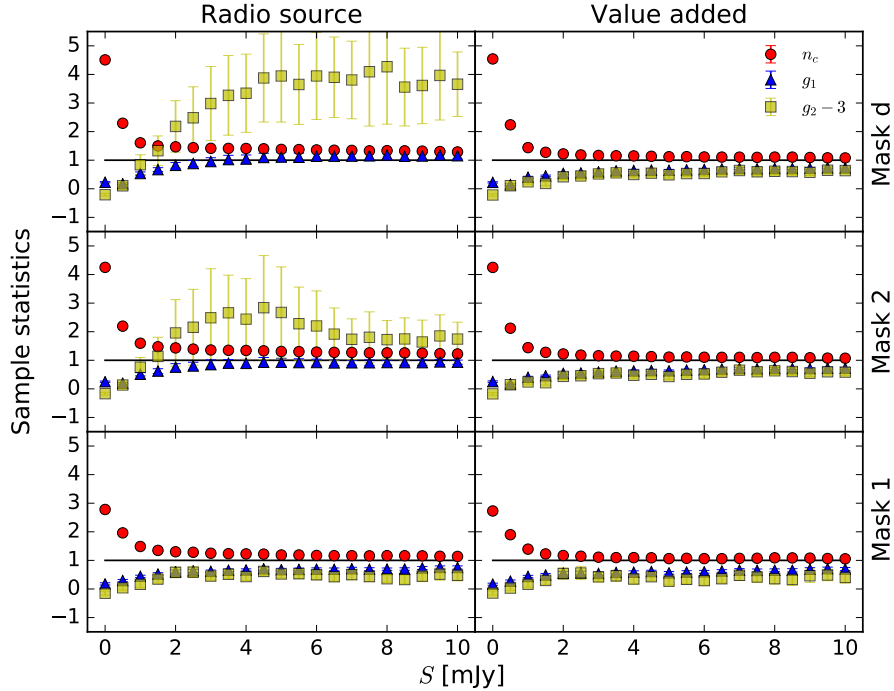


Figure 4.1: Measured clustering parameter n_c , sample skewness g_1 , and excess kurtosis $g_2 - 3$ of the LoTSS-DR1 radio source and value added source catalogue for three different masks. Figure taken from Siewert et al. (2020a).

4.1 Source count distribution of LOFAR radio sources

The first data release of the LOFAR Two-metre Sky Survey (LoTSS-DR1; Shimwell et al. 2019) covers already 424 square degrees of the northern sky. In order to test the data quality of the survey, we measured the point-source completeness of the radio source catalogue. For a region of 53 pointings out of the available 58 pointings, we find the radio source catalogue to be 99% point source complete at 0.8 mJy. The remaining five pointings are rejected, as they show clear under-densities in the source distribution. Additionally to the five rejected pointings, we define a sky coverage mask of the survey (“mask d”), which also rejects cells with less than five sources in their coverage. Based on the per cell averaged local rms noise flux densities, we define a second suite of masks, which masks cells above one (“mask 1”), two (“mask 2”), or three times (“mask 3”) the median rms noise flux density.

With this suite of masks, we measure the statistical moments of the radio source distribution as a function of flux density threshold. As already shown in Section 1.5.1, the assumption of a Poisson distribution for the spatial radio source counts does not fit to all surveys. Consequently, we calculate in Siewert et al. (2020a) the clustering

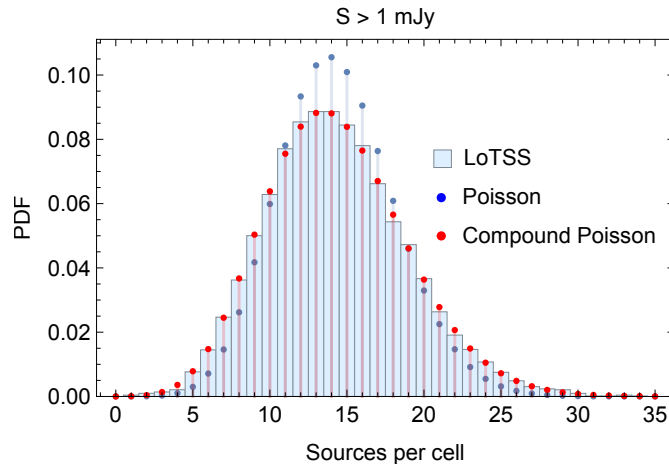


Figure 4.2: Histogram of LoTSS-DR1 source counts per cell for a flux density threshold of 1 mJy and the best-fit Poisson (blue dots) and Compound Poisson distribution (red dots). Figure taken from Siewert et al. (2020a).

parameter n_c and higher moments, like the skewness g_1 and excess kurtosis $g_2 - 3$ for both available source catalogues of the LoTSS-DR1. The first radio source catalogue consists out of the raw sources (Shimwell et al., 2019), found by the Python Blob Detection and Source Finder (PYBDSF; Mohan and Rafferty 2015). The second value added source catalogue (Williams et al., 2019) extends the analysis of the first radio source catalogue by identifying artefacts, matching multi-component sources, and finding counterparts in optical and infrared surveys. In Figure 4.1 (Siewert et al., 2020a), we show the sample statistics of the LoTSS-DR1 radio source and of the value added source catalogue. We identify a significant difference in n_c and higher moments between the radio source and the value-added source catalogue, which shows the significant improvement of identifying artefacts and matching multi-component sources.

In order to describe the distribution of the spatial source counts, we compare the observed sample skewness and excess kurtosis to the expected moments of a Poisson and Compound Poisson distribution. We observe a significant improvement by describing the sources counts with a Compound Poisson distribution, rather than with a pure Poisson distribution (e.g. see Fig. 4.2). Additionally, to further quantify the fit of both distributions to the observed source counts, we compare both with a Pearson χ^2 -test. For the 1 mJy flux density threshold sample, we find a goodness-of-fit $\chi^2/\text{d.o.f.}$ of 30.7 for the Poisson and 0.76 for the Compound Poisson distribution. From these results, we conclude that the source counts per cell do not follow a Poisson distribution and are better described by Compound Poisson distribution.

Beside the spatial source distribution, we also investigated the differential source counts as function of flux density (Siewert et al., 2020a). Deriving the differential source counts like described in Section 1.5.2, we find good agreement between the LoTSS-DR1 value added source catalogue and other measurements at roughly the same frequency

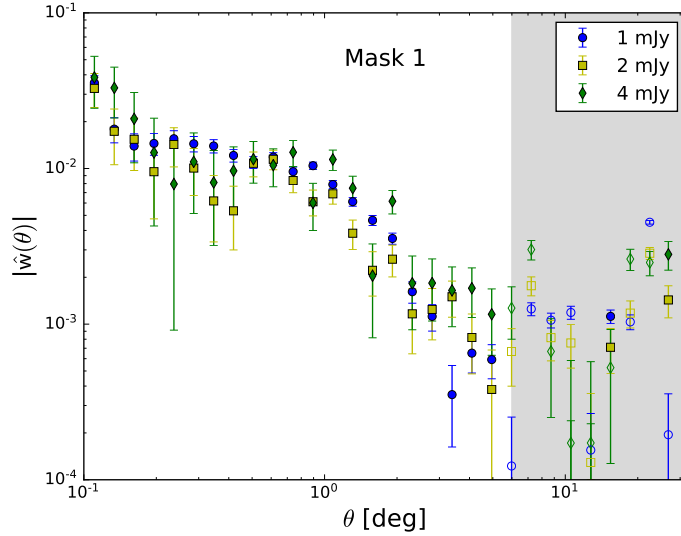


Figure 4.3: Angular two-point correlation function estimated from the LoTSS-DR1 value added source catalogue, masked with “mask 1”. Open symbols correspond to negative values of the angular two-point correlation function. Figure taken from Siewert et al. (2020a)

(Williams et al., 2016; Franzen et al., 2016). Comparing the observed differential source counts to expectations from simulations, like the SKA Design Study (SKADS; Wilman et al., 2008) and the Tiered Radio Extragalactic Continuum Simulations (T-RECS; Bonaldi et al., 2019), we find good agreement. However, both simulations show a small discrepancy in the flux density range from 3 to 12 mJy, while comparing to the observed source counts. A similar discrepancy is found in the deep-field studies of LoTSS (Mandal et al., 2020), where the T-RECS and SKADS model over-estimate the differential source counts with respect to the source counts of the Lockman Hole, the Boötes, and the Elais-N1 regions in a flux density range of 2 to 20 mJy.

4.2 Angular two-point correlation function of LOFAR radio sources

Based on the masking procedure and completeness limits defined in the previous section and Siewert et al. (2020a), we estimated the angular two-point correlation function of the LoTSS-DR1 value added source catalogue. The estimated angular two-point correlation functions of the LoTSS-DR1 value added catalogue with flux density threshold of 1,2, and 4 mJy are shown in Figure 4.3 for “mask 1”. Open symbols correspond to negative values and the grey shaded part indicates angular separations with low number of weighted pair counts, for more details see Section 4.5.1.

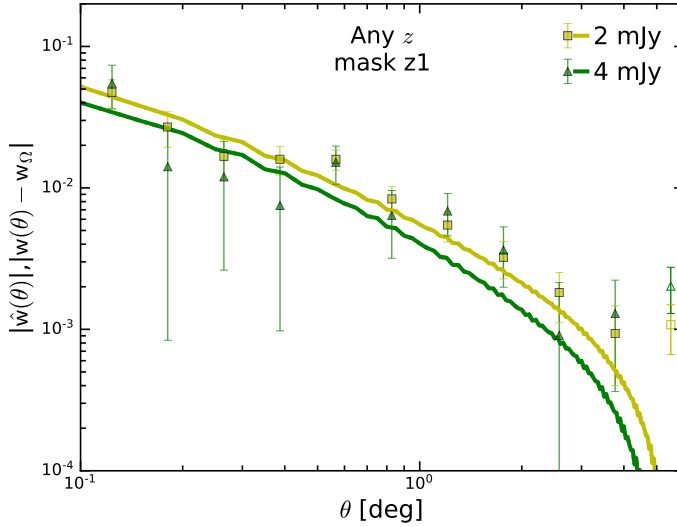


Figure 4.4: Angular two-point correlation function estimated for sources with redshift information of the LoTSS-DR1 value added source catalogue. The is masked with “mask z1”. Figure taken from Siewert et al. (2020a). Negative symbols correspond to negative values.

Previous studies of the angular two-point correlation by means of the TGSS-ADR1 source catalogue revealed a significantly increased correlation with respect to measurements from other surveys, like NVSS and FIRST. In order to compare the observed correlations with previous studies, we fitted a power law (see Eq. 4.4) to the estimated angular two-point correlations. The full set of measurements for the three flux density thresholds and different masks is presented in Siewert et al. (2020a). In comparison to the flux density dependent correlation observed for “mask d”, we find more reliable results for the low-noise region covered by “mask 1”. For the sample with 2 mJy flux density threshold and masked by “mask 1”, we find a clustering amplitude of $A = (5.1 \pm 0.6) \times 10^{-3}$ with a slope of $\gamma = 0.74 \pm 0.16$. In general, we find the radio source sky, observed with LoTSS-DR1, to be statistically isotropic at better than one percent for angular separations above one degree (Siewert et al., 2020a).

4.3 Comparison to expectations of the cosmological standard model

The big achievement of the value added source catalogue of LoTSS is, to cross-match the radio sources to optical and infrared counterparts in the Panoramic Survey Telescope and Rapid Response System (PAN-STARRS; Kaiser et al. 2002; Kaiser et al. 2010) and the Wide-field Infrared Survey Explorer (WISE; Wright et al. 2010). Based on these cross-

matches, roughly 73% of the value added sources have photometric and/or spectroscopic redshift information. We use these redshift informations to calculate expectations of the angular two-point correlation function based on the most recent Planck best-fit cosmological model Planck Collaboration et al. 2018a; Planck Collaboration et al. 2018b. Together with the galaxy bias function of Nusser and Tiwari (2015) and Tiwari and Nusser (2016) (see Eq. 4.1), we compute with the help of the CAMB SOURCE (Challinor and Lewis, 2011) code the angular power spectrum of the observed redshift distribution for redshifts $z \leq 2$. Using Equation (1.56), we then calculate the expectation of the angular two-point correlation for multipole moments up to $l = 4000$. In Figure 4.4 (Siewert et al., 2020a), the observed angular two-point correlation function (points) is compared to the expectations (lines) of non-linear theory, including the source lensing and Halofit option of CAMB. The sample is masked by a combination of “mask 1” and rejecting sources within in a band of equal declination, where counterparts of PAN-STARRS are missing. From the expectations $w(\theta)$ we subtract the integral constraint w_Ω , which is computed by means of the random-random pair counts of the observed angular two-point correlation $\hat{w}(\theta)$. We find good agreement between the observed and expected angular correlation for angular scales between 0.1 deg and 6 deg.

Additionally, we estimate the angular two-point correlation for three redshift sub-samples and compute the expectations for these redshift bins. The comparison of these results reveal problems with the galaxy bias model (Tiwari and Nusser, 2016), while piecewise constant biases improve the match of the expectations to the angular correlation of the individual redshift bins. A more sophisticated approach of directly fitting cosmological parameters and testing different bias models was beyond the scope of the work presented in Siewert et al. (2020a). More details on the calculations of the expectations and CAMB SOURCE settings, as well as on the angular two-point correlation function of different redshift sub-samples are described in Siewert et al. (2020a), as well as in the Sections 4.5.3, 4.5.4, and 4.6.

4.4 Publication A&A 643, A100 (2020)

The publication (Siewert et al., 2020a)

“One- and Two-point Source Statistics from the
LOFAR Two-metre Sky Survey First Data Release”

by

Thilo M. Siewert, Catherine Hale, Nitesh Bhardwaj, Marian Biermann, David J. Bacon,
Matt Jarvis, Huub Röttgering, Dominik J. Schwarz, Timothy Shimwell, Philip N. Best,
Kenneth J. Duncan, Martin J. Hardcastle, Jose Sabater, Cyril Tasse, Glenn J. White,
and Wendy L. Williams

was mainly written by Thilo M. Siewert, Catherine Hale, Nitesh Bhardwaj, Marian Biermann and Dominik J. Schwarz and was edited by the other authors. The Sections 3, 5, 6.2, 6.3, and App. A and D were mainly written by Thilo M. Siewert. The Sections 1, 2, 6.1, and App. C were partly written by the Thilo M. Siewert.

<https://doi.org/10.1051/0004-6361/201936592>

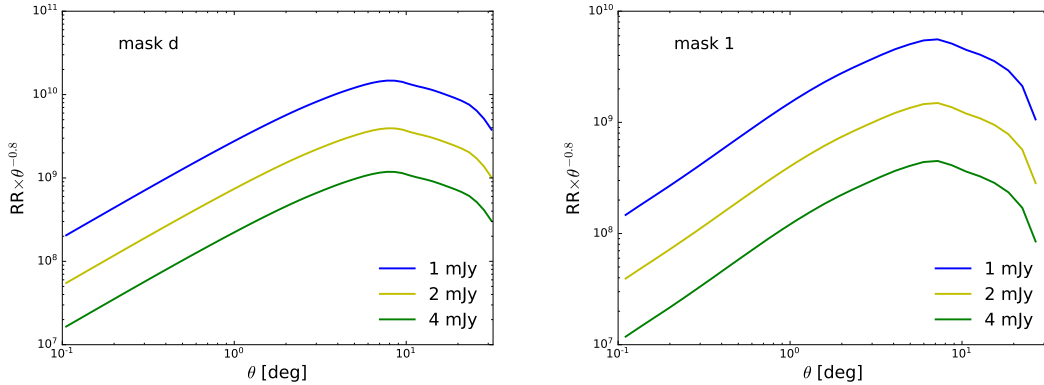


Figure 4.5: Pair counts from the mock catalogue, scaled with $\theta^{-\gamma}$ for three flux density thresholds, masked with “mask d” (*left*) and “mask 1” (*right*).

4.5 Supplementary material

In the following sections, additional results, which have been conducted in the process of preparing the publication Siewert et al. (2020a), are shown. Materials directly used from Siewert et al. (2020a) are referenced accordingly. If not stated otherwise the results shown in the following have been produced by myself.

In detail, the sensitivity of the angular two-point correlation estimator to the observed sky coverage of the LoTSS-DR1 is investigated in Section 4.5.1. Following previous problems in the procedure of how to generate the mock catalogue, the mock-mock auto-correlation has been computed in Section 4.5.2 as a sanity check to validate the new procedure. In order to compute theoretical expectations of the angular two-point correlation function, several settings and approximations of CAMB SOURCES have been tested in Section 4.5.3. In Section 4.5.4 and 4.6 the detailed analysis of the redshift dependent angular two-point correlation function is extended from Siewert et al. (2020a). Additionally, the results of the angular two-point correlation function of Siewert et al. (2020a) are compared to estimates from the literature in Section 4.7. The same procedures used to measure the angular two-point correlation function of the LoTSS-DR1 are repeated for the four surveys used in Siewert et al. (2020b), namely the TGSS-ADR1 (Intema et al., 2017), WENSS (de Bruyn et al., 2000), SUMSS (Mauch et al., 2003), and NVSS (Condon et al., 1998).

4.5.1 Sensitivity of the survey

The sensitivity of the angular two-point correlation estimator is limited by the geometry of the survey. Often this geometry is of round, or regular shape and therefore the largest possible angular scales are of order of the diameter of the survey, with typical scales of a few degrees for deep fields. On the other hand, surveys with nearly full sky coverage have also been used for the estimation of the angular two-point correlation. These surveys

have in most cases a regular and symmetric shape and are in the estimation only limited by the smaller number of sources, due to poorer sensitivity of the survey.

In the case of LoTSS-DR1, the HETDEX field yields a more complicated geometry with an unregular edge and holes in its coverage. To test up to which angular scale the estimator is sensitive, the pair counts of the mock catalogue from Siewert et al. (2020a) have been scaled with $\theta^{-\gamma}$ and $\gamma = 0.8$ for three flux density thresholds. The results of this test are shown in Figure 4.5 for “mask d” and “mask 1”. The scaled pair counts increase continuously up to 6-7 deg and start to flatten out afterwards. Comparing the pair counts at largest angular separations probed in this analysis to smaller separations they are still of the same order. For the publication Siewert et al. (2020a), we therefore concluded that results of the angular two-point correlation estimator are reasonable up to scales of order $\theta \sim 10$ deg. In case of smaller sub-samples, the scaled pair counts drop above angular separations of $\theta \sim 6$ deg much faster and therefore we shaded these regions in grey (e.g., see Fig. 4.3). The loss of scaled pair counts might also coincide with the angular two-point correlation varying around zero, which is furthermore strongly affected by the integral constraint. The angular separations above 6 deg are also affected by the inter-pointing flux density calibration, which is mainly consistent with typical angular scales of a pointing.

4.5.2 Mock - Mock correlation

In order to generate a random set of sources, necessary for the angular two-point correlation estimation, the mock catalogue, described in Section 4 of Siewert et al. (2020a) takes some survey properties, like the noise distribution into account. As the mock catalogue is therefore not purely random any more, some features and differences in the estimated angular two-point correlation could be caused by the mock catalogue itself. To investigate the affect of the mock catalogue to the estimated angular two-point correlation, a first test, where the mock catalogue is compared to a purely random set of sources, is shown in Figure 21 of Siewert et al. (2020a) (mock-random). The non-null correlation of the “mock-random” estimation is caused by the noise structure of the survey, but it is still over an order of magnitude lower than the correlation observed in the “data-mock” sample and drops strongly for larger separations. In an earlier version of this publication (arXiv:1908.10309v1), the mock catalogue was produced with a different routine, where the sources are randomly drawn for each of the pointings, which resulted in a non-vanishing “mock-random” correlation for angular separations $\theta \leq 8$ deg. Whereas in the recent version, the mock sources have been chosen over the entire field of view until roughly 20 times the total number of sources have been drawn.

The auto-correlation of the mock catalogue is checked separately, while the mock catalogue is split up randomly into two equally sized samples, which are then used as data and random sample for the estimator of the angular two-point correlation function. The resulting correlations of this test are shown in Figure 4.6 for the 1, 2 and 4 mJy flux density thresholds, masked with “mask d” (left) and “mask 1” (right). Within one sigma, all the auto-correlations of the three different flux density threshold samples for both masks are consistent with zero. As the number of sources decreases with increasing flux density

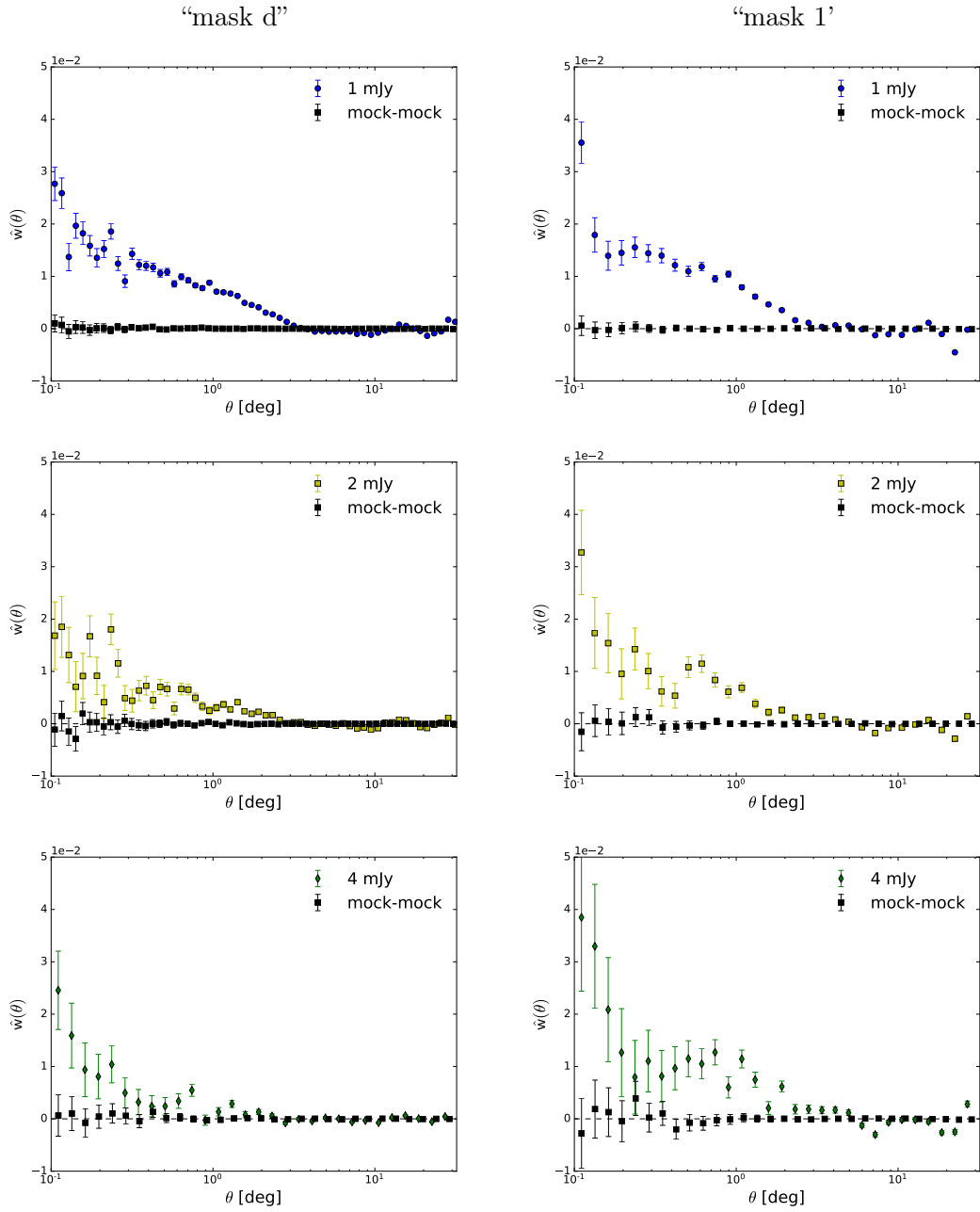


Figure 4.6: Mock - Mock correlation for “mask d” (*left*) and “mask 1” (*right*) with flux density thresholds of 1, 2, and 4 mJy (*top-bottom*). The mock catalogue was randomly splitted into two, same sized samples, which serve as data and random sample in the angular two-point correlation estimation.

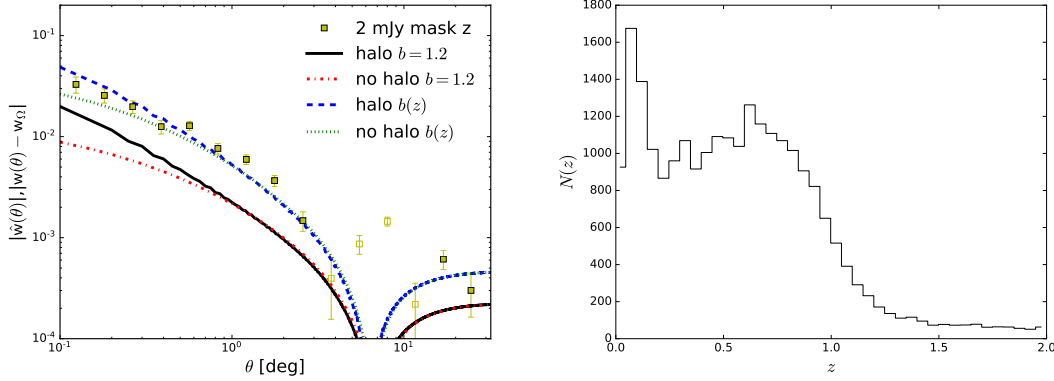


Figure 4.7: Comparison of different settings of CAMB SOURCES (lines) to the estimated angular two-point correlation function of the 2 mJy “mask z ” sample (Siewert et al., 2020a, yellow squares) from the LoTSS-DR1 value added source catalogue (*left*) and the corresponding redshift distribution (*right*).

thresholds, the error bars of both the “data-mock” and “mock-mock” correlation grow, but for most of the angular separations $\theta \leq 1$ deg the two sets are clearly distinguishable and do not show similar features. Therefore we concluded that the new procedure to generate the mock catalogue does not affect the measurement and is suitable in general for the analysis of the angular two-point correlation function.

4.5.3 Settings of CAMB SOURCES

In order to study the expectations of the angular two-point correlation function in Siewert et al. (2020a), different settings of CAMB SOURCES (Challinor and Lewis, 2011) have been tested. CAMB SOURCES allows the user to use either contributions from only linear theory, or from non-linear theory. The non-linear theory can be included by using different kinds of halo-fit models, like Smith et al. (2003) and Takahashi et al. (2012) and the current default model by Mead et al. (2016). In the following the usage of the halo-fit model is denoted as “halo” or “no halo”. Additionally, it is possible to include different models for the galaxy bias, like a piecewise constant bias or a functional form (e.g. Nusser and Tiwari, 2015), denoted as b or $b(z)$, respectively. For this analysis $b(z)$ is defined like in Siewert et al. (2020a), which was proposed by Nusser and Tiwari (2015):

$$b(z) = 1.6 + 0.85z + 0.33z^2. \quad (4.1)$$

A comparison of the theoretical expectations using halo, no halo and $b = 1.2$ (Planck Collaboration et al., 2018b), or $b(z)$ is shown in Figure 4.7 (left) for the 2 mJy “mask z ” sample of the LoTSS-DR1 value added source catalogue (Siewert et al., 2020a). All other cosmological parameters and settings necessary for the computation of the power spectrum are identically to Siewert et al. (2020a), which were taken from Planck Collaboration et al. (2018b) and are shown in Appendix A.3. The necessary redshift distribution

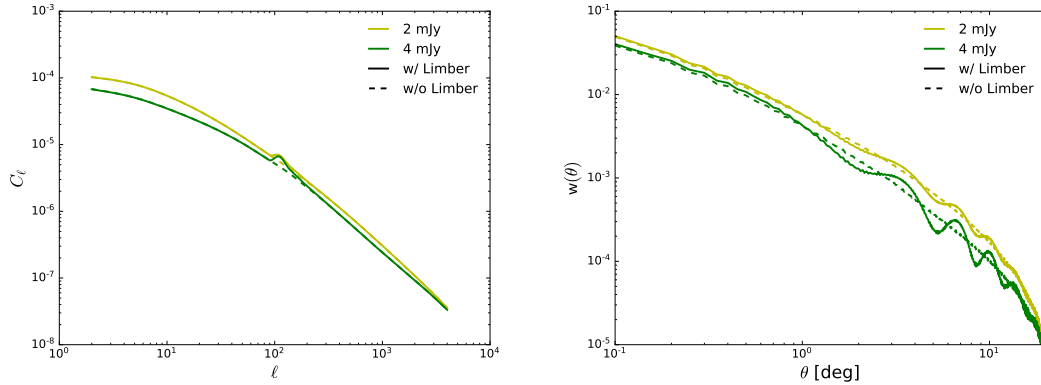


Figure 4.8: Angular power spectrum with (“w/”, solid lines) and without Limber approximation (“w/o”, dashed lines) for the 2 and 4 mJy flux density threshold samples of the LoTSS-DR1 value added source catalogue, masked with “mask z” (*left*) and the corresponding angular two-point correlation function (*right*), calculated from the angular power spectrum.

for CAMB SOURCES, needed to generate a window function, for this analysis uses only sources with redshift $z \leq 2$ (see Fig. 4.7 right). Using also sources with higher redshifts leads to an increased ringing in the angular two-point correlations, which might be caused by stronger shot noise contributions at higher redshifts. CAMB SOURCES uses a spline interpolation to generate a smooth redshift distribution from the given sample redshift distribution, which might fail at high redshifts, due to the low number of sources at high redshifts. Unfortunately it is not possible to access the generated spline interpolation and therefore the sample redshift distribution is cut at an upper limit, where the shot noise is roughly below 10%.

Using the halo-fit option to calculate contributions from non-linear theory affects the angular two-point correlation function only on small angular separations below $\theta \sim 1$ deg. Above 1 deg degree the expectation with halo-fit is equal to using only linear theory. The strongest effect over all angular scales is observed by varying the galaxy bias from a constant value to a functional form. In this case the galaxy bias of Nusser and Tiwari (2015) gives a good agreement to the 2 mJy “mask z” sample (Siewert et al., 2020a), whereas the constant bias, chosen from Planck Collaboration et al. (2018b), results in weaker correlation over all angular separations.

Additionally, it is possible to use the Limber approximation starting at a given multipole, which is by default the case for $l \geq 100$. Using the Limber approximation decreases the necessary computation time of CAMB SOURCES significantly, but could also lead to inaccuracies in the angular two-point correlation function. In Figure 4.8 (left), the calculated power spectrum for the 2 and 4 mJy flux density threshold samples of the LoTSS-DR1 value added source catalogue, masked with “mask z” are shown with Limber (“w/”, solid line) and without Limber approximation (“w/o”, dashed line). Furthermore

the halo-fit, together with the count lensing option was used to compute the power spectrum up to $l = 4 \times 10^3$. The corresponding expectations for the angular two-point correlation function are also shown in Figure 4.8 (right). In this analysis the angular power spectrum shows an extra peak of power starting at $l = 100$, which extends for the 4 mJy sample up to $l = 200$. Caused by this peak in the power spectrum, the angular two-point correlation starts to strongly deviate at angular separations of $\theta \sim 1$ deg from the solution without Limber approximation, which is caused by the oscillating spherical harmonics in Equation (14) of Siewert et al. (2020a). Therefore, we conclude not to use the Limber approximation in the analysis presented in Siewert et al. (2020a) and the following Sections.

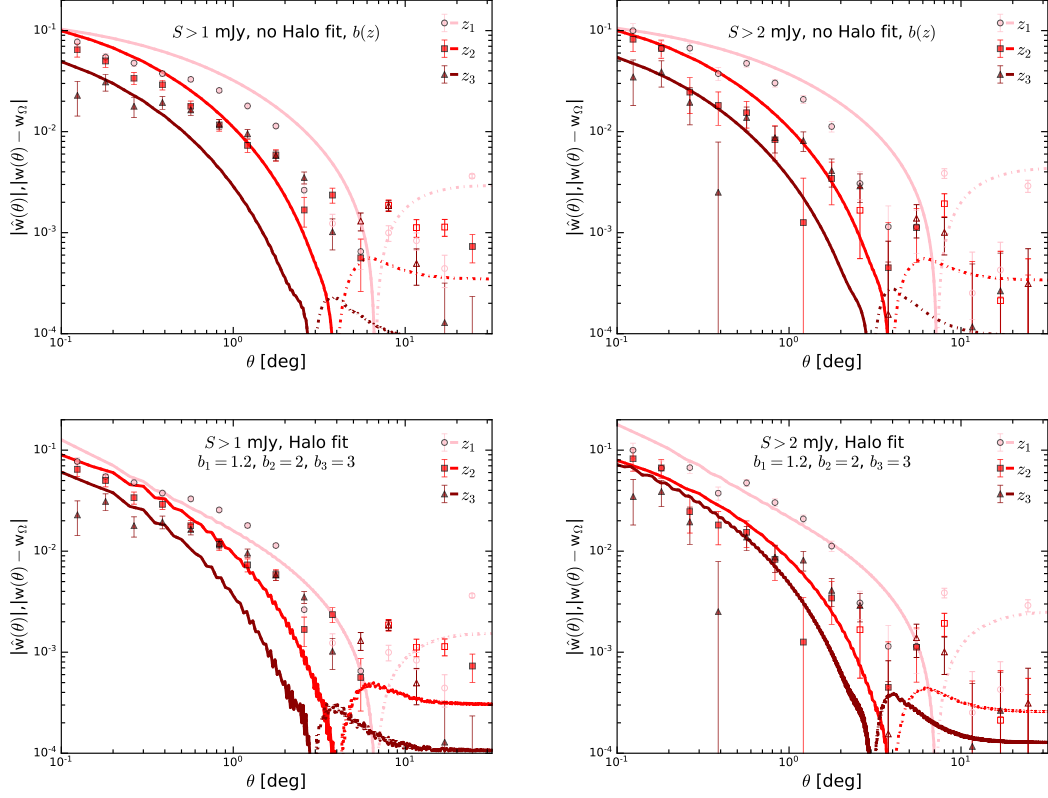


Figure 4.9: Angular two-point correlation function for three redshift bins z_1, z_2 and z_3 for flux density thresholds of 1 (*left*) and 2 mJy (*right*) of “mask z” compared to expectations computed with CAMB SOURCES. For the expectations, we use linear theory together with a redshift dependent bias function (*top*), or non-linear theory together with a piecewise constant bias (*bottom*). Negative values are shown with open symbols and dashed lines. The integral constraint w_Ω is subtracted from the expectations.

4.5.4 Angular two-point correlation function for different redshift bins

In Section 6.3 of Siewert et al. (2020a) the angular two-point correlation function for the three different redshift bins is shown for the 2 mJy flux density threshold of “mask z” and using only non-linear theory. Additionally, the angular two-point correlation was estimated for the 1 mJy sample of “mask z”, which is also compared to expectations of CAMB SOURCES in Figure 4.9. Beside the conclusion from Section 6.1 of Siewert et al. (2020a) using the redshift information of the sources in the LoTSS-DR1 value added source catalogue, the angular correlation is also consistent for the 1 mJy flux density threshold. We see in the top-left panel of Figure 4.9 that the CAMB predictions for the redshift bin z_1 and 1 mJy, using only linear theory and the galaxy bias function $b(z)$ seem to overestimate the amount of correlation while we obtain a reasonable agreement

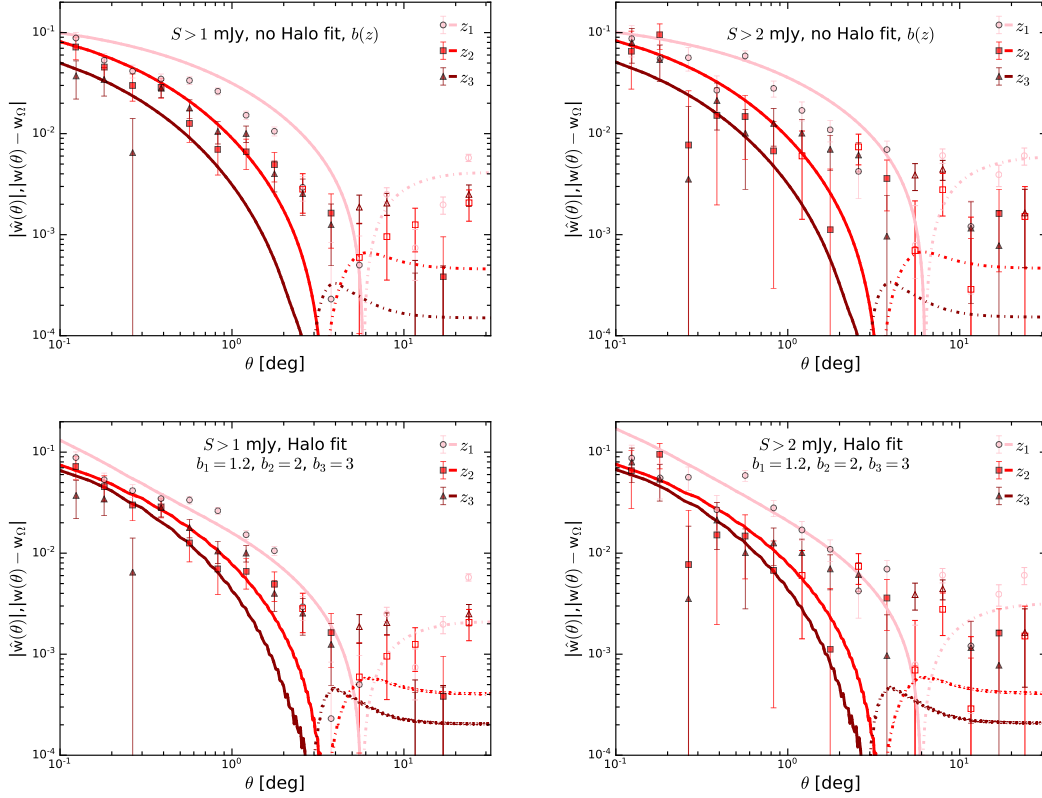


Figure 4.10: Angular two-point correlation function for three redshift bins z_1, z_2 and z_3 for flux density thresholds of 1 (*left*) and 2 mJy (*right*) of “mask z1” compared to expectations computed with CAMB SOURCES. For the expectations, we use linear theory together with a redshift dependent bias function (*top*), or non-linear theory together with a piecewise constant bias (*bottom*). Negative values are shown with open symbols and dashed lines. The integral constraint w_Ω is subtracted from the expectations.

for the z_2 bin at small angular scales ($\lesssim 1$ degree) and for z_3 below ~ 0.5 degrees. For the 2 mJy redshift bins the prediction for the z_1 similarly overestimates the estimated correlation, but it is in better agreement than for 1 mJy. As already shown in Figure 26 of Siewert et al. (2020a), using the halo-fit option and a piecewise constant bias improves the agreement between the theoretical expectations and the estimated two-point correlation function of the 1 and 2 mJy redshift bins z_1 and z_2 . In general the theoretical expectations are comparable between each of 1 and 2 mJy redshift bins. Only the 2 mJy z_1 sample with halofit and constant bias shows a stronger correlation than for the corresponding 1 mJy sample.

The two-point correlation function is additionally estimated for the three redshift cuts masked with the “mask z1” introduced in Section 6.2 of Siewert et al. (2020a) and compared to theoretical expectations. In Figure 4.10 the results of this test are shown,

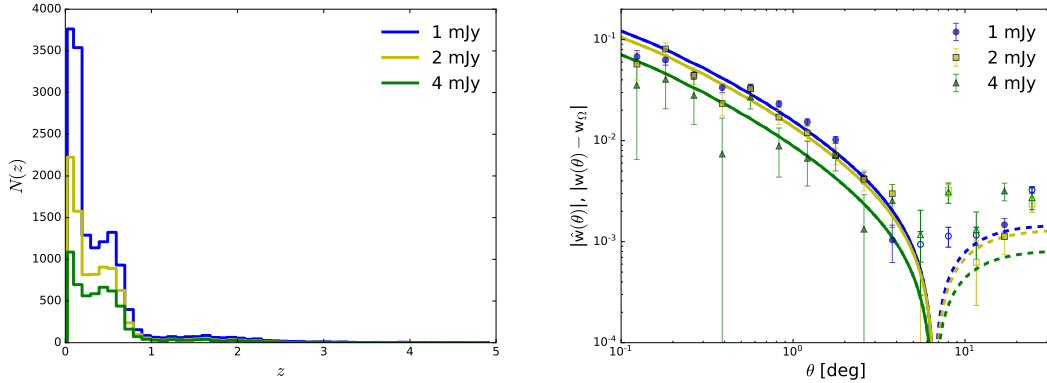


Figure 4.11: *Left*: Redshift distribution of LoTSS-DR1, masked with “mask z”, with additional redshift quality cut and with flux density thresholds of 1, 2 and 4 mJy. *Right*: Corresponding estimated angular two-point correlation function (points) and expectations, based on CAMB SOURCES simulations with Planck best-fit cosmological parameters, with subtracted integral constraint (lines). Negative values are shown with open symbols and dashed lines.

which produces consistent results for the 1 mJy redshift bins compared to “mask z”. As the sample sizes decrease significantly using “mask z1”, the 2 mJy redshift bins vary more strongly than their counterparts of “mask z”. The theoretical expectations from CAMB SOURCES are not directly affected by the decreasing number of sources, as they use the normalized redshift distributions for the window function. However, we find within error bars good agreement between the estimated angular two-point correlation function and the theoretical expectations, using non-linear theory and a piecewise constant bias.

4.6 Quality cut on redshift distribution

The redshift dependent estimations of the angular two-point correlation function, published in Siewert et al. (2020a), are limited by the quality of the redshift estimations. The published best-fit redshift estimates (Duncan et al., 2019) are based either on spectroscopic or on photometric redshifts from cross matching the LoTSS-DR1 sources to PanSTARSS and WISE sources. In order to have a better quality control on the redshift distribution, a quality cut can be formulated, where only sources with

$$\frac{z_{\max} - z_{\min}}{2(1 + z_{\text{best}})} < 0.1 \quad (4.2)$$

are used. The cut is based on the maximum z_{\max} and minimum z_{\min} redshift of the 80% fit interval, as well as the best fit redshift z_{best} . Additionally, we reject all sources, which redshift estimates are based only on the spectroscopic redshifts. Applying this quality cut to the LoTSS-DR1 sources and using the same flux density threshold as in

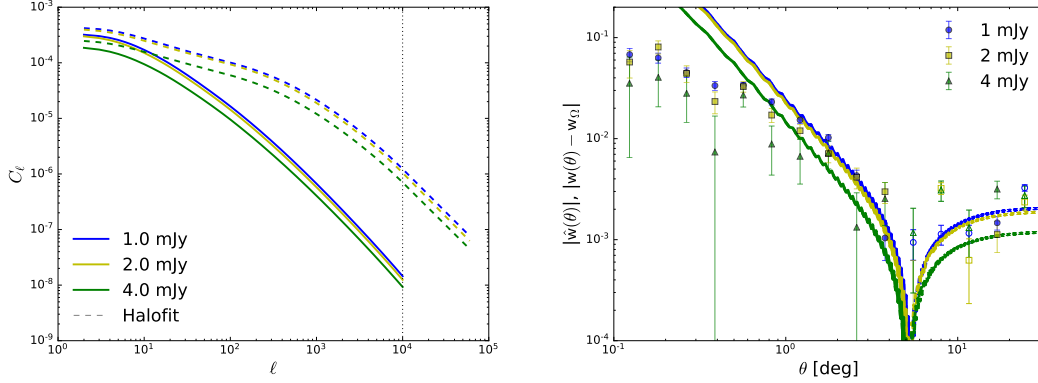


Figure 4.12: *Left*: Comparison of angular power spectrum derived from only linear theory (solid lines), or halo-fit model (dashed lines). *Right*: Estimated angular two-point correlation function (points) with expectations from CAMB SOURCES using halo-fit (lines).

Siewert et al. (2020a) together with the “mask z”, the total number of sources reduces to 14 831, 8790 and 5336, for 1, 2 and 4 mJy, respectively. With a purely random sample of 20 times the number of sources than the data sample, the estimated angular two-point correlation function $\hat{w}(\theta)$, using TREECORR (Jarvis et al., 2004, version 4.1.3), is shown in Figure 4.11. In comparison to Figure 24 of Siewert et al. (2020a), the separation of the angular bins is chosen to be $\Delta \ln(\theta/1 \text{ deg}) = 0.4$ in order to overcome stronger shot noise contributions in the pair counts.

Like in Siewert et al. (2020a), theoretical expectations for $w(\theta)$ from simulations can be derived. The expectations, shown in Figure 4.11, are calculated with Equation (14) of Siewert et al. (2020a) using numerical calculations from CAMB SOURCES with only linear theory, together with best-fit cosmological parameters from Planck Collaboration et al. (2018b) and especially the galaxy bias $b = 1.2$. The sum of Equation (14) is calculated for an $l_{max} = 10^4$, which is enough to let the sum converge and is still justifiable in terms of computation time. From the theoretical expectations the integral constraint w_Ω , defined in Equation (28) from Siewert et al. (2020a), is subtracted. Comparing Figure 4.11 to Figure 24 of Siewert et al. (2020a), one can see that all three flux density threshold samples are more self-consistent, as well as in better agreement to the theoretical expectations. Still, a slight increased correlation around 1 deg is visible when compared to the expectations and to the 2 and 4 mJy samples.

Additionally to only using linear theory in the simulations, the halo-fit option of CAMB SOURCES can be used. This option will by default implement the non-linear theory of Mead et al. (2016). To let the sum of Equation (14) converge in this case, the used l_{max} is not enough and therefore the simulated C_l ’s are extended up to $l = 6 \times 10^4$. This extrapolation is done by fitting a power law of the form

$$C_l^{fit} \propto l^\beta \quad (4.3)$$

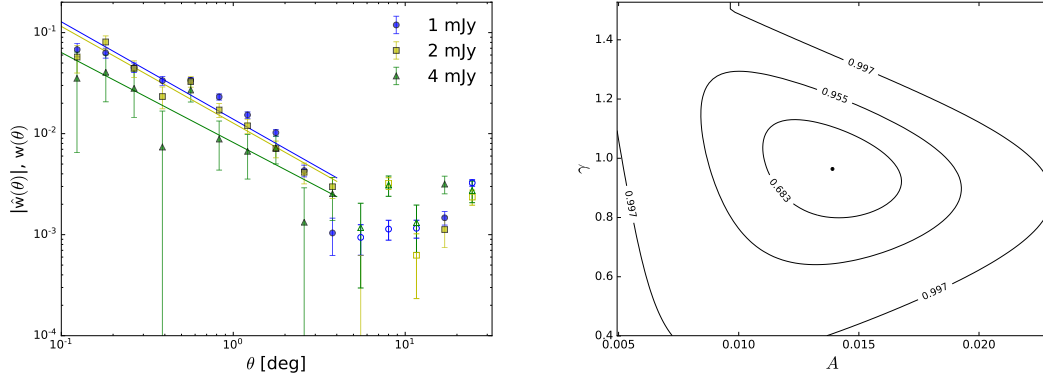


Figure 4.13: Angular two-point correlation function with power law of the form $w(\theta) = A\theta^{-\gamma}$ fitted to the data of the 1,2 and 4 mJy “quality cut” samples (*left*). The best-fit results are shown with their 68%, 95% and 99% confidence regions (*right*) for the 1 mJy “quality cut” sample. Negative values are shown with open symbols.

to the last two C_l , which is adapted from the Core Cosmology Library (CCL¹, Chisari et al., 2019) package. The resulting power spectra using non-linear theory and the extension up $l = 6 \times 10^4$ are shown in left panel of Figure 4.12. The change between simulated C_l and the fitted extension is highlighted by a vertical dashed line at $l = 10^4$. Using this extended power spectrum, the inferred angular two-point correlation function is shown in the right panel of Figure 4.12. Going up to $l = 6 \times 10^4$ the power spectra with non-linear theory still do not decrease to amplitudes of 10^{-8} , like using only linear theory, which results in a ringing in the estimated correlation function. Due to the increased values of C_l on all scales, especially for larger multipole moments l , the computed angular two-point correlation shows an excess of correlation at angular scales below one degree.

Like in Siewert et al. (2020a), a power law can be fitted to the estimated angular two-point correlation functions of the quality cut samples. The results of this fit procedure are shown in Figure 4.13 (left). The power law is fitted to the data on the range of $0.1 \leq \theta \leq 4.0$ deg, which gives in this case more consistent results than for the range $0.2 \leq \theta \leq 2.0$ deg of Siewert et al. (2020a). For the 1 mJy “quality cut” sample an amplitude of $A = (13.90 \pm 1.88) \times 10^{-3}$ with an slope of $\gamma = 0.96 \pm 0.11$ is found. The corresponding confidence regions of the 1 mJy fit are shown in Figure 4.13 (right), while the reported errors belong to the 68% confidence level. For increasing flux density thresholds a decreasing correlation amplitude of $A = (12.71 \pm 1.27) \times 10^{-3}$ for 2 mJy and $A = (8.18 \pm 1.46) \times 10^{-3}$ for 4 mJy is found. Together with the decreasing correlation amplitude, the correlation function itself flattens in the fitted range and the fitted slope decreases slightly, with $\gamma = 0.95 \pm 0.08$ for 2 mJy and $\gamma = 0.89 \pm 0.16$ for 4 mJy respectively. Over all the results of the fitted power law exceed the results of the “mask z” and “mask z1” samples of Siewert et al. (2020a) in terms of correlation amplitude A ,

¹<https://github.com/LSSTDESC/CCL>

whereas the slope γ is consistent to previous measurements. Introducing the quality cut to the redshift estimates, the median, as well as the mean redshift of the flux density threshold samples decreases significantly compared to the “Any z ” sample of Siewert et al. (2020a). For the 1 mJy sample the mean redshift decreases from $\bar{z} = 0.59$ of the “Any z ” sample to $\bar{z} = 0.38$ and the median from $z_{med} = 0.50$ to $z_{med} = 0.37$ respectively. The decreasing mean redshift indicates a selection bias towards smaller redshifts and therefore more local structures. These structures are expected to be more clustered, which can explain the higher correlations observed in the “quality cut” samples and of the different redshift bin samples of Siewert et al. (2020a) and Section 4.5.4.

4.7 Comparison of the angular two-point correlation function

The estimated angular two-point correlation functions in Siewert et al. (2020a) have already been briefly compared to other results from the literature. A more detailed comparison of the fit results from a simple power law (see also Eq. (31) in Siewert et al., 2020a):

$$w(\theta) = A \left(\frac{\theta}{1 \text{ deg}} \right)^{-\gamma} \quad (4.4)$$

is presented in Table 4.1 and Figure 4.14. The Table 4.1 was conducted for estimators with similar bias and variance, namely the Hamilton (1993, H) and the Landy and Szalay (1993, LS) estimators, while in Siewert et al. (2020a) the LS estimator was used. For a detailed discussion and testing of the different estimator see App. C in Siewert et al. (2020a) and Biermann et al. (in preparation). Table 4.1 additionally shows the angular scales to which the model was fitted. Observing angular scales $\theta < 0.1$ deg, the clustering is expected to originate from multiple sources within the same dark matter halo, while the correlation for larger scales is expected to come dominantly from sources between different dark matter halos. In the work of Dolfi et al. (2019), they found for a sample of the TGSS-ADR1 source catalogue with a flux density threshold of 150 mJy and scales $\theta \leq 0.1$ deg an amplitude of $A = (6.5 \pm 0.6) \times 10^{-5}$ with a slope of $\gamma = 2.87 \pm 0.02$. For scales $\theta > 0.1$ the measured angular two-point correlation flattens significantly. The results of Siewert et al. (2020a) have been fitted in the range of $0.2 \text{ deg} \leq \theta \leq 2 \text{ deg}$, therefore only results with a similar range are compared. In terms of correlation amplitude, consistent values can be found between LoTSS-DR1, WENSS, SUMSS, FIRST, and NVSS, especially for the LoTSS-DR1 2 and 4 mJy sample of “mask d”. For the faintest samples of LoTSS-DR1, the measured amplitudes are also in agreement to the results from fainter TGSS-ADR1 samples (Rana and Bagla, 2019). Different measurements at 4.85 GHz (Loan et al., 1997; Rengelink, 1999), as well as at 232 MHz (de Oliveira-Costa and Lazio, 2010) show a significant excess in the amplitudes compared to all other measurements. In addition to the measurements from radio surveys, the results are compared to measurements from an optical survey (APM; Maddox et al. 1996). For some results in Table 4.1 the slope of Equation (4.4) has been fixed and only the am-

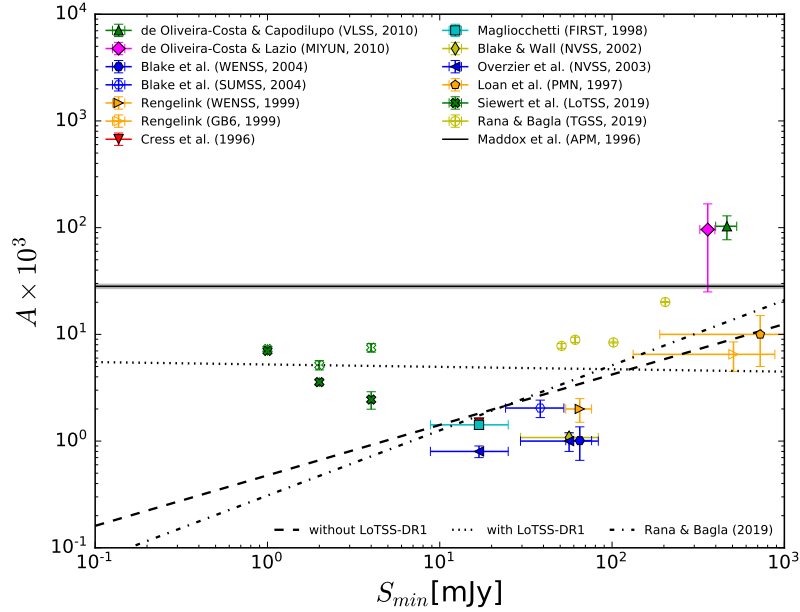


Figure 4.14: Comparison of angular two-point correlation amplitude from Siewert et al. (2020a) for the LoTSS-DR1 with “mask d” (full symbols) and “mask 1” (open symbols) to earlier results from the literature. Errors in the amplitude are 68% confidential intervals of the fit and errors in the flux density corresponds to uncertainties in the flux density scaling from the observed frequency to 144 MHz with $\alpha = 0.76 \pm 0.21$. Additionally the results of the fit of Equation (4.5) are shown for values from Table 4.1 without (dashed) and without LoTSS-DR1 (dotted), as well as for the results of Rana and Bagla (2019) (dashed dotted).

plitude was varied (Loan et al., 1997; Rengelink, 1999; Overzier et al., 2003). The fixed slopes are shown with their corresponding values in brackets. In order to produce Figure 4.14, the flux density thresholds of Table 4.1 are scaled to 144 MHz, using a spectral index of $\alpha = 0.76 \pm 0.21$ (Tiwari, 2016). Errors on the scaled flux density threshold are estimated by propagating the uncertainty of the spectral index. Rana and Bagla (2019) claim to observe an reasonable fit of a flux density dependent correlation amplitude of the form:

$$\log_{10}(A(S) \times 10^3) = a + b \log_{10} \left(\frac{S}{1 \text{ mJy}} \right) \quad (4.5)$$

with $a = -0.51 \pm 0.59$ and $b = 0.61 \pm 0.33$ (see Fig. 4.14 dashed dotted line). For fitting the same power law of Equation (4.5), the python package LMFIT (Newville et al., 2016) was used and the fit results are presented with the 68.25% confidence interval from the Levenberg-Marquardt minimization routine. Fitting the power law of Equation (4.5) to the values presented in Table 4.1, without the results from LoTSS-DR1 gives $a = -0.32 \pm 0.45$ and $b = 0.47 \pm 0.22$ (see Fig. 4.14 dashed line), which is in good

agreement to the results of Rana and Bagla (2019). In this work a different estimation of Cress et al. (1996) was used than in Rana and Bagla (2019), which can explain the difference in the fitted parameters.

These findings might reflect an increasing correlation amplitude with increasing flux density threshold, but are within two sigma also consistent with a constant correlation amplitude. Based on the Bootes field observed at 1.4 GHz, Wilman et al. (2003) found a similar trend in their estimated angular two-point correlation functions. But their fitted amplitudes are also in agreement with no detection, due to the large errors on the estimated correlation amplitude. The error bars increase consistently with the decreasing number of sources and are therefore strongly affected by shot noise. The estimated correlation amplitude increases in the same consistent behaviour and is therefore also expected to be driven by shot noise. The fit results might also be driven by results from de Oliveira-Costa and Lazio (2010), as they also probe scales below 0.1 deg and therefore find an increased correlation amplitude. Results from Loan et al. (1997) and Rengelink (1999) also probe scales below 0.1 deg and additionally fix the slope of Equation (4.4). When additionally including the results from LoTSS-DR1 to the power law fit, the best-fit results change to $a = 0.72 \pm 0.13$ and $b = -0.02 \pm 0.09$ (see Fig. 4.14 dotted line). These results are consistent with a constant angular two-point correlation function amplitude, which is consistent with findings from Rengelink (1999) and Blake et al. (2004).

Table 4.1: Comparison of best-fit results from a power law (Eq. 4.4) to the angular two-point correlation function from the literature. Shown are the survey, the frequency ν and the bandwidth $\Delta\nu$ of the survey. The fit results are shown with amplitude A and slope γ . If the slope was fixed in the fit, the corresponding values are shown in brackets. Additionally the estimator in use is highlighted, which is either Landy and Szalay (1993, LS) or Hamilton (1993, H).

Survey	Reference	ν [MHz]	S_{lim} [mJy]	A ($\times 10^{-3}$)	γ	Est.	Fit range [deg]
VLSS	de Oliveira-Costa and Capodilupo (2010)	74	770	103 ± 26	1.21 ± 0.35	H	$0.2 \leq \theta \leq 0.6$
LoTSS	Siewert et al. (2020a), “mask d”	144	1	$7.00^{+0.18}_{-0.18}$	$0.58^{+0.04}_{-0.04}$	LS	$0.2 \leq \theta \leq 2$
LoTSS	Siewert et al. (2020a), “mask d”	144	2	$3.57^{+0.25}_{-0.25}$	$0.67^{+0.10}_{-0.10}$	LS	$0.2 \leq \theta \leq 2$
LoTSS	Siewert et al. (2020a), “mask d”	144	4	$2.45^{+0.45}_{-0.26}$	$0.87^{+0.24}_{-0.23}$	LS	$0.2 \leq \theta \leq 2$
LoTSS	Siewert et al. (2020a), “mask 1”	144	1	$7.20^{+0.42}_{-0.42}$	$0.68^{+0.08}_{-0.08}$	LS	$0.2 \leq \theta \leq 2$
LoTSS	Siewert et al. (2020a), “mask 1”	144	2	$5.11^{+0.59}_{-0.69}$	$0.74^{+0.16}_{-0.16}$	LS	$0.2 \leq \theta \leq 2$
LoTSS	Siewert et al. (2020a), “mask 1”	144	4	$7.45^{+0.95}_{-0.95}$	$0.46^{+0.21}_{-0.20}$	LS	$0.2 \leq \theta \leq 2$
TGSS	Rana and Bagla (2019)	147.5	50	7.8 ± 0.4	0.821 ± 0.072	LS	$1 < \theta$
TGSS	Rana and Bagla (2019)	147.5	60	8.9 ± 0.5	0.760 ± 0.053	LS	$1 < \theta$
TGSS	Rana and Bagla (2019)	147.5	100	8.4 ± 0.1	0.716 ± 0.104	LS	$1 < \theta$
TGSS	Rana and Bagla (2019)	147.5	200	20.1 ± 0.2	1.24 ± 0.132	LS	$1 < \theta$
MIYUN	de Oliveira-Costa and Lazio (2010)	232		96 ± 71	1.12 ± 0.11	H	$\theta < 0.6$
WENSS	Rengelink (1999)	325	35	2.0 ± 0.5	(0.8)	H	
WENSS	Blake et al. (2004)	325	35	1.01 ± 0.35	1.22 ± 0.33	LS	$0.2 < \theta$
SUMSS	Blake et al. (2004)	843	10	2.04 ± 0.38	1.24 ± 0.16	LS	$0.2 < \theta$
FIRST	Cress et al. (1996)	1400		2.0 ± 0.3	1.26 ± 0.04	LS	$0.02 < \theta < 2$
FIRST	Magliocchetti et al. (1998)	1400	3	1.52 ± 0.06	1.68 ± 0.07	LS	$0.01 < \theta$
FIRST	Overzier et al. (2003)	1400	3	1.2 ± 0.1	(0.8)	H	$0.3 \leq \theta$
FIRST	Overzier et al. (2003)	1400	10	1.9 ± 0.3	(0.8)	H	$0.3 \leq \theta$
NVSS	Blake et al. (2004)	1400	10	1.49 ± 0.15	1.05 ± 0.10	LS	$0.3 < \theta$
NVSS	Blake and Wall (2002)	1400	10	1.08 ± 0.09	0.85 ± 0.1	LS	$0.1 < \theta$
NVSS	Overzier et al. (2003)	1400	3	0.8 ± 0.1	(0.8)	H	$0.3 \leq \theta$
NVSS	Overzier et al. (2003)	1400	10	1.0 ± 0.2	(0.8)	H	$0.3 \leq \theta$
PMN	Loan et al. (1997)	4850	50	10.00 ± 5.00	(0.8)	H	$0 \leq \theta \leq 10$
GB6	Rengelink (1999)	4850	35	6.5 ± 2.0	(0.8)	H	
APM	Maddox et al. (1996)			28.2 ± 1.2	0.679 ± 0.001		$0.01 < \theta < 0.1$

4.8. ESTIMATING THE ANGULAR TWO-POINT CORRELATION FUNCTION FROM DIFFERENT SURVEYS

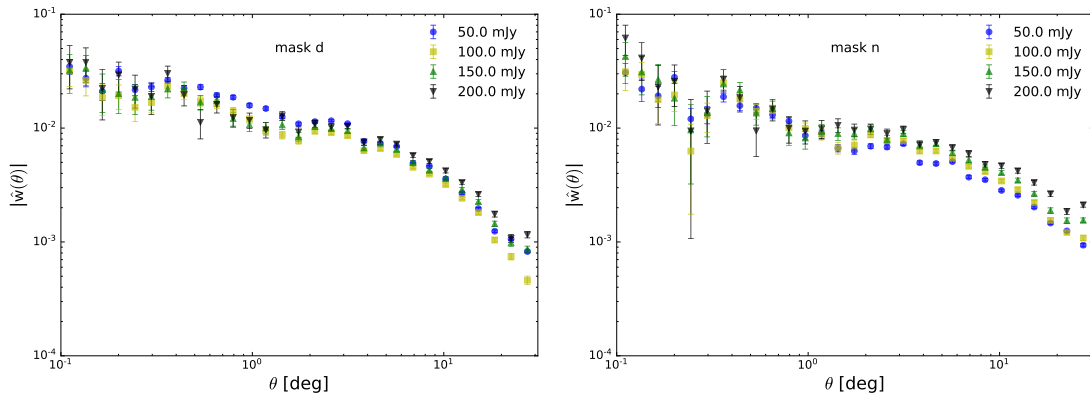


Figure 4.15: Estimated angular two-point correlation function of TGSS-ADR1 with flux density thresholds of 50, 100, 150, and 200 mJy, masked with “mask d” (*left*) and “mask n” (*right*). Negative values are shown with open symbols.

4.8 Estimating the angular two-point correlation function from different surveys

The routines and procedures defined in Siewert et al. (2020a), combined with the masks defined in Siewert et al. (2020b) can be used to estimate the angular two-point correlation function from the TGSS-ADR1, WENSS, SUMSS and NVSS source catalogues. In comparison to Appendix A of Siewert et al. (2020a), the masks of Siewert et al. (2020b) are defined in a lower HEALPIX resolution of $N_{side} = 16$. To each of the surveys four different flux density thresholds are applied, which follow Siewert et al. (2020b). For the SUMSS and NVSS source catalogues, the lowest flux density threshold of 18 and 15 mJy are abandoned in order to ease the analysis to a common set of flux density thresholds of 25, 35, 45, and 55 mJy. As the TGSS-ADR1 source catalogue is only complete at higher flux densities, the set of flux density thresholds for this survey is defined as 50, 100, 150, and 200 mJy. In the Figures 4.15, 4.17, 4.19, and 4.21 the results of the estimates from TREECORR (Jarvis et al., 2004) with a logarithmic angular bin width of $\Delta \ln(\theta/1 \text{ deg}) = 0.2$ for each survey are shown. The rest of the parameters of TREECORR have been kept the same, like described in Siewert et al. (2020a). For the random sample, we randomly generate 20 times the number of sources of each data sample on the masked sphere. In order to compare the results of the four different surveys, the angular two-point correlation function was fitted to the power law of Equation (4.4). Like in Siewert et al. (2020a), the python package LMFIT is used for the fitting procedure, while the integral constraint is neglected in the following sections. The range of $0.2 \text{ deg} \leq \theta \leq 2.0 \text{ deg}$ to which the power law is fitted has been kept the same for all four surveys, masks and different flux density thresholds. In the left panels of the Figures 4.16, 4.18, 4.20, and 4.22 the fit results for one flux density threshold for “mask d” and “mask n” are shown as solid and dashed lines. The confidence intervals of 68.3%, 95.5%, and 99.7% for the

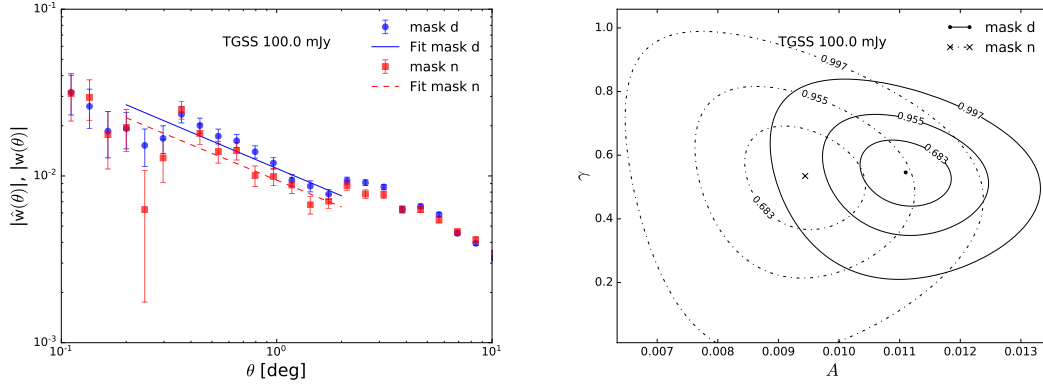


Figure 4.16: Angular two-point correlation of TGSS-ADR1 with 100 mJy flux density threshold and masked with “mask d” and “mask n” (*left*). The data is fitted to a power law $w(\theta) = A\theta^{-\gamma}$ (*left*, lines) and the best-fit results are shown with 68%, 95%, and 99% confidence intervals (*right*) for both masks.

corresponding fits of the left panel are shown in the right panel of the same figures.

4.8.1 TGSS-ADR1 angular two-point correlation

The estimated angular two-point correlation functions of the TGSS-ADR1 (Intema et al., 2017) show consistent behaviour for all four flux density thresholds and both masks. A slight discrepancy can be found for the 50 mJy “mask d”, which shows higher correlation around angular separations of $\theta \sim 1$ deg. Over nearly all angular scales in Figure 4.15 a increasing flux density threshold, except for the formerly mentioned sample, coincidences with a larger two-point correlation. The results of the power law (Eq. 4.4) fitted to the estimated angular two-point correlation, presented in Table 4.2, confirm the observed correlation enhancement for higher flux density thresholds.

As seen before, the 50 mJy “mask d” shows also in the fit results a stronger correlation at 1 deg, which exceeds all amplitudes found for the other flux density thresholds. Using the more aggressive “mask n” seems to affect the 50 mJy flux density threshold the most, where the largest difference of the fitted correlation amplitude is found. Masking regions with higher noise helps in this case to focus the estimation on regions, which are already complete at lower flux density thresholds. With an increasing flux density threshold and increasing correlation amplitude at an pivot scale of 1 deg, the slope of the fitted power law tends to decrease. A similar trend of increasing correlation amplitudes with decreasing slope was observed in similar study of Rana and Bagla (2019) for the 50, 60, and 100 mJy flux density threshold samples, whose results are presented in Table 4.1. The fourth sample of their analysis with a flux density threshold of 200 mJy shows a significantly increased correlation amplitude, which exceeds the amplitudes found in this work. In general the masking strategy of Rana and Bagla (2019) is similar to the “mask n” of Siewert et al. (2020b), but is based on a different HEALPIX resolution of

4.8. ESTIMATING THE ANGULAR TWO-POINT CORRELATION FUNCTION FROM DIFFERENT SURVEYS

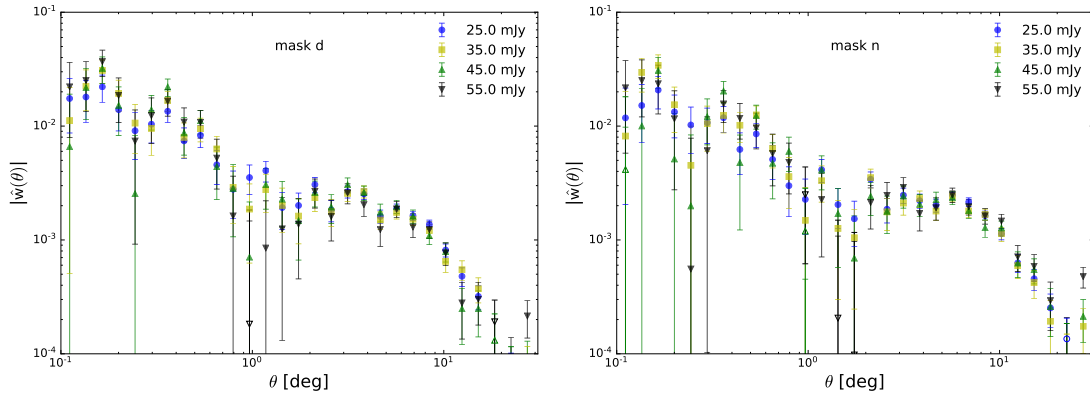


Figure 4.17: Estimated angular two-point correlation function of WENSS with flux density thresholds of 25, 35, 45, and 55 mJy, masked with “mask d” (*left*) and “mask n” (*right*). Negative values are shown with open symbols.

$N_{Side} = 1024$, which could explain the relatively good agreement between the 50 and 100 mJy “mask n” fit results and the 50, 60, and 100 mJy samples of Rana and Bagla (2019). The difference in the slope between the fitted slopes in this thesis and Rana and Bagla (2019) is explained by the lower limit of the fit range, which is in their case set to one degree. In Figure 4.15 the angular two-point correlation steepens at angular scales $\theta \gtrsim 3$ deg, which indicates a change of slope and therefore could correspond to the larger slopes found in Rana and Bagla (2019). Another change of slope was found for angular separations $\theta < 0.1$ deg by Dolfi et al. (2019), with an increased slope of $\gamma = 2.87 \pm 0.02$. Studying the power spectrum of the TGSS-ADR1, Tiwari et al. (2019) found large-scale offset of the TGSS-ADR1 flux density while comparing to the GLEAM (Hurley-Walker et al., 2017) source catalogue. This flux density offset will result in excess of power at low multipoles and larger angular scales, which could explain the excess of correlation observed for angular scales $\theta > 10$ deg.

4.8.2 WENSS angular two-point correlation

For the WENSS (de Bruyn et al., 2000) source catalogue, the estimated angular two-point correlation is in good agreement between the two different masks and the four different flux density thresholds. Comparing the estimated two-point correlation function of the WENSS in Figure 4.17 to the TGSS-ADR1 in Figure 4.15 a more strongly varying slope can be observed. Below angular separations of one degree, the two-point correlations follow continuously a single power law and changes direction between one and two degree, with an peak at two to three degree. For angular separations larger three degrees, the two-point correlation starts to decrease again. In Figure 4.17 no clear flux depended correlation can be observed, like for the TGSS-ADR1 in Section 4.8.1. Fitting the same power law of Equation (4.4) as before to the angular separations between 0.2 deg and 2 deg reveals a significantly smaller correlation amplitude than for the TGSS-ADR1 with

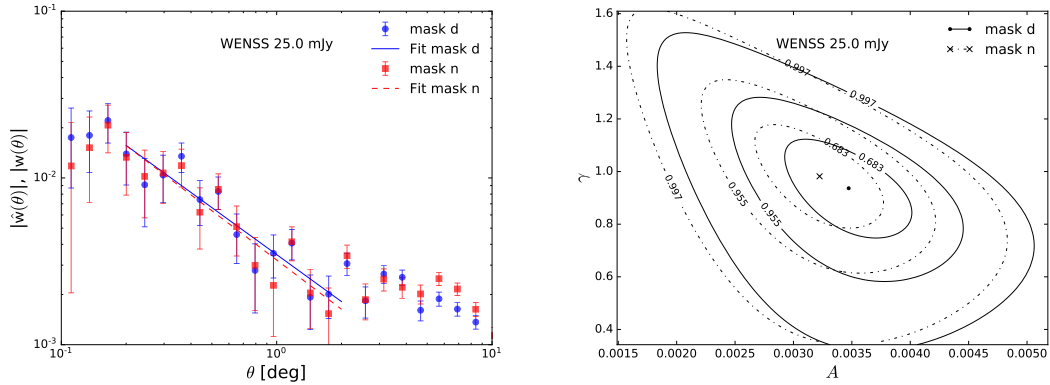


Figure 4.18: Angular two-point correlation of WENSS with 25 mJy flux density threshold and masked with “mask d” and “mask n” (*left*). The data is fitted to a power law $w(\theta) = A\theta^{-\gamma}$ (*left*, lines) and the best-fit results are shown with 68%, 95%, and 99% confidence intervals (*right*) for both masks.

a much steeper slope (see Table 4.2). As already seen in Figure 4.17, the correlation of the four flux density thresholds is in good agreement to each other and also between the two different masks. For both masks the best fitted power law in terms of $\chi^2/\text{d.o.f.}$ is found for the 25 mJy flux density thresholds, which in both cases shows the largest correlation amplitude of $A = (3.47 \pm 0.36) \times 10^{-3}$ and $A = (3.22 \pm 0.36) \times 10^{-3}$ for “mask d” and “mask n”, respectively (see Fig. 4.18). The resulting slope of the power law is found to be smallest for the 25 mJy flux density threshold. Contrariwise to the indistinguishable flux density dependency in the Figures 4.17 and 4.18, the results of the fit in Table 4.2 reveal a decreasing correlation amplitude with increasing flux density threshold. With the decreasing correlation amplitude the slope of the correlation steepens, e.g. from $\gamma = 0.937 \pm 0.122$ for 25 mJy to $\gamma = 1.389 \pm 0.272$ for 55 mJy of “mask d”. This flux density dependency is contrary to the results presented in Section 4.8.1 for the TGSS-ADR1.

In a previous study, Rengelink (1999) found for the WENSS with a flux density threshold of 35 mJy a correlation amplitude of $A = (2.0 \pm 0.5) \times 10^{-3}$, while fixing the slope to $\gamma = 0.8$. Estimates for different flux density thresholds did not show a clear change in the correlation amplitude, which might be an effect of the fixed slope. This estimate is still biased by the catalogue version used for the analysis, as Rengelink (1999) uses a preliminary version of the catalogue, which covers only 570 square degrees (Rengelink et al., 1997) and contains 11 299 sources. The catalogue used in the analysis of this section is the most recent one, presented in de Bruyn et al. (2000), and contains 229 420 sources, while covering 2298 square degrees. In a more recent work of Blake et al. (2004) regarding the SUMSS survey, the angular two-point correlation of the WENSS survey has also been estimated. Blake et al. (2004) found a similar shape of the estimated angular two-point correlation, like shown in Figure 4.17, with a reasonable good fit of

4.8. ESTIMATING THE ANGULAR TWO-POINT CORRELATION FUNCTION FROM DIFFERENT SURVEYS

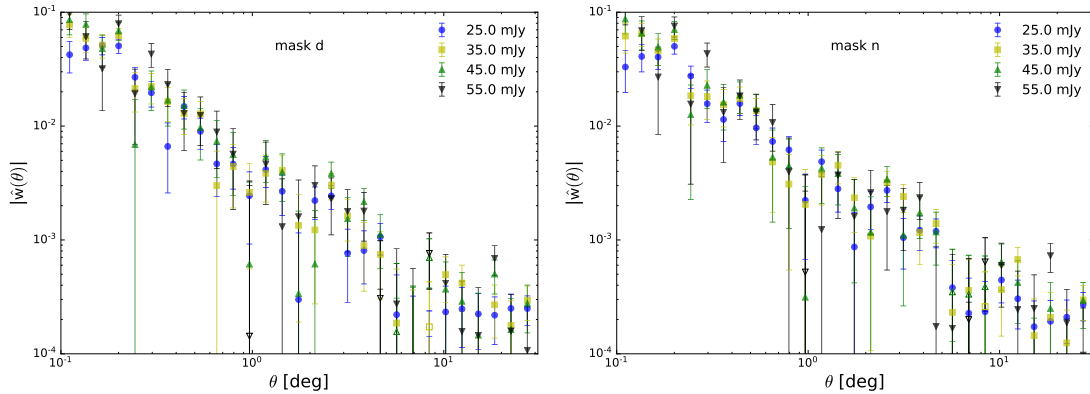


Figure 4.19: Estimated angular two-point correlation function of SUMSS with flux density thresholds of 25, 35, 45, and 55 mJy, masked with “mask d” (*left*) and “mask n” (*right*). Negative values are shown with open symbols.

a double power law to a sample with 35 mJy peak flux density threshold. For a single power law with a lower fit range of $\theta > 0.2$ deg they found a correlation amplitude of $A = (1.01 \pm 0.35) \times 10^{-3}$ with a fitted constant offset of $(0.35 \pm 0.19) \times 10^{-3}$, which has a similar role like the integral constraint. The fitted slope is given as $\gamma = 1.22 \pm 0.33$, which is in good agreement to the best-fit results of Table 4.2 for all flux density thresholds. The comparison of the correlation amplitude is complicated by the fitted constant offset, but in most of the cases the results of Table 4.2 show a stronger correlation than in Blake et al. (2004).

4.8.3 SUMSS angular two-point correlation

The estimated angular two-point correlations of SUMSS (Mauch et al., 2003) for “mask d” and “mask n” are shown in Figure 4.19. For the different flux density thresholds, the estimated angular two-point correlation function seems to vary more strongly than for WENSS, or TGSS, but from Figure 4.19 no clear flux density dependence can be observed. Between the two different masks, the observed correlation is comparable and shows a similar trend. Over the observed range of angular separations the angular two-point correlation function shows no clear features, except for a flattening for angular separations $\theta < 0.2$ deg of the 25 mJy flux density threshold in both mask samples. This flattening is more visible plotting only the 25 mJy samples in Figure 4.20. Fitting the same power law from the former, the resulting correlation amplitudes and slopes are presented in Table 4.2. In comparison to results from the Sections 4.8.1 and 4.8.2, the fit of the power law to the SUMSS data shows a better agreement and continuity regarding the $\chi^2/\text{d.o.f.}$. The fitted correlation amplitudes of all flux density thresholds and masks are in good agreement to the results of WENSS. Contrariwise, the slope of the power law is found to be steeper, e.g. for “mask d” with values between $\gamma = 1.560 \pm 0.350$ and $\gamma = 1.833 \pm 0.283$, than for TGSS and WENSS. In terms of $\chi^2/\text{d.o.f.}$, the best fitted

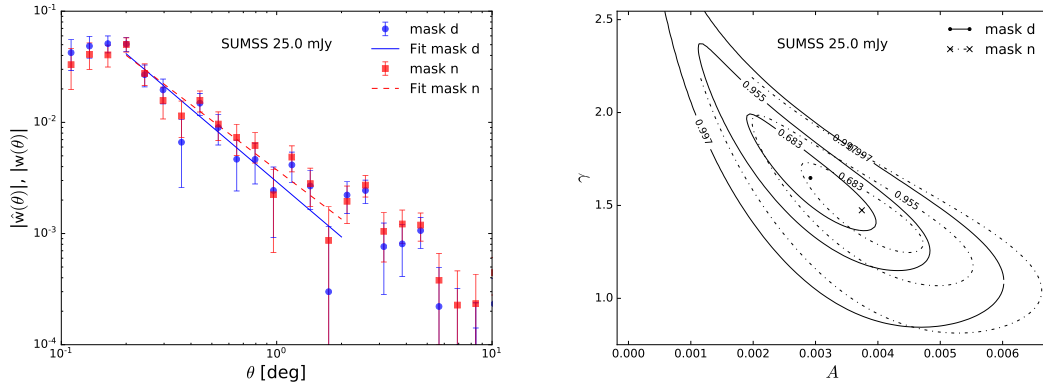


Figure 4.20: Angular two-point correlation of SUMSS with 25 mJy flux density threshold and masked with “mask d” and “mask n” (*left*). The data is fitted to a power law $w(\theta) = A\theta^{-\gamma}$ (*left*, lines) and the best-fit results are shown with 68%, 95%, and 99% confidence intervals (*right*) for both masks.

power law is found for the 55 mJy “mask d” sample with $A = (3.41 \pm 1.12) \times 10^{-3}$ and $\gamma = 1.833 \pm 0.283$, and for the 25 mJy “mask n” sample with $A = (3.74 \pm 0.65) \times 10^{-3}$ and $\gamma = 1.474 \pm 0.163$.

Comparing the estimated angular two-point correlation functions of this analysis to results from the literature, like Blake et al. (2004), the fitted correlation amplitudes are in reasonable agreement. Blake et al. (2004) reports the fitted single power law as $A = (2.04 \pm 0.38) \times 10^{-3}$ and $\gamma = 1.24 \pm 0.16$ for a flux density threshold of 10 mJy. Initially, they fitted a sum of two power laws to the estimated angular two-point correlation with a clear break at $\theta \approx 0.1$ deg. For angular separations $\theta \gtrsim 0.1$ deg, they additionally investigated the dependence of the fitted power law to the flux density threshold and found within error bars no clear change in the correlation amplitude.

4.8.4 NVSS angular two-point correlation

The estimated angular two-point correlation functions of NVSS (Condon et al., 1998) are shown in Figure 4.21 for “mask d” (left) and “mask n” (right). For angular separations $\theta < 0.4$ deg the angular two-point correlation varies strongly between the different flux density threshold samples of “mask d”. On these small angular scales, the correlation shows a clear dependence on the flux density threshold, with higher correlation for larger flux densities and vice versa. For larger angular separations, the correlation shows no clear flux density dependence and is consistent for all four flux density thresholds. Estimating the angular two-point correlation function for “mask n” results in much larger errors on the correlation and the power of the correlation varies more strongly than for “mask d”. For both masking samples, the correlation seems to follow a single power law, while for “mask n” the statement is complicated by the larger error bars. The results of the fitted power law of Equation (4.4) are presented in Table 4.2. In Figure 4.22 (left), the

4.8. ESTIMATING THE ANGULAR TWO-POINT CORRELATION FUNCTION FROM DIFFERENT SURVEYS

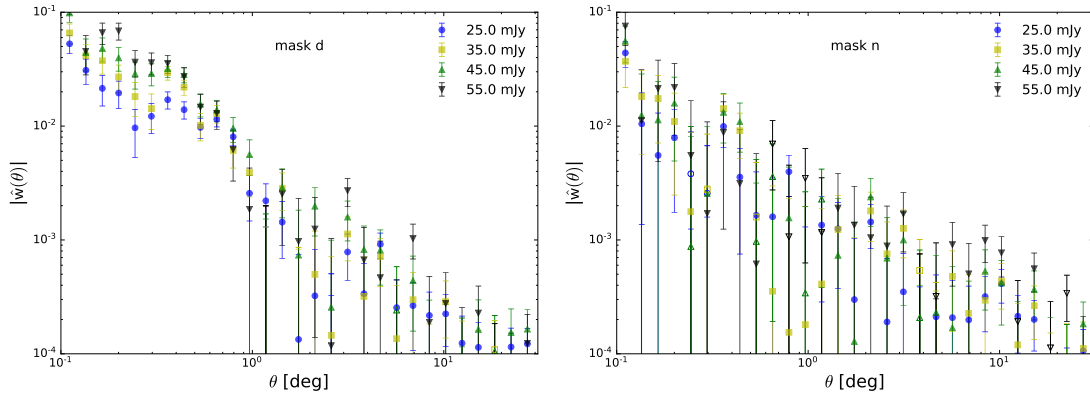


Figure 4.21: Estimated angular two-point correlation function of the NVSS with flux density thresholds of 25, 35, 45, and 55 mJy, masked with “mask d” (*left*) and “mask n” (*right*). Negative values are shown with open symbols.

fitted power laws for the 25 mJy samples are shown, together with the corresponding confidence regions (right). Showing only the estimates of the 25 mJy “mask d” samples in Figure 4.22 (left) reveals a varying angular two-point correlation function, which gives in terms of $\chi^2/\text{d.o.f.}$ a raise to a poorer fit of the power law. The resulting correlation amplitudes exceed the amplitudes found for WENSS and SUMSS, but are still two times smaller than for the TGSS-ADR1. Despite negative correlations (open symbols) for angular separations around $\theta \sim 0.3$ deg, the power law fit to the 25 mJy “mask n” sample gives significantly better results than for the 25 mJy “mask d” sample, with $\chi^2/\text{d.o.f.} = 1.32$ for $A = (1.29 \pm 0.53) \times 10^{-3}$, $\gamma = 0.799 \pm 0.553$ and $\chi^2/\text{d.o.f.} = 4.25$ for $A = (3.61 \pm 0.80) \times 10^{-3}$, $\gamma = 1.210 \pm 0.217$, respectively. Increasing the flux density threshold for “mask n” results in a vanishing correlation amplitude with strongly steepened slopes, like $A = (0.02 \pm 0.32) \times 10^{-3}$ and $\gamma = 4.354 \pm 11.628$ for 55 mJy. Taking a closer look at the confidence regions (see Fig. 4.22) of the 25 mJy “mask n” fit shows that the fit routine tends to higher slope values, which therefore can cause smaller correlation amplitudes.

In the literature, several estimates of the angular two-point correlation function for the NVSS are reported. Blake et al. (2004) commonly estimated the angular two-point correlation function for SUMSS, WENSS, and NVSS. Similar to Figure 4.22, they found a comparable deficit of pairs for angular separations of $0.1 < \theta < 0.3$ deg, which they explain as an artefact of the diffraction of the side lobes of the beam. Ignoring data points at $\theta \approx 0.2$ deg and fitting the power law only to angular separations of $\theta > 0.3$ deg for a flux density threshold of 10 mJy they found a correlation amplitude of $A = 1.49 \pm 0.15$ with a slope of $\gamma = 1.05 \pm 0.10$. For the same flux density threshold, but taking angular separations $\theta > 0.1$ deg into account, Blake and Wall (2002) estimated in an earlier study a smaller amplitude of $A = 1.08 \pm 0.09$ with a slope of 0.85 ± 0.1 . Redoing the fit for several flux density thresholds they found no signs of flux dependent correlation. Contrariwise to

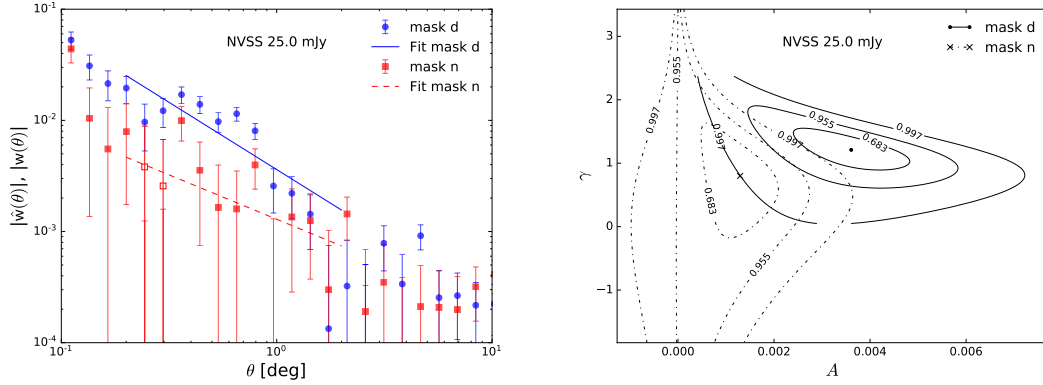


Figure 4.22: Angular two-point correlation of NVSS with 25 mJy flux density threshold and masked with “mask d” and “mask n” (*left*). Negative values are shown with open symbols. The data is fitted to a power law $w(\theta) = A\theta^{-\gamma}$ (*left*, lines) and the best-fit results are shown with 68%, 95%, and 99% confidence intervals (*right*) for both masks.

the deficit of pairs around $\theta \approx 0.2$ deg at low flux density thresholds, Overzier et al. (2003) found for a larger flux density threshold of 200 mJy an excess of sources. They also found a slight increasing correlation amplitude with increasing flux density thresholds. Fixing the slope in the fitting procedure to $\gamma = 0.8$, Overzier et al. (2003) found for a sample with 10 mJy flux density threshold and angular separations $\theta \geq 0.3$ deg a correlation amplitude of $A = 1.0 \pm 0.2$, which is in good agreement to the result of Blake and Wall (2002). At the same frequency of 1.4 GHz Overzier et al. (2003) investigated a source catalogue of FIRST (Helfand et al., 2015) from 2001 October 15. For flux densities below 10 mJy a consistent correlation amplitude between NVSS and FIRST was found. Above 10 mJy the estimated correlation amplitude of FIRST is found to be two times larger than for NVSS, with $A = (1.9 \pm 0.3) \times 10^{-3}$. The increased correlation amplitude can be explained by the increased resolution of FIRST, which results in more resolved multi-component sources and therefore in a lesser integrated flux density due to splitting sources into more components. Several other reported measurements of the angular two-point correlation function of FIRST catalogue are presented in Table 4.1. They all report a slight increased or similar correlation amplitude compared to results from NVSS. Comparing the new results of the NVSS 25 mJy “mask n” sample to these measurements shows a better agreement, than to the results reported for the NVSS. Resulting amplitudes of the other flux density threshold samples of “mask d” show a significantly increased value, which are not in agreement with previous findings. A possible reason for this discrepancy can be the range to which the power law is fitted, like previously mentioned, or the unmatching flux density thresholds. Additionally, at least two different versions of the NVSS catalogue are publicly available, which differ in the number of sources and the accuracy of the reported flux densities and positions.

Table 4.2: Resulting best-fit values of $w = A(\theta/1 \text{ deg})^{-\gamma}$ with 68% confidence intervals, fitted in the range $0.2 \leq \theta \leq 2.0 \text{ deg}$, for the TGSS-ADR1, WENSS, SUMSS, and NVSS

Survey	Mask	S (mJy)	N	A ($\times 10^3$)	γ	$\chi^2/\text{d.o.f.}$	BIC	AIC
TGSS	d	50	393 447	$15.25^{+0.40}_{-0.40}$	$0.477^{+0.042}_{-0.043}$	3.60	18.14	17.17
		100	244 881	$11.10^{+0.49}_{-0.49}$	$0.546^{+0.067}_{-0.069}$	2.08	11.57	10.60
		150	173 964	$11.67^{+0.49}_{-0.49}$	$0.511^{+0.066}_{-0.068}$	1.04	3.20	2.23
		200	133 547	$12.37^{+0.74}_{-0.74}$	$0.471^{+0.100}_{-0.105}$	1.40	6.83	5.86
	n	50	296 855	$9.09^{+0.44}_{-0.44}$	$0.593^{+0.071}_{-0.073}$	3.05	16.14	15.17
		100	179 951	$9.44^{+0.65}_{-0.65}$	$0.535^{+0.104}_{-0.109}$	2.54	13.97	13.00
		150	127 244	$10.44^{+0.71}_{-0.71}$	$0.427^{+0.113}_{-0.120}$	1.52	7.79	6.82
		200	97 355	$11.13^{+0.73}_{-0.73}$	$0.350^{+0.118}_{-0.126}$	0.95	2.23	1.26
WENSS	d	25	115 808	$3.47^{+0.36}_{-0.36}$	$0.937^{+0.122}_{-0.123}$	0.91	1.65	0.68
		35	95 302	$3.15^{+0.46}_{-0.46}$	$1.152^{+0.154}_{-0.151}$	1.01	2.91	1.94
		45	81 534	$3.17^{+0.80}_{-0.80}$	$1.131^{+0.267}_{-0.260}$	2.30	12.76	11.79
		55	71 643	$2.35^{+0.67}_{-0.67}$	$1.389^{+0.272}_{-0.249}$	1.29	5.80	4.83
	n	25	93 577	$3.22^{+0.36}_{-0.36}$	$0.982^{+0.128}_{-0.128}$	0.72	-1.15	-2.12
		35	76 760	$3.08^{+0.63}_{-0.63}$	$1.100^{+0.211}_{-0.206}$	1.53	7.89	6.92
		45	65 494	$2.98^{+0.98}_{-0.98}$	$1.033^{+0.353}_{-0.350}$	2.83	15.28	14.31
		55	57 463	$1.92^{+0.92}_{-0.87}$	$1.335^{+0.452}_{-0.397}$	2.05	11.41	10.44
SUMSS	d	25	75 642	$2.92^{+0.69}_{-0.68}$	$1.648^{+0.216}_{-0.190}$	1.32	6.10	5.13
		35	55 973	$3.51^{+0.86}_{-0.85}$	$1.600^{+0.230}_{-0.202}$	1.07	3.61	2.64
		45	44 403	$3.58^{+1.28}_{-1.25}$	$1.560^{+0.350}_{-0.295}$	1.53	7.87	6.91
		55	36 646	$3.41^{+1.12}_{-1.06}$	$1.833^{+0.283}_{-0.240}$	0.92	1.73	0.76
	n	25	73 356	$3.74^{+0.65}_{-0.64}$	$1.474^{+0.163}_{-0.151}$	1.13	4.26	3.29
		35	54 336	$4.09^{+0.97}_{-0.98}$	$1.434^{+0.240}_{-0.214}$	1.34	6.29	5.32
		45	43 121	$3.78^{+1.21}_{-1.19}$	$1.576^{+0.311}_{-0.264}$	1.32	6.12	5.15
		55	35 574	$3.37^{+1.33}_{-1.24}$	$1.794^{+0.349}_{-0.286}$	1.20	5.00	4.03
NVSS	d	25	209 034	$3.61^{+0.80}_{-0.79}$	$1.210^{+0.217}_{-0.207}$	4.25	20.14	19.17
		35	151 702	$4.12^{+1.11}_{-1.08}$	$1.362^{+0.252}_{-0.232}$	4.32	20.35	19.38
		45	117 617	$5.44^{+1.13}_{-1.11}$	$1.412^{+0.190}_{-0.177}$	2.67	14.56	13.59
		55	95 129	$4.48^{+0.96}_{-0.93}$	$1.719^{+0.181}_{-0.164}$	1.31	6.01	5.04
	n	25	156 331	$1.29^{+0.52}_{-0.53}$	$0.799^{+0.503}_{-0.553}$	1.32	6.14	5.17
		35	113 246	$0.76^{+0.73}_{-0.61}$	$1.557^{+1.129}_{0.755}$	1.23	5.31	4.34
		45	87 666	$0.35^{+0.72}_{-0.35}$	$2.261^{+2.417}_{-0.962}$	1.10	3.95	2.99
		55	70 777	$0.02^{+0.32}_{-0.02}$	$4.354^{+11.628}_{-2.010}$	0.76	-0.57	-1.54

Chapter 5

Summary and Conclusion

In this thesis the foundations of cosmology by means of different cosmological measurements have been discussed and tested with existing radio continuum surveys, as well as with simulated data. The work presented in this thesis can be grouped into three projects. Firstly, we measured in Section 2 for the first time the Cosmic Radio Dipole consistently from four independent radio surveys, namely the TGSS-ADR1, WENSS, SUMSS, and NVSS. Secondly, the Cosmic Radio Dipole was estimated in Section 3 for simulated number count maps, which are based on survey specifications of the upcoming SKA and the Λ CDM-model. Additionally, the clustering and distribution of radio sources was estimated in Section 4 for the LoTSS-DR1 and the four previous analysed radio surveys. The results of the angular correlation functions have been additionally compared to expectations, derived from numerical calculations based on the Λ CDM-model with best-fit cosmological parameters.

In order to measure the Cosmic Radio Dipole, we introduced a quadratic estimator in Bengaly et al. (2019) and Siewert et al. (2020b), which was tested against possible biases raising from the masking procedure and low number of sources. We find that the quadratic estimator can distinguish a dipole anisotropy of order of the CMB dipole from a purely random distribution of sources within absolute accuracies of 10^{-3} for simulated full skies with 10^7 sources. Furthermore, the dipole direction can be recovered within one degree to the simulated dipole direction. In general, the recovered dipole amplitudes, as well as dipole directions of the quadratic estimator are unbiased by the applied masks. However, in contrast to the quadratic estimator, we find a general directional bias of a linear estimator, which was used in previous studies.

Applying the quadratic estimator to the TGSS-ADR1, WENSS, SUMSS, and NVSS source catalogues, we find consistent dipole amplitudes and directions within each survey for two different masking strategies. The observed dipole amplitudes of all four surveys exceed the expected CMB dipole amplitude by factors of four to five times the CMB dipole amplitude at 1.4 GHz and of ten to 15 times at 150 MHz. However, the results of Siewert et al. (2020b) are in good agreement to results from the literature for the same surveys (e.g. Rubart and Schwarz 2013; Singal 2011; Singal 2019), while we estimate for the first time the Cosmic Radio Dipole consistently from all four surveys. Additionally,

the SUMSS source catalogue is used for the first time to estimate the Cosmic Radio Dipole. The excess still persist for a cross-matched sub-sample of the TGSS-ADR1 and NVSS source catalogues. We additionally find indications for a frequency dependent dipole amplitude, which contradicts the assumption of a purely kinematic dipole. Contributions to the dipole amplitude from local structures, like voids or clusters of galaxies, have already been discussed in the literature (Rubart et al., 2014), which would also show a frequency dependent contribution. In general, the contributions of these structures can relax the difference between the Radio and CMB dipole, but can not explain the large difference between the TGSS and NVSS dipole. Systematic effects, like a globular offset in the observed flux density scale of the TGSS-ADR1 (Tiwari et al., 2019), have been investigated by using a rescaled version of the TGSS catalogue (Hurley-Walker, 2017). The corresponding dipole measurements of the rescaled TGSS-ADR1 reveal a new dipole direction with comparable amplitudes, which are of unknown nature and not comparable with other contributions, like estimated bulk flows (e.g, Feldman et al. 2010; Hoffman et al. 2015). Based on a second fitting routine for the χ^2 -minimisation of the quadratic estimator, we tested the two hypothesis of having only a monopole for the source count distribution, or having an additional dipole modification to the source counts. We find, for the example of the NVSS source catalogue, that the source counts are significantly better described by a monopole with dipole modulation.

In order to distinguish further contributions, like local and large-scale structures, the quadratic estimator is used in Schwarz et al. (2018), Bengaly et al. (2019), and Square Kilometre Array Cosmology Science Working Group et al. (2020) to forecast possible measurements of the Cosmic Radio Dipole in terms of upcoming SKA surveys. These surveys will eventually observe the complete southern hemisphere at a central frequency of 700 MHz down to a realistic flux density threshold of 20 μ Jy. We find for simulated skies with SKA specifications, which include large-scale structures and a kinematic dipole, that local structures within redshifts of $z \leq 0.5$ can contribute to an increased dipole amplitude and change in the observed dipole direction. However, to be able to identify the local contributions with these larger and deeper surveys, additional redshift informations are necessary. Once upcoming surveys, like the LoTSS, will have large enough sky coverages and completed optical and/or infra-red follow up studies, which can be used to measure the redshift distribution of the sources, the different contributions to the Cosmic Radio Dipole can be ruled out.

In case of LoTSS, we have analysed in Siewert et al. (2020a) the two source catalogues of the first data release in terms of data quality as well as one and two-point source statistics. We derive a point-source completeness of 99% at 0.8 mJy for a set of 53 pointings of the LoTSS-DR1, while five pointings are in addition clearly under-sampled. By comparing the LoTSS-DR1 radio source and the value added source catalogue, we showed the significant improvement of identifying artefacts and matching multi-component sources, which was done for the value added catalogue. However, the general assumption of a Poisson-like source distribution seems unlikely, while the source count distribution of both catalogues are better described by a Compound Poisson distribution. Additionally, we measured the differential source counts and find good agreement to other existing

studies, as well as to simulated skies of SKADS and T-RECS (Siewert et al., 2020a; Mandal et al., 2020). Based on the previous findings, the angular two-point correlation is estimated for the full value added source catalogue and sub-samples with redshift information from optical and/or infra-red observations. We identify the 2 mJy “mask 1” sample to be the most reliable sample from the suite of flux density thresholds and masks. For a simple power-law fit of the angular two-point correlation function, we find for the 2 mJy “mask 1” sample at a pivot scale of 1 deg a correlation amplitude of $A = (5.11 \pm 0.60) \times 10^{-3}$ with a slope of $\gamma = 0.74 \pm 0.16$. In general we find the radio sky observed with the LoTSS-DR1 to be statistically isotropic at better than one percent for angular scales above one degree. Furthermore, the measured angular two-point correlation functions are compared to results from the literature, which have been observed at different frequencies (e.g. Blake and Wall 2002; Overzier et al. 2003; Rana and Bagla 2019), while we found no significant dependence of the correlation amplitude on the flux density threshold between these surveys (see Sect. 4.7). By comparing the measured angular two-point correlation functions of redshift sub-samples to expectations derived from Planck 2018 best-fit cosmology (Planck Collaboration et al., 2018a; Planck Collaboration et al., 2018b), we find good agreement on angular scales between 0.1 and 6 deg. A more detailed study of the angular two-point correlation function for redshift sub-samples revealed that we need larger sets of radio sources with improved measurements of the redshift distribution in order to measure cosmological parameters directly (see Sect. 4.5.4 and 4.6). However, Alonso et al. (2020) extended the analysis of Siewert et al. (2020a) and started to analyse the large-scale structures by cross correlating the LoTSS-DR1 value added catalogue to CMB lensing data. Additionally, they were able to constrain the linear bias of radio galaxies in the LoTSS-DR1 catalogue, as well as the amplitude of matter inhomogeneities σ_8 .

With future data release of LoTSS, the sky coverage and the total number of sources will significantly increase and already published sky fractions will be reprocessed for future data releases. For a second data release, the processing pipeline is improved and extended, which results in a significantly improved dynamic range. The next data release will cover in total ~ 5700 square degrees of the northern sky with roughly 4.5 million detected sources, which are splitted into two regions. It would be interesting to use these future data releases of LoTSS in order to make detailed measurements of cosmological parameters and a more detailed analysis of the large-scale structures.

We conclude that the origin of the Cosmic Radio Dipole can not completely be described by a kinematic effect. Possible contributions to the Cosmic Radio Dipole have to be distinguished by analysing upcoming radio surveys with additional redshift information and better sensitivity. Additionally, the spatial distribution of source counts does not follow a Poisson distribution and is better described with a Compound Poisson distribution. With existing surveys, we can conclude that for angular scales above one degree the radio sky is statistically isotropic at percent level and better. Furthermore, using the available redshift informations for the LoTSS-DR1 sources, the angular two-point correlation function agrees with expectations from recent best-fit cosmological models (Planck Collaboration et al., 2018a).

Acknowledgements

First of all, I want to thank my supervisor Prof. Dr. Dominik J. Schwarz, who guided my scientific education and research from my Bachelor thesis to this Dissertation. I thank him for all the opportunities in the various collaborations and the many schools and conferences I could attend with the help of him. It was a pleasure to present our work to the physics community and discuss it with international audiences.

I also want to thank the second referee Prof. Dr. Joris Verbiest and the other members of the examination committee for evaluating this thesis and their participation in the disputation.

I thank all members of the cosmology research group of Prof. Schwarz for the interesting group meetings and discussions. Especially, I want to thank Aritra Basu, who helped me with every question I had during the time of this thesis and Matthias Schmidt-Rubart for the fruitful collaboration. Also many thanks to my long time office maids, Dennis Schröder and Marc Klegrewe, for the quite amusing time on E6. I am also thankful to Gudrun Eickmeyer and Susi v. Reder for helping me with all the administrative things I encountered within the last years.

Special thanks to my parents and my girlfriend for supporting and encouraging me the whole time.

I acknowledge financial support from the Research Training Group 1620 “Models of Gravity”, supported by Deutsche Forschungsgemeinschaft (DFG) and support of the German Federal Ministry for Science and Research BMBF-Verbundforschungsprojekt D-LOFAR IV (grant number 05A17PBA).

This research made use of Astropy, a community-developed core Python package for astronomy (Astropy Collaboration et al., 2013) hosted at <http://www.astropy.org/>, and of the astropy-based reproject package (<http://reproject.readthedocs.io/en/stable/>). Some of the results in this paper have been derived using the healpy (Zonca et al., 2019) and HEALPix (Górski et al., 2005) package. This research made use of TOPCAT (Taylor, 2005), matplotlib (Hunter, 2007), NumPy (Walt et al., 2011), SciPy (Virtanen et al., 2020), lmfit (Newville et al., 2016), CAMB Sources (Challinor and Lewis, 2011) and TreeCorr (Jarvis et al., 2004).

Appendix

In this Appendix, the main computer programs, which have been used in this work are shown. The code of the Appendices A.1 and A.2 are written with python, while the modifications to the CAMB SOURCE code, which are presented in Appendix A.4, are written in fortran. In Appendix A.3 the main settings for the CAMB SOURCE code are shown.

A.1 Differential source counts

The following code was used in Siewert et al. (2020a) to calculate the differential source counts of a given survey, which will be masked by a pre-defined HEALPIX mask. Additional criteria, like a redshift limit can be included in the binning procedure from line 56 to 64.

```

1 # -*- coding: utf-8 -*-
2 import healpy as hp
3 import numpy as np
4 import matplotlib.pyplot as plt
5 from astropy.io import fits
6
7 def main():
8
9     hdulist = fits.open('<Catalogue File>.fits')
10    tldata = hdulist[1].data
11    RA = tldata['RA']
12    DEC = tldata['DEC']
13    FLUX = tldata['total_flux']
14    hdulist.close()
15
16    if len(FLUX) == len(RA) and len(FLUX) == len(DEC):
17        numbsources = len(FLUX)
18    else:
19        print('Error while read in')
20
21 # Mask handling
22 file_mask = '<Mask File in HEALPix format>.fits'
23 mask = hp.read_map(file_mask)
24 NSide = hp.get_nside(mask)
25 NPIX = hp.nside2npix(NSide)
26

```

```

27 # Counting unmasked pixels
28     unmasked = 0
29     for i in range(NPIX):
30         if mask[i] != 0:
31             unmasked += 1
32
33 # Sky coverage
34     coverage = 4 * np.pi * unmasked / NPIX
35
36 # Masing the survey
37     survey = []
38     i = 0
39     for i in range(0,numbsources):
40         # Convert Declination from deg to rad with convention [0,pi]
41         theta=(90.-DEC[i])/180.*np.pi
42         # Convert Right Ascension from deg to rad
43         phi=RA[i]/180.*np.pi
44         b=hp.ang2pix(NSide,theta,phi)
45         if mask[b]==1:
46             survey.append(FLUX[i])
47
48 #Binning of the data into bins with equal step width in log10
49     Numb_bins = 33
50     log_step_width =
51     ↪ (np.log10(upper_flux)-np.log10(lower_flux))/float(Numb_bins)
52     file_out = '<File Results>'
53     fout = open(file_out, 'w')
54     lower_flux = 0.1      # in mJy
55     upper_flux = 10000   # in mJy
56     i=0
57     xlow = lower_flux
58     xup = 0
59     while xlow <= upper_flux:
60         survey_del = []
61         if len(survey)!=0:
62             xup = xlow*pow(10,log_step_width)
63             xmid = xlow*pow(10,log_step_width/2.)
64             for s in range(len(survey)):
65                 if float(xlow) <= float(survey[s]) < (float(xup)):
66                     i += 1
67                     survey_del.append(s)
68             else:
69                 break
70             survey = np.delete(survey, survey_del)
71             del survey_del
72 # Report only non-null bins and calculate differential source counts
73     if i != 0:
74         N = i
75         N_A = np.power(xmid/1000.,5./2)*i /
76         ↪ (coverage*(xup-xlow)/1000.) # i/(coverage*(xup-xlow))#
77         error =np.power(xmid/1000.,5./2)*np.sqrt(i) /
78         ↪ (coverage*(xup-xlow)/1000.)#np.sqrt(i) / (coverage*(xup-xlow)) #

```



```

77         fout.write(str(xmid/1000.)+' '+str(coverage) +'
↪ '+str(N)+' '+str(N_A)+' '+str(error)+'\n')
78         i = 0
79         xlow = xup
80         fout.close()
81 main()

```

A.2 Angular two-point correlation

This code computes the angular two-point correlation function for a given set of data points of the angular power spectrum C_l and multipoles l . From line 25 to 31 the given range of multipoles is extended by extrapolating the given angular power spectrum with a fit of the form $C_l^{fit} \propto l^\beta$. If this is not wanted, the script can be changed accordingly to just use the given angular power spectrum.

```

1 # -*- coding: utf-8 -*-
2 from astropy.io import fits
3 import matplotlib.pyplot as plt
4 import scipy.special as scp
5 import numpy as np
6 import math as m
7 plt.style.use('classic')
8
9 # Read in power spectrum file
10 file_windowsource = './<File Power Spectrum>.fits'
11 hdulist = fits.open(file_windowsource)
12 tbdata = hdulist[1].data
13 ls = tbdata['l'].astype(np.float64)
14 cl = tbdata['C_l'].astype(np.float64)
15
16 # Define grid of angular separations
17 theta = np.arange(0.1, 32., 0.05)
18 wtheta = np.zeros(len(theta))
19
20 # The extension  $C_l^{fit} \propto l^\beta$  is fitted to the last two  $C_l$ 's
21 beta =
↪ (m.log10(cl[-2]) - m.log10(cl[-1])) / (m.log10(ls[-2]) - m.log10(ls[-1]))
22 ampl = cl[-1]
23
24 # Extrapolating the array of  $C_l$ 's up to  $l = 60000$ 
25 ls_extend = np.append(ls, np.arange(np.max(ls)+1, 60001, dtype = int))
26 cl_extend = np.append(cl, ampl*np.power(np.arange(np.max(ls)+1, 60001)
↪ ,beta)/np.power(ls[-1], beta))
27
28 # Using scipy's legendre polynomials to calculate the two-point
↪ correlation
29 cos_theta = np.cos(np.radians(theta), dtype = np.float)
30 d = 2
31 while d <= len(ls_extend):
32     wtheta += (2*ls_extend[d-2]+1)*cl_extend[d-2]
↪ *scp.eval_legendre(int(ls_extend[d-2]), cos_theta)

```

```

33     print(d)
34     d+=1
35 wtheta = wtheta/(4*np.pi)
36
37 save_path= './<File results>'
38 # Plotting the resulting angular two-point correlation
39 plt.xlim(0.1, 32.)
40 plt.xlabel(r' $\theta$ ', fontsize = 18)
41 plt.ylabel(r' $w(\theta)$ ', fontsize = 18)
42 plt.loglog(theta, wtheta, basex= 10, basey = 10, ls = '-', color = 'k')
43 plt.savefig(save_path + '.pdf', format = 'pdf')
44
45 # Saving the resulting angular two-point correlation to file
46 hdu = fits.BinTableHDU.from_columns([fits.Column(name='theta', format =
    ↪ 'E', array=theta), fits.Column(name='wtheta', format = 'E', array
    ↪ = wtheta)])
47 hdu.writeto(save_path + '.fits')

```

A.3 Settings of CAMB SOURCES

In the following all necessary settings of CAMB SOURCES are shown with their values, which have been used in Siewert et al. (2020a) and this thesis. More detailed values, like window function and flux density threshold are for the example of the 1 mJy sample of the LoTSS-DR1 value added source catalogue, masked with 'mask z'. Additionally in this case the halo-fit option and the galaxy bias of Nusser and Tiwari (2015) are used. The details on how to include the modified galaxy bias are presented in Appendix A.4.

```

1 output_file:
2 Cl1.0_halofit-Tiwari_4000
3 path:
4 ./tmp/
5 window source function:
6 ./window1.0mJytotal.fits
7 flux density threshold: 1.000000
    ↪ mJy
8 parameters: class: <CAMBparams>
9 WantCls = True
10 WantTransfer = True
11 WantScalars = True
12 WantTensors = False
13 WantVectors = False
14 WantDerivedParameters = True
15 Want_cl_2D_array = True
16 Want_CMB = True
17 Want_CMB_lensing = True
18 DoLensing = True
19 NonLinear = NonLinear_both
20 Transfer: <TransferParams>
21     high_precision = True
22     accurate_massive_neutrinos =
    ↪ False
23     kmax = 1.3464234
24     k_per_logint = 0
25     PK_num_redshifts = 1
26     PK_redshifts = [0.0]
27     want_zstar = False
28     want_zdrag = False
29     min_l = 2
30     max_l = 4150
31     max_l_tensor = 600
32     max_eta_k = 18000.0
33     max_eta_k_tensor = 1200.0
34     ombh2 = 0.0223828
35     omch2 = 0.1201075
36     omk = 0.0
37     omnuh2 = 0.0006451439
38     H0 = 67.32117
39     TCMB = 2.7255
40     YHe = 0.2454006
41     num_nu_massless = 2.046
42     num_nu_massive = 1
43     nu_mass_eigenstates = 1

```

A.3. SETTINGS OF CAMB SOURCES

```

44 share_delta_neff = True
45 nu_mass_degeneracies = [0.0]
46 nu_mass_fractions = [1.0]
47 nu_mass_numbers = [1]
48 InitPower: <InitialPowerLaw>
49   tensor_parameterization =
50     ↪ tensor_param_indeptilt
51   ns = 0.9660499
52   nrun = 0.0
53   nrunrun = 0.0
54   nt = 0.0
55   ntrun = 0.0
56   r = 0.0
57   pivot_scalar = 0.05
58   pivot_tensor = 0.05
59   As = 2.100549e-09
60   At = 0.0
61 Recomb: <Recfast>
62   min_a_evolve_Tm =
63     ↪ 0.00110987795051
64   RECFAST_fudge = 1.125
65   RECFAST_fudge_He = 0.86
66   RECFAST_Heswitch = 6
67   RECFAST_Hswitch = True
68   AGauss1 = -0.14
69   AGauss2 = 0.079
70   zGauss1 = 7.28
71   zGauss2 = 6.73
72   wGauss1 = 0.18
73   wGauss2 = 0.33
74 Reion: <TanhReionization>
75   Reionization = True
76   use_optical_depth = True
77   redshift = 10.0
78   optical_depth = 0.05430842
79   delta_redshift = 0.5
80   fraction = -1.0
81   include_helium_fullreion = True
82   helium_redshift = 3.5
83   helium_delta_redshift = 0.5
84   helium_redshiftstart = 6.0
85   tau_solve_accuracy_boost = 1.0
86   timestep_boost = 1.0
87   max_redshift = 50.0
88 DarkEnergy: <DarkEnergyPPF>
89   w = -1.0
90   wa = 0.0
91   cs2 = 1.0
92   use_tabulated_w = False
93 NonLinearModel: <Halofit>
94   Min_kh_nonlinear = 0.005
95   halofit_version = mead
96 Accuracy: <AccuracyParams>
97   AccuracyBoost = 1.0
98   lSampleBoost = 1.0
99   lAccuracyBoost = 1.0
100   AccuratePolarization = True
101   AccurateBB = False
102   AccurateReionization = True
103   TimeStepBoost = 1.0
104   BackgroundTimeStepBoost = 1.0
105   IntTolBoost = 1.0
106   SourcekAccuracyBoost = 1.0
107   IntkAccuracyBoost = 1.0
108   TransferkBoost = 1.0
109   NonFlatIntAccuracyBoost = 1.0
110   BessIntBoost = 1.0
111   LensingBoost = 1.0
112   NonlinSourceBoost = 1.0
113   BesselBoost = 1.0
114   LimberBoost = 1.0
115   SourceLimberBoost = 1.0
116   KmaxBoost = 1.0
117   neutrino_q_boost = 1.0
118 SourceTerms: <SourceTermParams>
119   limber_windows = False
120   limber_phi_lmin = 100
121   counts_density = True
122   counts_redshift = True
123   counts_lensing = True
124   counts_velocity = True
125   counts_radial = False
126   counts_timedelay = True
127   counts_ISW = True
128   counts_potential = True
129   counts_evolve = False
130   line_phot_dipole = False
131   line_phot_quadrupole = False
132   line_basic = True
133   line_distortions = True
134   line_extra = False
135   line_reionization = False
136   use_21cm_mK = True
137 z_outputs = []
138 scalar_initial_condition =
139   ↪ initial_adiabatic
140 InitialConditionVector = []
141 OutputNormalization = 1
142 Alens = 1.0
143 MassiveNuMethod = Nu_trunc
144 DoLateRadTruncation = True
145 Evolve_baryon_cs = False
146 Evolve_delta_xe = False
147 Evolve_delta_Ts = False
148 Do21cm = False
149 transfer_21cm_cl = False

```

```

147 Log_lvalues = False
148 use_cl_spline_template = True
149 SourceWindows:
    ↪ <SourceWindowArray_1>
150 0: <SplinedSourceWindow>
151     source_type = counts
152     bias = 1.0
153     dlog10Ndm = -0.2
154 CustomSources: <CustomSources>
155     num_custom_sources = 0
156     c_source_func = None
157     custom_source_ell_scales = []

```

A.4 Bias Modification

The source code of CAMB SOURCES¹ (Challinor and Lewis, 2011) has been modified to account for the galaxy bias $b(z) = 1.6 + 0.85z + 0.33z^2$ of Nusser and Tiwari (2015). The modification has been applied to the fortran source code file `equations.f90` in the subroutine `output_window_sources`. In the following, the modification is shown, while the bias is calculated in line 17 and is passed in line 18. Not modified code is abbreviated with [...].

```

1  subroutine output_window_sources(...)
2  [...]
3  real(dl) biasG
4  [...]
5
6  do w_ix = 1, State%num_redshiftwindows
7      associate (W => State%Redshift_W(w_ix))
8
9          if (W%kind == window_lensing) then
10             sources(3+w_ix) = -2*phi*W%win_lens(j)
11         elseif (W%kind == window_counts) then
12             !assume zero velocity bias and relevant tracer is CDM perturbation
13             !neglect anisotropic stress in some places
14             !Main density source
15             if (CP%SourceTerms%counts_density) then
16
17                 biasG = 1.6+0.85*(1./a-1.)+0.33*(1./a-1.)**2.
18                 counts_density_source= W%wing(j)*(clxc*biasG +
19                 ↪ (W%comoving_density_ev(j) - 3*adotoa)*sigma/k)
20             !Newtonian gauge count density; bias assumed to be on synchronous gauge
21             ↪ CDM density
22             else
23                 counts_density_source= 0
24             endif
25         [...]

```

¹<https://github.com/cmbant/CAMB>

Bibliography

- Airy, G. B. (1835). “On the Diffraction of an Object-glass with Circular Aperture”. In: *Transactions of the Cambridge Philosophical Society* 5, p. 283.
- Alonso, David et al. (2015). “Ultra-large-scale Cosmology in Next-generation Experiments with Single Tracers”. In: *Astrophys. J.* 814.2, 145, p. 145. DOI: 10.1088/0004-637X/814/2/145. arXiv: 1505.07596 [astro-ph.CO].
- Alonso, David et al. (2020). “Cross-correlating radio continuum surveys and CMB lensing: constraining redshift distributions, galaxy bias and cosmology”. In: *arXiv e-prints*, arXiv:2009.01817, arXiv:2009.01817. arXiv: 2009.01817 [astro-ph.CO].
- Astropy Collaboration et al. (2013). “Astropy: A community Python package for astronomy”. In: *Astron. Astrophys.* 558, A33, A33. DOI: 10.1051/0004-6361/201322068. arXiv: 1307.6212 [astro-ph.IM].
- Barthel, Peter D. (1989). “Is Every Quasar Beamed?” In: *Astrophys. J.* 336, p. 606. DOI: 10.1086/167038.
- Becker, Robert H., Richard L. White, and David J. Helfand (1995). “The FIRST Survey: Faint Images of the Radio Sky at Twenty Centimeters”. In: *Astrophys. J.* 450, p. 559. DOI: 10.1086/176166.
- Beijing Observatory Metre-Wave Radio Astronomy Group (1986). “Miyun metre-wave aperture synthesis radio telescope”. In: *Chin. Astron. and Astrophys.* 10.1, pp. 3–11. DOI: 10.1016/0275-1062(86)90048-2.
- Bengaly, C. A. P. et al. (2019). “Testing the standard model of cosmology with the SKA: the cosmic radio dipole”. In: *Mon. Not. R. Astron. Soc.* 486.1, pp. 1350–1357. DOI: 10.1093/mnras/stz832. arXiv: 1810.04960 [astro-ph.CO].
- Bengaly, Carlos A. P., Roy Maartens, and Mario G. Santos (2018). “Probing the Cosmological Principle in the counts of radio galaxies at different frequencies”. In: *J. Cosmol. Astropart. Phys.* 2018.4, 031, p. 031. DOI: 10.1088/1475-7516/2018/04/031. arXiv: 1710.08804 [astro-ph.CO].
- Bennett, C. L. et al. (1996). “Four-Year COBE DMR Cosmic Microwave Background Observations: Maps and Basic Results”. In: *Astrophys. J. Let.* 464, p. L1. DOI: 10.1086/310075. arXiv: astro-ph/9601067 [astro-ph].
- Biermann, Marian (2019). “A Detailed Look at Estimators for the Two-Point Correlation Function, their Variance and a Verification of the TreeCorr-Algorithm with LoTSS Data”. MA thesis. Bielefeld, Germany: Bielefeld University.

BIBLIOGRAPHY

- Blake, C. and J. Wall (2002). “Quantifying angular clustering in wide-area radio surveys”. In: *Mon. Not. R. Astron. Soc.* 337, pp. 993–1003. DOI: 10.1046/j.1365-8711.2002.05979.x. eprint: astro-ph/0208350.
- Blake, Chris, Tom Mauch, and Elaine M. Sadler (2004). “Angular clustering in the Sydney University Molonglo Sky Survey”. In: *Mon. Not. R. Astron. Soc.* 347.3, pp. 787–794. DOI: 10.1111/j.1365-2966.2004.07240.x. arXiv: astro-ph/0310115 [astro-ph].
- Bonaldi, Anna et al. (2019). “The Tiered Radio Extragalactic Continuum Simulation (T-RECS)”. In: *Mon. Not. R. Astron. Soc.* 482.1, pp. 2–19. DOI: 10.1093/mnras/sty2603. arXiv: 1805.05222 [astro-ph.GA].
- Bonzini, M. et al. (2013). “The sub-mJy radio sky in the Extended Chandra Deep Field-South: source population”. In: *Mon. Not. R. Astron. Soc.* 436.4, pp. 3759–3771. DOI: 10.1093/mnras/stt1879. arXiv: 1310.1248 [astro-ph.CO].
- Burke, Bernard F., Francis Graham-Smith, and Peter N. Wilkinson (2019). *An Introduction to Radio Astronomy*. eng. 4th ed. Cambridge: Cambridge University Press, 1 Online-Resource (540 pages). ISBN: 978-1-316-98750-6, 1-316-98750-7. URL: <https://doi.org/10.1017/9781316987506>.
- Challinor, Anthony and Antony Lewis (2011). “Linear power spectrum of observed source number counts”. In: *Phys. Rev. D* 84.4, 043516, p. 043516. DOI: 10.1103/PhysRevD.84.043516. arXiv: 1105.5292 [astro-ph.CO].
- Chisari, Nora Elisa et al. (2019). “Core Cosmology Library: Precision Cosmological Predictions for LSST”. In: *ApJS* 242.1, 2, p. 2. DOI: 10.3847/1538-4365/ab1658. arXiv: 1812.05995 [astro-ph.CO].
- Cohen, A. S. et al. (2007). “The VLA Low-Frequency Sky Survey”. In: *Astron.J.* 134.3, pp. 1245–1262. DOI: 10.1086/520719. arXiv: 0706.1191 [astro-ph].
- Condon, J. J. (1992). “Radio emission from normal galaxies.” In: *ARA&A* 30, pp. 575–611. DOI: 10.1146/annurev.aa.30.090192.003043.
- Condon, J. J. and M. Harwit (1968). “Means of Measuring the Earth’s Velocity Through the 3° Radiation Field”. In: *Phys. Rev. Lett.* 20 (23), pp. 1309–1310. DOI: 10.1103/PhysRevLett.20.1309. URL: <https://link.aps.org/doi/10.1103/PhysRevLett.20.1309>.
- Condon, J. J., J. J. Broderick, and G. A. Seielstad (1989). “A 4.85 GHz Sky Survey. I. Maps Covering 0 Degrees δ +75 Degrees”. In: *Astron.J.* 97, p. 1064. DOI: 10.1086/115049.
- Condon, J. J., Mark R. Griffith, and Alan E. Wright (1993). “The Parkes-MIT-NRAO Surveys. IV. Maps for the Southern Survey Covering -88degrees δ -37degrees”. In: *Astron.J.* 106, p. 1095. DOI: 10.1086/116707.
- Condon, J. J. et al. (1994). “A 4.85 GHz Sky Survey. III. Epoch 1986 and Combined (1986-1987) Maps Covering 0degrees δ +75degrees”. In: *Astron.J.* 107, p. 1829. DOI: 10.1086/116992.
- Condon, J. J. et al. (1998). “The NRAO VLA Sky Survey”. In: *Astron.J.* 115.5, pp. 1693–1716. DOI: 10.1086/300337.
- Conklin, E. K. (1969). “Velocity of the Earth with Respect to the Cosmic Background Radiation”. In: *Nature* 222.5197, pp. 971–972. DOI: 10.1038/222971a0.

- Cordes, J. M. and T. J. W. Lazio (2002). “NE2001.I. A New Model for the Galactic Distribution of Free Electrons and its Fluctuations”. In: *arXiv Astrophysics e-prints*. eprint: astro-ph/0207156.
- Crawford, F. (2009). “Detecting the Cosmic Dipole Anisotropy in Large-Scale Radio Surveys”. In: *Astrophysical Journal* 692, pp. 887–893. DOI: 10.1088/0004-637X/692/1/887. arXiv: 0810.4520.
- Cress, Catherine M. et al. (1996). “The Angular Two-Point Correlation Function for the FIRST Radio Survey”. In: *Astrophys. J.* 473, p. 7. DOI: 10.1086/178122. arXiv: astro-ph/9606176 [astro-ph].
- de Bruyn, G. et al. (2000). “VizieR Online Data Catalog: The Westerbork Northern Sky Survey (Leiden, 1998)”. In: *VizieR Online Data Catalog*, VIII/62, pp. VIII/62.
- de Gasperin, F., H. T. Intema, and D. A. Frail (2018). “A radio spectral index map and catalogue at 147–1400 MHz covering 80 per cent of the sky”. In: *Mon. Not. R. Astron. Soc.* 474.4, pp. 5008–5022. DOI: 10.1093/mnras/stx3125. arXiv: 1711.11367 [astro-ph.IM].
- de Oliveira-Costa, Angélica and John Capodilupo (2010). “Clustering at 74MHz”. In: *Mon. Not. R. Astron. Soc.* 404.4, pp. 1962–1965. DOI: 10.1111/j.1365-2966.2010.16412.x. arXiv: 0908.4248 [astro-ph.CO].
- de Oliveira-Costa, Angelica and Joseph Lazio (2010). “Clustering of Extragalactic Sources from 151 MHz to 232 MHz: Implications for Cosmological 21-cm Observations”. In: *arXiv e-prints*, arXiv:1004.3167, arXiv:1004.3167. arXiv: 1004.3167 [astro-ph.CO].
- Dicke, R. H. et al. (1965). “Cosmic Black-Body Radiation.” In: *Astrophys. J.* 142, pp. 414–419. DOI: 10.1086/148306.
- Dolfi, Arianna et al. (2019). “Clustering properties of TGSS radio sources”. In: *Astron. Astrophys.* 623, A148, A148. DOI: 10.1051/0004-6361/201834317. arXiv: 1901.08357 [astro-ph.CO].
- Duncan, K. J. et al. (2019). “The LOFAR Two-metre Sky Survey. IV. First Data Release: Photometric redshifts and rest-frame magnitudes”. In: *Astron. Astrophys.* 622, A3, A3. DOI: 10.1051/0004-6361/201833562. arXiv: 1811.07928 [astro-ph.GA].
- Ellis, G. F. R. and J. E. Baldwin (1984). “On the expected anisotropy of radio source counts”. In: *Mon. Not. R. Astron. Soc.* 206, pp. 377–381. DOI: 10.1093/mnras/206.2.377.
- Fanaroff, B. L. and J. M. Riley (1974). “The morphology of extragalactic radio sources of high and low luminosity”. In: *Mon. Not. R. Astron. Soc.* 167, 31P–36P. DOI: 10.1093/mnras/167.1.31P.
- Feldman, Hume A., Richard Watkins, and Michael J. Hudson (2010). “Cosmic flows on 100 h⁻¹ Mpc scales: standardized minimum variance bulk flow, shear and octupole moments”. In: *Mon. Not. R. Astron. Soc.* 407.4, pp. 2328–2338. DOI: 10.1111/j.1365-2966.2010.17052.x. arXiv: 0911.5516 [astro-ph.CO].
- Fixsen, D. J. (2009). “THE TEMPERATURE OF THE COSMIC MICROWAVE BACKGROUND”. In: *Astrophys. J.* 707.2, pp. 916–920. DOI: 10.1088/0004-637x/707/2/916. URL: <https://doi.org/10.1088/0004-637x/707/2/916>.

- Fixsen, D. J. et al. (1994). “Cosmic Microwave Background Dipole Spectrum Measured by the COBE FIRAS Instrument”. In: *Astrophys. J.* 420, p. 445. DOI: 10.1086/173575.
- Franzen, T. M. O. et al. (2016). “The 154 MHz radio sky observed by the Murchison Widefield Array: noise, confusion, and first source count analyses”. In: *Mon. Not. R. Astron. Soc.* 459, pp. 3314–3325. DOI: 10.1093/mnras/stw823. arXiv: 1604.03751 [astro-ph.IM].
- Garofalo, David and Chandra B. Singh (2019). “FR0 Radio Galaxies and Their Place in the Radio Morphology Classification”. In: *Astrophys. J.* 871.2, 259, p. 259. DOI: 10.3847/1538-4357/aaf056. arXiv: 1811.05383 [astro-ph.HE].
- Ghisellini, Gabriele (2011). “Extragalactic relativistic jets”. In: *American Institute of Physics Conference Series*. Ed. by Felix A. Aharonian, Werner Hofmann, and Frank M. Rieger. Vol. 1381. American Institute of Physics Conference Series, pp. 180–198. DOI: 10.1063/1.3635832. arXiv: 1104.0006 [astro-ph.CO].
- Gibelyou, Cameron and Dragan Huterer (2012). “Dipoles in the sky”. In: *Mon. Not. R. Astron. Soc.* 427.3, pp. 1994–2021. DOI: 10.1111/j.1365-2966.2012.22032.x. arXiv: 1205.6476 [astro-ph.CO].
- Górski, K. M. et al. (2005). “HEALPix: A Framework for High-Resolution Discretization and Fast Analysis of Data Distributed on the Sphere”. In: *Astrophys. J.* 622, pp. 759–771. DOI: 10.1086/427976.
- Gregory, P. C. and J. J. Condon (1991). “The 87GB Catalog of Radio Sources Covering 0 degrees δ +75 degrees at 4.85 GHz”. In: *ApJS* 75, p. 1011. DOI: 10.1086/191559.
- Gregory, P. C. et al. (1996). “The GB6 Catalog of Radio Sources”. In: *ApJS* 103, p. 427. DOI: 10.1086/192282.
- Griffith, Mark R. and Alan E. Wright (1993). “The Parkes-MIT-NRAO (PMN) Survey. I. The 1450 MHz Surveys and Data Reduction”. In: *Astron. J.* 105, p. 1666. DOI: 10.1086/116545.
- Griffith, Mark R. et al. (1994). “The Parkes-MIT-NRAO (PMN) Surveys. III. Source Catalog for the Tropical Survey (-29 degrees δ -9 degrees -3pt.5)”. In: *ApJS* 90, p. 179. DOI: 10.1086/191863.
- (1995). “The Parkes-MIT-NRAO (PMN) Surveys. VI. Source Catalog for the Equatorial Survey (-9.5 degrees δ +10.0 degrees)”. In: *ApJS* 97, p. 347. DOI: 10.1086/192146.
- Hamilton, A. J. S. (1993). “Toward Better Ways to Measure the Galaxy Correlation Function”. In: *Astrophys. J.* 417, p. 19. DOI: 10.1086/173288.
- Haslam, C. G. T. et al. (1981). “A 408 MHz all-sky continuum survey. I - Observations at southern declinations and for the North Polar region.” In: *Astron. Astrophys.* 100, pp. 209–219.
- Haslam, C. G. T. et al. (1982). “A 408 MHz all-sky continuum survey. II. The atlas of contour maps.” In: *Astron. Astrophys., Sup.* 47, pp. 1–143.
- Helfand, David J., Richard L. White, and Robert H. Becker (2015). “The Last of FIRST: The Final Catalog and Source Identifications”. In: *Astrophys. J.* 801.1, 26, p. 26. DOI: 10.1088/0004-637X/801/1/26. arXiv: 1501.01555 [astro-ph.GA].

- Henry, Paul S. (1971). “Isotropy of the 3 K Background”. In: *Nature* 231.5304, pp. 516–518. DOI: 10.1038/231516a0.
- Hoffman, Yehuda, Hélène M. Courtois, and R. Brent Tully (2015). “Cosmic bulk flow and the local motion from Cosmicflows-2”. In: *Mon. Not. R. Astron. Soc.* 449.4, pp. 4494–4505. DOI: 10.1093/mnras/stv615. arXiv: 1503.05422 [astro-ph.CO].
- Hubble, E. P. (1926). “Extragalactic nebulae.” In: *Astrophys. J.* 64, pp. 321–369. DOI: 10.1086/143018.
- Hunter, J. D. (2007). “Matplotlib: A 2D graphics environment”. In: *Computing in Science & Engineering* 9.3, pp. 90–95. DOI: 10.1109/MCSE.2007.55.
- Hurley-Walker, N. et al. (2017). “GaLactic and Extragalactic All-sky Murchison Widefield Array (GLEAM) survey - I. A low-frequency extragalactic catalogue”. In: *Mon. Not. R. Astron. Soc.* 464.1, pp. 1146–1167. DOI: 10.1093/mnras/stw2337. arXiv: 1610.08318 [astro-ph.GA].
- Hurley-Walker, Natasha (2017). “A Rescaled Subset of the Alternative Data Release 1 of the TIFR GMRT Sky Survey”. In: *arXiv e-prints*, arXiv:1703.06635, arXiv:1703.06635. arXiv: 1703.06635 [astro-ph.IM].
- Intema, H. T. et al. (2017). “The GMRT 150 MHz all-sky radio survey. First alternative data release TGSS ADR1”. In: *Astron. Astrophys.* 598, A78, A78. DOI: 10.1051/0004-6361/201628536. arXiv: 1603.04368 [astro-ph.CO].
- Jarvis, M., G. Bernstein, and B. Jain (2004). “The skewness of the aperture mass statistic”. In: *Mon. Not. R. Astron. Soc.* 352, pp. 338–352. DOI: 10.1111/j.1365-2966.2004.07926.x. eprint: astro-ph/0307393.
- Kaiser, Nicholas et al. (2002). “Pan-STARRS: A Large Synoptic Survey Telescope Array”. In: *Survey and Other Telescope Technologies and Discoveries*. Ed. by J. Anthony Tyson and Sidney Wolff. Vol. 4836. Society of Photo-Optical Instrumentation Engineers (SPIE) Conference Series, pp. 154–164. DOI: 10.1117/12.457365.
- Kaiser, Nick et al. (2010). “The Pan-STARRS wide-field optical/NIR imaging survey”. In: *Ground-based and Airborne Telescopes III*. Ed. by Larry M. Stepp, Roberto Gilmozzi, and Helen J. Hall. Vol. 7733. Society of Photo-Optical Instrumentation Engineers (SPIE) Conference Series, 77330E. DOI: 10.1117/12.859188.
- Kassim, N. E. et al. (1993). “Subarcminute Resolution Imaging of Radio Sources at 74 MHz With the Very Large Array”. In: *Astron. J.* 106, p. 2218. DOI: 10.1086/116795.
- Kassim, N. E. et al. (2007). “The 74 MHz System on the Very Large Array”. In: *ApJS* 172.2, pp. 686–719. DOI: 10.1086/519022. arXiv: 0704.3088 [astro-ph].
- Kennicutt, Robert C. and Neal J. Evans (2012). “Star Formation in the Milky Way and Nearby Galaxies”. In: *ARA&A* 50, pp. 531–608. DOI: 10.1146/annurev-astro-081811-125610. arXiv: 1204.3552 [astro-ph.GA].
- Kingman J. F. C., 1939 (2010). *Poisson processes*. eng. Reprinted, [Nachdr.] Vol. 3. Oxford studies in probability ; 3. Oxford: Clarendon Press, VIII, 104 S. : graph. Darst. ISBN: 0-19-853693-3.
- Landy, S. D. and A. S. Szalay (1993). “Bias and variance of angular correlation functions”. In: *Astrophys. J.* 412, pp. 64–71. DOI: 10.1086/172900.

- Limber, D. N. (1953). “The Analysis of Counts of the Extragalactic Nebulae in Terms of a Fluctuating Density Field.” In: *Astrophys. J.* 117, p. 134. DOI: 10.1086/145672.
- Loan, A. J., J. V. Wall, and O. Lahav (1997). “The correlation function of radio sources”. In: *Mon. Not. R. Astron. Soc.* 286.4, pp. 994–1002. DOI: 10.1093/mnras/286.4.994. arXiv: astro-ph/9612190 [astro-ph].
- Lonsdale, C. J. et al. (2009). “The Murchison Widefield Array: Design Overview”. In: *IEEE Proceedings* 97.8, pp. 1497–1506. DOI: 10.1109/JPROC.2009.2017564. arXiv: 0903.1828 [astro-ph.IM].
- Maddox, S. J., G. Efstathiou, and W. J. Sutherland (1996). “The APM Galaxy Survey - III. an analysis of systematic errors in the angular correlation function and cosmological implications”. In: *Mon. Not. R. Astron. Soc.* 283.4, pp. 1227–1263. DOI: 10.1093/mnras/283.4.1227. arXiv: astro-ph/9601103 [astro-ph].
- Magliocchetti, M. et al. (1998). “Variance and skewness in the FIRST survey”. In: *Mon. Not. R. Astron. Soc.* 300.1, pp. 257–268. DOI: 10.1046/j.1365-8711.1998.01904.x. arXiv: astro-ph/9802269 [astro-ph].
- Mandal, S. et al. (2020). “Extremely deep 150 MHz source counts from the LoTSS Deep Fields”. In: *arXiv e-prints*, arXiv:2011.08829, arXiv:2011.08829. arXiv: 2011.08829 [astro-ph.GA].
- Mauch, T. et al. (2003). “SUMSS: a wide-field radio imaging survey of the southern sky - II. The source catalogue”. In: *Mon. Not. R. Astron. Soc.* 342.4, pp. 1117–1130. DOI: 10.1046/j.1365-8711.2003.06605.x. arXiv: astro-ph/0303188 [astro-ph].
- Mead, A. J. et al. (2016). “Accurate halo-model matter power spectra with dark energy, massive neutrinos and modified gravitational forces”. In: *Mon. Not. R. Astron. Soc.* 459.2, pp. 1468–1488. DOI: 10.1093/mnras/stw681. arXiv: 1602.02154 [astro-ph.CO].
- Mohan, Niruj and David Rafferty (2015). *PyBDSF: Python Blob Detection and Source Finder*. ascl: 1502.007.
- Murphy, T. et al. (2007). “The second epoch Molonglo Galactic Plane Survey: compact source catalogue”. In: *Mon. Not. R. Astron. Soc.* 382.1, pp. 382–392. DOI: 10.1111/j.1365-2966.2007.12379.x. arXiv: 0708.3092 [astro-ph].
- Newville, M. et al. (2016). “Lmfit: Non-Linear Least-Square Minimization and Curve-Fitting for Python”. In: ascl: 1606.014.
- Nusser, Adi and Prabhakar Tiwari (2015). “The Clustering of Radio Galaxies: Biasing and Evolution versus Stellar Mass”. In: *Astrophys. J.* 812.1, 85, p. 85. DOI: 10.1088/0004-637X/812/1/85. arXiv: 1505.06817 [astro-ph.CO].
- Overzier, R. A. et al. (2003). “The spatial clustering of radio sources in NVSS and FIRST; implications for galaxy clustering evolution”. In: *Astron. Astrophys.* 405, pp. 53–72. DOI: 10.1051/0004-6361:20030527. arXiv: astro-ph/0304160 [astro-ph].
- Partridge, R. B. and David T. Wilkinson (1967). “Isotropy and Homogeneity of the Universe from Measurements of the Cosmic Microwave Background”. In: *Phys. Rev. Lett.* 18 (14), pp. 557–559. DOI: 10.1103/PhysRevLett.18.557. URL: <https://link.aps.org/doi/10.1103/PhysRevLett.18.557>.

- Peebles, P. J. E. (1980). *The large-scale structure of the universe*. Princeton University Press.
- Peebles, P. J. E. and David T. Wilkinson (1968). “Comment on the Anisotropy of the Primeval Fireball”. In: *Phys. Rev.* 174 (5), pp. 2168–2168. DOI: 10.1103/PhysRev.174.2168. URL: <https://link.aps.org/doi/10.1103/PhysRev.174.2168>.
- Penzias, A. A. and R. W. Wilson (1965). “A Measurement of Excess Antenna Temperature at 4080 Mc/s.” In: *Astrophys. J.* 142, pp. 419–421. DOI: 10.1086/148307.
- Peper, Marius (2017). “Forecasting the Cosmic Radio Dipole”. MA thesis. Bielefeld, Germany: Bielefeld University.
- Planck Collaboration et al. (2016). “Planck 2015 results. XIII. Cosmological parameters”. In: *Astron. Astrophys.* 594, A13, A13. DOI: 10.1051/0004-6361/201525830. arXiv: 1502.01589 [astro-ph.CO].
- Planck Collaboration et al. (2018a). “Planck 2018 results. I. Overview and the cosmological legacy of Planck”. In: *arXiv e-prints*. arXiv: 1807.06205.
- Planck Collaboration et al. (2018b). “Planck 2018 results. VI. Cosmological parameters”. In: *arXiv e-prints*. arXiv: 1807.06209 [astro-ph.CO].
- Rana, Sandeep and Jasjeet S. Bagla (2019). “Angular clustering of point sources at 150 MHz in the TGSS survey”. In: *Mon. Not. R. Astron. Soc.* 485, pp. 5891–5896. DOI: 10.1093/mnras/stz831. arXiv: 1802.05001 [astro-ph.GA].
- Rayleigh, Lord F.R.S. (1879). “XXXI. Investigations in optics, with special reference to the spectroscope”. In: *The London, Edinburgh, and Dublin Philosophical Magazine and Journal of Science* 8.49, pp. 261–274. DOI: 10.1080/14786447908639684. eprint: <https://doi.org/10.1080/14786447908639684>. URL: <https://doi.org/10.1080/14786447908639684>.
- Rengelink, R. B. et al. (1997). “The Westerbork Northern Sky Survey (WENSS), I. A 570 square degree Mini-Survey around the North Ecliptic Pole”. In: *Astron. Astrophys., Sup.* 124, pp. 259–280. DOI: 10.1051/aas:1997358.
- Rengelink, Roeland (1999). “Clustering evolution in the radio surveys WENSS and GB6”. In: *The Most Distant Radio Galaxies*. Ed. by H. J. A. Röttgering, P. N. Best, and M. D. Lehnert, p. 399.
- Roche, Nathan D. et al. (2002). “The clustering, number counts and morphology of extremely red ($R-K > 5$) galaxies to $K \leq 21$ ”. In: *Mon. Not. R. Astron. Soc.* 337.4, pp. 1282–1298. DOI: 10.1046/j.1365-8711.2002.05975.x. arXiv: astro-ph/0205259 [astro-ph].
- Rodríguez-Espinoza, J. M. and P. Alvarez Martin (1997). “Gran Telescopio Canarias: a 10 m telescope for the ORM.” In: *Optical Telescopes of Today and Tomorrow*. Ed. by Arne L. Ardeberg. Vol. 2871. Society of Photo-Optical Instrumentation Engineers (SPIE) Conference Series, pp. 69–73. DOI: 10.1117/12.269113.
- Rubart, M. and D. J. Schwarz (2013). “Cosmic radio dipole from NVSS and WENSS”. In: *Astron. Astrophys.* 555, A117, A117. DOI: 10.1051/0004-6361/201321215. arXiv: 1301.5559 [astro-ph.CO].

- Rubart, Matthias, David Bacon, and Dominik J. Schwarz (2014). “Impact of local structure on the cosmic radio dipole”. In: *Astron. Astrophys.* 565, A111, A111. DOI: 10.1051/0004-6361/201423583. arXiv: 1402.0376 [astro-ph.CO].
- Ryle, M., F. G. Smith, and B. Elsmore (1950). “A preliminary survey of the radio stars in the Northern Hemisphere”. In: *Mon. Not. R. Astron. Soc.* 110, p. 508. DOI: 10.1093/mnras/110.6.508.
- Sargent, M. T. et al. (2010). “The VLA-COSMOS Perspective on the Infrared-Radio Relation. I. New Constraints on Selection Biases and the Non-Evolution of the Infrared/Radio Properties of Star-Forming and Active Galactic Nucleus Galaxies at Intermediate and High Redshift”. In: *ApJS* 186.2, pp. 341–377. DOI: 10.1088/0067-0049/186/2/341. arXiv: 1001.1354 [astro-ph.CO].
- Schechter, P. (1976). “An analytic expression for the luminosity function for galaxies.” In: *Astrophys. J.* 203, pp. 297–306. DOI: 10.1086/154079.
- Schwarz, Dominik J. et al. (2018). “SKA and the Cosmic Radio Dipole”. In: *arXiv e-prints*. arXiv: 1810.06373 [astro-ph.CO].
- Seyfert, Carl K. (1943). “Nuclear Emission in Spiral Nebulae.” In: *Astrophys. J.* 97, p. 28. DOI: 10.1086/144488.
- Shimwell, T. W. et al. (2017). “The LOFAR Two-metre Sky Survey. I. Survey description and preliminary data release”. In: *Astron. Astrophys.* 598, A104, A104. DOI: 10.1051/0004-6361/201629313. arXiv: 1611.02700 [astro-ph.IM].
- Shimwell, T. W. et al. (2019). “The LOFAR Two-metre Sky Survey. II. First data release”. In: *Astron. Astrophys.* 622, A1, A1. DOI: 10.1051/0004-6361/201833559. arXiv: 1811.07926 [astro-ph.GA].
- Siewert, Thilo M. et al. (2020a). “One- and Two-point Source Statistics from the LOFAR Two-metre Sky Survey First Data Release”. In: *Astron. Astrophys.* 643, A100. DOI: 10.1051/0004-6361/201936592. arXiv: 1908.10309 [astro-ph.CO].
- Siewert, Thilo M., Matthias Schmidt-Rubart, and Dominik J. Schwarz (2020b). “The Cosmic Radio Dipole: Estimators and Frequency Dependence”. In: *arXiv e-prints*. arXiv: 2010.08366 [astro-ph.CO].
- Simon, P. (2007). “How accurate is Limber’s equation?” In: *Astron. Astrophys.* 473.3, pp. 711–714. DOI: 10.1051/0004-6361:20066352. arXiv: astro-ph/0609165 [astro-ph].
- Singal, Ashok K. (2011). “Large Peculiar Motion of the Solar System from the Dipole Anisotropy in Sky Brightness due to Distant Radio Sources”. In: *Astrophys. J. Let.* 742.2, L23, p. L23. DOI: 10.1088/2041-8205/742/2/L23. arXiv: 1110.6260 [astro-ph.CO].
- (2019). “Large disparity in cosmic reference frames determined from the sky distributions of radio sources and the microwave background radiation”. In: *Phys. Rev. D* 100.6, 063501, p. 063501. DOI: 10.1103/PhysRevD.100.063501. arXiv: 1904.11362 [physics.gen-ph].
- Smith, R. E. et al. (2003). “Stable clustering, the halo model and non-linear cosmological power spectra”. In: *Mon. Not. R. Astron. Soc.* 341.4, pp. 1311–1332. DOI: 10.1046/j.1365-8711.2003.06503.x. arXiv: astro-ph/0207664 [astro-ph].

- Smolčić, V. et al. (2008). “A New Method to Separate Star-forming from AGN Galaxies at Intermediate Redshift: The Submillijansky Radio Population in the VLA-COSMOS Survey”. In: *ApJS* 177.1, pp. 14–38. DOI: 10.1086/588028. arXiv: 0803.0997 [astro-ph].
- Square Kilometre Array Cosmology Science Working Group et al. (2020). “Cosmology with Phase 1 of the Square Kilometre Array Red Book 2018: Technical specifications and performance forecasts”. In: *Publ. Astron. Soc. Australia* 37, e007, e007. DOI: 10.1017/pasa.2019.51. arXiv: 1811.02743 [astro-ph.CO].
- Swarup, Govind (1991). “Giant metrewave radio telescope (GMRT)”. In: *IAU Colloq. 131: Radio Interferometry. Theory, Techniques, and Applications*. Ed. by T. J. Cornwell and R. A. Perley. Vol. 19. Astronomical Society of the Pacific Conference Series, pp. 376–380.
- Takahashi, Ryuichi et al. (2012). “Revising the Halofit Model for the Nonlinear Matter Power Spectrum”. In: *Astrophys. J.* 761.2, 152, p. 152. DOI: 10.1088/0004-637X/761/2/152. arXiv: 1208.2701 [astro-ph.CO].
- Tasker, Niven J. et al. (1994). “The Parkes-MIT-NRAO Surveys. V. Maps for the Tropical Survey Covering -29 degrees < delta < -9 degrees”. In: *Astron. J.* 107, p. 2115. DOI: 10.1086/117022.
- Tauber, J. A. et al. (2010). “Planck pre-launch status: The Planck mission”. In: *Astron. Astrophys.* 520, A1, A1. DOI: 10.1051/0004-6361/200912983.
- Taylor, M. B. (2005). “TOPCAT & STIL: Starlink Table/VOTable Processing Software”. In: *Astronomical Data Analysis Software and Systems XIV*. Ed. by P. Shopbell, M. Britton, and R. Ebert. Vol. 347. Astronomical Society of the Pacific Conference Series, p. 29.
- Tingay, S. J. et al. (2013). “The Murchison Widefield Array: The Square Kilometre Array Precursor at Low Radio Frequencies”. In: *Publ. Astron. Soc. Australia* 30, e007, e007. DOI: 10.1017/pasa.2012.007. arXiv: 1206.6945 [astro-ph.IM].
- Tiwari, Prabhakar (2016). “Radio spectral index from NVSS and TGSS”. In: *arXiv e-prints*, arXiv:1609.01308, arXiv:1609.01308. arXiv: 1609.01308 [astro-ph.GA].
- Tiwari, Prabhakar and Adi Nusser (2016). “Revisiting the NVSS number count dipole”. In: *J. Cosmol. Astropart. Phys.* 2016.3, 062, p. 062. DOI: 10.1088/1475-7516/2016/03/062. arXiv: 1509.02532 [astro-ph.CO].
- Tiwari, Prabhakar, Shamik Ghosh, and Pankaj Jain (2019). “The Galaxy Power Spectrum from TGSS ADR1 and the Effect of Flux Calibration Systematics”. In: *Astrophys. J.* 887.2, 175, p. 175. DOI: 10.3847/1538-4357/ab54c8. arXiv: 1907.10305 [astro-ph.CO].
- Totsuji, H. and T. Kihara (1969). “The Correlation Function for the Distribution of Galaxies”. In: *Publ. Astron. Soc. Japan* 21, p. 221.
- Turner, Michael S. (1991). “Tilted Universe and other remnants of the preinflationary Universe”. In: *Phys. Rev. D* 44.12, pp. 3737–3748. DOI: 10.1103/PhysRevD.44.3737.
- van Haarlem, M. P. et al. (2013). “LOFAR: The LOw-Frequency ARray”. In: *Astron. Astrophys.* 556, A2, A2. DOI: 10.1051/0004-6361/201220873. arXiv: 1305.3550 [astro-ph.IM].

- Virtanen, Pauli et al. (2020). “SciPy 1.0: Fundamental Algorithms for Scientific Computing in Python”. In: *Nature Methods* 17, pp. 261–272. DOI: <https://doi.org/10.1038/s41592-019-0686-2>.
- Walt, StÅlfan van der, S. Chris Colbert, and GaÅñl Varoquaux (2011). “The NumPy Array: A Structure for Efficient Numerical Computation”. In: *Computing in Science & Engineering* 13.2, pp. 22–30. DOI: 10.1109/MCSE.2011.37. eprint: <https://aip.scitation.org/doi/pdf/10.1109/MCSE.2011.37>. URL: <https://aip.scitation.org/doi/abs/10.1109/MCSE.2011.37>.
- Weinberg, Steven (1972). *Gravitation and Cosmology: Principles and Applications of the General Theory of Relativity*.
- White, Richard L. et al. (1997). “A Catalog of 1.4 GHz Radio Sources from the FIRST Survey”. In: *Astrophys. J.* 475.2, pp. 479–493. DOI: 10.1086/303564.
- Williams, W. L. et al. (2016). “LOFAR 150-MHz observations of the Boötes field: catalogue and source counts”. In: *Mon. Not. R. Astron. Soc.* 460, pp. 2385–2412. DOI: 10.1093/mnras/stw1056. arXiv: 1605.01531.
- Williams, W. L. et al. (2019). “The LOFAR Two-metre Sky Survey. III. First data release: Optical/infrared identifications and value-added catalogue”. In: *Astron. Astrophys.* 622, A2, A2. DOI: 10.1051/0004-6361/201833564. arXiv: 1811.07927 [astro-ph.GA].
- Wilman, R. J. et al. (2003). “The clustering of sub-mJy radio sources in the Bootes Deep Field”. In: *Mon. Not. R. Astron. Soc.* 339.3, pp. 695–700. DOI: 10.1046/j.1365-8711.2003.06215.x. arXiv: astro-ph/0210679 [astro-ph].
- Wilman, R. J. et al. (2008). “A semi-empirical simulation of the extragalactic radio continuum sky for next generation radio telescopes”. In: *Mon. Not. R. Astron. Soc.* 388.3, pp. 1335–1348. DOI: 10.1111/j.1365-2966.2008.13486.x. arXiv: 0805.3413 [astro-ph].
- Wilson, A. S. and E. J. M. Colbert (1995). “The Difference between Radio-loud and Radio-quiet Active Galaxies”. In: *Astrophys. J.* 438, p. 62. DOI: 10.1086/175054. arXiv: astro-ph/9408005 [astro-ph].
- Wilson, Thomas L., Kristen Rohlfs, and Susanne HÅijttmeister (2013). *Tools of radio astronomy*. eng. 6. ed. Astronomy and astrophysics library. Berlin [u.a.]: Springer, XV, 609 S. ISBN: 978-3-642-39949-7, 3-642-39949-5. URL: http://deposit.d-nb.de/cgi-bin/dokserv?id=4390559&prov=M&dok_var=1&dok_ext=htm.
- Wright, Alan E. et al. (1994). “The Parkes-MIT-NRAO (PMN) Surveys. II. Source Catalog for the Southern Survey (-87 degrees δ; -37 degrees)”. In: *ApJS* 91, p. 111. DOI: 10.1086/191939.
- Wright, Alan E. et al. (1996). “The Parkes-MIT-NRAO (PMN) Surveys. VIII. Source Catalog for the Zenith Survey (-37.0 degrees δ; -29.0 degrees)”. In: *ApJS* 103, p. 145. DOI: 10.1086/192272.
- Wright, Edward L. et al. (2010). “The Wide-field Infrared Survey Explorer (WISE): Mission Description and Initial On-orbit Performance”. In: *Astron. J.* 140.6, pp. 1868–1881. DOI: 10.1088/0004-6256/140/6/1868. arXiv: 1008.0031 [astro-ph.IM].

- Xavier, Henrique S., Filipe B. Abdalla, and Benjamin Joachimi (2016). “Improving log-normal models for cosmological fields”. In: *Mon. Not. R. Astron. Soc.* 459.4, pp. 3693–3710. DOI: 10.1093/mnras/stw874. arXiv: 1602.08503 [astro-ph.CO].
- Yun, Min S., Naveen A. Reddy, and J. J. Condon (2001). “Radio Properties of Infrared-selected Galaxies in the IRAS 2 Jy Sample”. In: *Astrophys. J.* 554.2, pp. 803–822. DOI: 10.1086/323145. arXiv: astro-ph/0102154 [astro-ph].
- Zhang, X. et al. (1993). “The Miyun 232 MHz survey. I. Fields centred at RA:00h41m, Dec:41deg12’ and RA:07h00m, Dec:35deg00’”. In: *Astron. Astrophys., Sup.* 99, pp. 545–575.
- Zhang, X. et al. (1997). “The Miyun 232 MHz survey.” In: *Astron. Astrophys., Sup.* 121, pp. 59–63. DOI: 10.1051/aas:1997314.
- Zonca, Andrea et al. (2019). “healpy: equal area pixelization and spherical harmonics transforms for data on the sphere in Python”. In: *Journal of Open Source Software* 4.35, p. 1298. DOI: 10.21105/joss.01298. URL: <https://doi.org/10.21105/joss.01298>.

Ehrenwörtliche Erklärung

Hiermit versichere ich, dass ich die vorliegende Dissertation ohne Hilfe Dritter und ohne Zuhilfenahme anderer als der angegebenen Quellen und Hilfsmittel angefertigt habe. Die den benutzten Quellen wörtlich oder inhaltlich entnommenen Stellen sind als solche kenntlich gemacht. Diese Arbeit hat in gleicher oder ähnlicher Form noch keinem Prüfungsamt vorgelegen.